Voltage Programmable Liquid Optical Devices

Gary George Wells

A thesis submitted in partial fulfillment of the
requirements of Nottingham Trent University
for the degree of Doctor of Philosophy

October 2009

Acknowledgements

Abstract

In this study I have looked at two types of voltage programmable liquid optical device. The first is a rotatable liquid crystal waveplate and the second is an amplitude programmable liquid phase grating. The rotatable waveplate was created by confining a droplet of E7 nematic liquid crystal between two glass substrates in a photolithographically produced square well of $60{\times}60{\times}15\mu$m dimensions. The droplet forms a circular disc shape with two nematic defects at opposite edges of the disc. The optical texture has been examined and the most likely n-director orientation is shown to be Bipolar. Electrodes etched into the sandwiching substrate allow an in-plane electric field to be applied and because of the E7's positive dielectric anisotropy the n-director of the droplet aligns itself with the field. The speed at which this rotation occurs is shown to follow the relationship $\theta = 0.0472\tau V^2$ and rotation speeds of 450°/s have been achieved. The droplet is multistable and can be rotated to any arbitrary angle. The temperature of the droplet affects its switching ability by changing the shape and size of the droplet within the well. The switching time with voltage at different temperatures has been investigated and shows that at higher temperatures switching is faster. Rounded square droplets have also been seen which exhibit six stable states which can be switched from one state to another by applying various electric fields. The switching speed of these states has been investigated for several different switching regimes.

A voltage programmable phase grating has also been demonstrated by inducing an undulation in the surface of a thin film of either hexadecane or 1-decanol oil. The thin film of oil is the result of a dielectrophoretic force created by a non-uniform electric field above a set of interdigitated electrodes. The thickness of the film is almost independent of the applied voltage. At higher voltages, an undulation in the oil air interface occurs which is static and stable with the same period as the electrode pitch. Measurements of hexadecane and 1-decanol oil for a variety of layer thickness on several different electrode pitches show that the amplitude of the undulation is proportional to the voltage squared. This scaling relationship and the exponential dependence on the ratio of oil thickness and the electrode pitch can be explained in terms of the balance between the dielectrophoretic forces created by the non-uniform electric field and the increase in surface energy associated with the surface deformation. For a thin layer of oil with low dielectric constant the higher order spatial harmonics in the electric field cause the undulation to become non-sinusoidal. The extent to which these harmonics shape the surface of the oil is explored and their relationship to oil thickness is shown. The relative contributions of these higher order harmonics are also shown to be independent from the applied voltage. As an example of the devices applications it has been shown to operate as an amplitude programmable phase grating and diffracts the energy of an incoming 543nm laser from the zero straight through order into the higher orders. The diffraction efficiency of 32.8% is very close to that predicted by theory. The device is polarization insensitive and switching times in excess of 40μs have been achieved in switching the first diffraction order from its minimum intensity to its maximum.

Contents

I

Contents

Contents

List of Figures

Chapter 1

Introduction

1.1 Aims and Rationale

Recently there has been much interest in photonic devices based on microfluidics. These include displays [3, 4], refractive tunable micro-lenses and optical beamsteerers [5–7]. Many of the current devices use electrowetting to manipulate the interface between two immiscible liquids to create the desired optical effects. Diffractive optical elements used in telecommunications are dominated by either acousto-optic or electro-optic devices [8], however such devices are inherently polarization sensitive due the the nature of the physical effects used in their operation. The aim of this project is to use the dielectrophoretic force, experienced by a polarizable liquid in the presence of a non uniform electric field, to alter the interface between between a thin layer of liquid and its interface with the surrounding air. By creating periodic variations in the thickness of the layer, it should be possible to use the device as a polarisation insensitive diffractive optical element which is able to divert the path of an incoming beam of light.

Liquid crystal devices are also of great interest for use in optical telecommunications and display technology. Bistability and multistability is an interesting characteristic of liquid crystals which can be exploited to create low energy displays and photonic switching devices for optical telecommunications. The aim of

this work was to create a device in which multiple stable states of the optical axis occur, at arbitrary in-plane rotation angles, in a small disc shape droplets of E7 liquid crystal. Such a device could be used to alter the polarisation state of light at polarization sensitive optical interconnections, such as those previously mentioned. As a continuously rotatable wave plate it could be used to compensate for mechanical stress induced polarization changes in optical fibres.

1.2 Liquid Crystals

Liquid crystal devices are now a ubiquitous technology in flat panel and portable displays including twisted and super-twisted nematic displays [9, 10] high efficiency displays [11]as well as dye displays [12]. Because they show a massive electro-optic response [13] they are also the subject of intense interest for applications in optical telecommunications [8, 14–16]. Such advances include holographic optical switching incorporating ferroelectric liquid crystals [17] and computer generated holography [18], as well as optical switches, attenuators and gain equalizers [19, 20]. Also, if polarization control is required, at temporary interconnections between polarization sensitive components [21] and they have also found uses in biomedical imaging [22].

Of particular interest in this study are the director orientations in small spherical or cylindrical cavities and these director orientations have been the subject of many studies. The planer polar alignment, discussed in chapter 3, has been seen in cylindrical cavities in optical fibers [23, 24] and in anopore and nucleopore membranes [25]. The bipolar alignment has been seen in polymer dispersed liquid crystal (PDLC) films [26, 27] the thermal and tranmissive properties of which have also been studied [28–30].

1.2.1 Liquid Crystal Theory

Liquid crystals are a phase of matter in between liquids and solids (Figure 1.1). They consist of long rod or disc like molecules and it is the order of these molecules which impart the interesting characteristics of a liquid crystal .
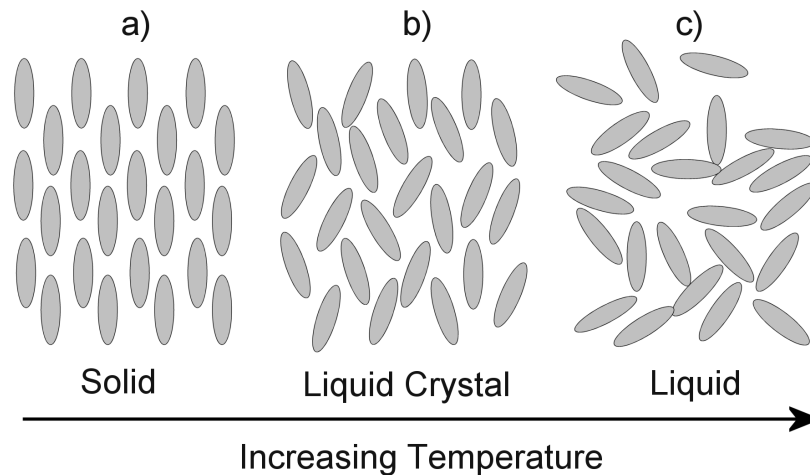
Figure 1.1: Schematic illustration of solid, liquid crystal and liquid phases with increasing temperature across the bottom

In a solid (Figure 1.1a) the molecules have both positional and orientational order, that is to say they are fixed in space and all point in the same direction. In a liquid (Figure 1.1 c) the molecules do not have any positional or any directional order and the molecules are free to move within the liquid and to orient themselves in any direction. In between these two phases of matter lies the liquid crystal (Figure 1.1 b) in which the positional order of the molecules is lost but there still remains some orientational order.

The direction in which the molecules point, in a liquid crystal, is represented by the *director* and is the average direction in which the *long axis* of say a thousand molecules in the liquid crystal points. In figure 1.2 the director is shown as the vector **n**. It should be noted that the n-Director is pointing upwards. This is a purely arbitrary choice and the director could easily be chosen to be pointing downwards. There is complete equivalence between the up and down direction of the director. This becomes important when looking at the optical texture of a

3

liquid crystal (section 1.2.8).
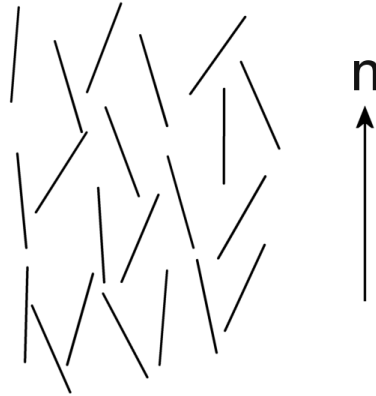
Figure 1.2: Schematic showing the arrangement of the molecules in a nematic liquid crystal

1.2.2 The Order Parameter

In liquid crystal the molecules are free to diffuse about the bulk much like that of a liquid. Nevertheless, as they do so they also maintain a certain amount of orientational order. The order parameter S of a liquid crystal defines how well the molecules in the liquid crystal align with the director. This order parameter is defined by the equation:

$$S = \frac{< 3\cos^2\theta - 1 >}{2} \tag{1.1}$$

Where θ is the angle between the molecules and the n-director [31]

It can be seen from equation 1.1 that if all the molecules in a liquid crystal formed an angle of 0 ° with the director (i.e. they are perfectly ordered) then the order parameter would be 1. For a highly disordered liquid crystal the order parameter is independent of Theta. The order parameter of a liquid crystal is also dependent on the temperature with the liquid crystal becoming increasingly disordered with increasing temperature. The order parameter usually has a value between 0.8 and 0.3 [32](Figure 1.3) until, at some point, all order within

the liquid crystal is lost and the liquid crystal becomes an isotropic fluid. The temperature at which the liquid crystal becomes isotropic is called the nematic isotropic transition temperature.
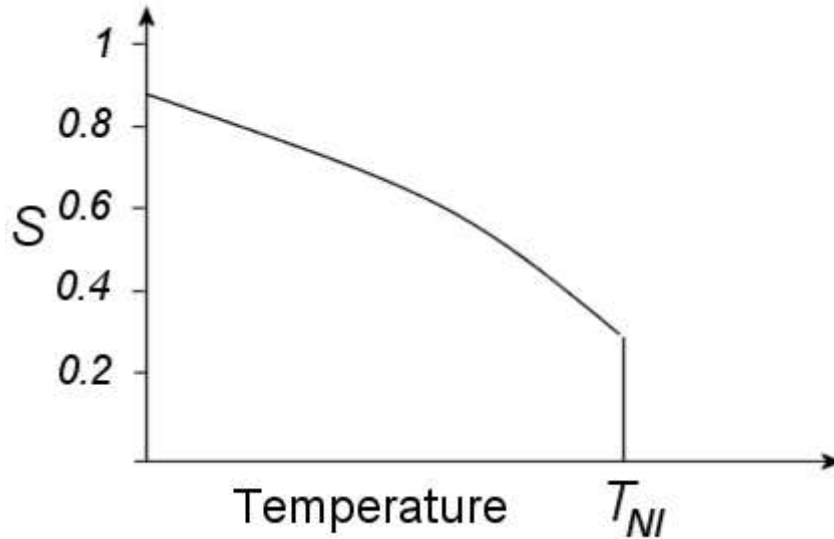
Figure 1.3: The variation of the order parameter in a liquid crystal with increasing temperature.

1.2.3 Nematic Liquid Crystals

There are several properties of a liquid crystal which determine it to be nematic [13]. These main features are summarized below:

1. The centers of gravity of the individual molecules have no long range order.

2. There is some order in the overall direction of the molecules and they tend to be parallel about some common axis. This common axis or average direction of the molecular axis is known as the **n** director (figure 1.2).

3. The direction of the director is arbitrary in space; in practice the director can be controlled with several techniques which will be discussed later.

4. There is complete equivalence between the **n** direction and the -**n** direction.

5. The nematic phase will only occur in materials in which there is no distinction between right and left handed molecules.

1.2.4   Boundary Effects and Surface Anchoring

The interface of a liquid crystal with another medium affects the liquid crystal such that it imparts a particular direction for the n-director at the boundary. This preferred direction for the director is dependent on type and characteristics of a particular boundary [13].

The three main types of anchoring at a surface are shown in figure 1.4. Figure 1.4a) shows a situation in which the alignment of the liquid crystal at the surface is planer. This kind of planer alignment can be achieved at the surface of a crystal[13] where the easy direction for the director is along a some simple crystallographic axes. This type of alignment can also be achieved by coating a surface with a polymer or surface coupling agent, with the molecules being absorbed parallel to the surface [33]. However, the parallel alignment introduced by the addition of a polymer or bonding agent is a random planer alignment, in that although the long axis of the molecules are in the plane of the surface, the direction of the long axis is purely random which results in a schlieren texture when viewed through crossed polarisers(section 1.2.9). The direction of the long axis can be made to point in the same direction by unidirectional rubbing causing the alignment to become homogeneous. A homeotropic alignment (Figure 1.4b) at the surface in which the liquid crystal molecules align perpendicular to the surface can be achieved on surfaces by binding amphiphilic molecules to the surface which attach their polar head to the surface, and leave the tail perpendicular to the surface[13, 33]. It can also be achieved with coupling agents such as silanes with long alkyl chains[34].

A particular interest in liquid crystal studies are mechanically bistable devices. A mechanically bistable device is one in which the director orientation
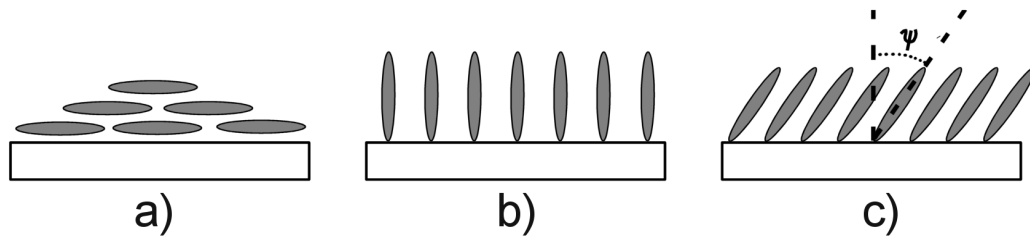
Figure 1.4: Three types of anchoring at a surface. a) Homo tropic b) homogeneous c)LC forms angle ψ at the surface

of the liquid crystal can assume either of two different and equal low energy states [35]. Devices incorperating this affect have the advantage of low power consumption because the optical properties of the device can be changed with the application of a voltage and the device keeps these properties even if the voltage is removed. Bistability has been achieved with various methods including arrays of microscopic posts [35–37] and various types of surface grating structures [35, 36, 38]. Particular alignments can occur if liquid crystals are confined in small cavities [39, 40] and easy alignment directions can be produced with specific surface treatments such as nano rubbing [41] and silicon di-oxide films irradiated with low energy ion beams [42].

1.2.5   Anisotropy and Birefringence

For an electric dipole consisting of two equal and oppositely charged particles Q_1 and Q_2 separated by a distance l the dipole moment $\mathbf{p}$ is defined as [43]

$$\mathbf{p} = Q\mathbf{l} \tag{1.2}$$

If a linear and isotropic medium contains N molecules per unit volume then the dipole moment per unit volume $\mathbf{P}$ is given by

$$\mathbf{P} = N\mathbf{p} \tag{1.3}$$

If an electric field $\mathbf{E}$ is applied to a linear isotropic and homogeneous material

the dipole moment induced in each molecule leads to a net dipole moment for a unit volume called the polarization **P**. For small electric fields **P** is proportional to **E** and the constant of proportionality is the electric susceptibility χ_e. The polarization is given by the equation

$$\mathbf{P} = \epsilon_0 \chi_e \mathbf{E} \tag{1.4}$$

Where ϵ_0 is the permittivity of free space $8.85 \times 10^{-12}\ C^2/Nm^2$

The induced polarization of the material arises via three basic polarization processes [44]

1. *Electronic Polarization* occurs when, in an electric field, the centre of charge of the electron cloud in a molecule moves slightly with respect to the centre of charge of the nuclei.

2. *Orientational polarization* occurs when polar molecules tend to align in an applied field.

3. *Atomic polarization* occurs when *ions* of different sign in solids such as crystals move in different directions in an electric field.

In E7 liquid crystal there are no contributions to the polarization through atomic polarization and the polarization of the liquid crystal arises from electronic and orientation polarization.

Anisotropic Electronic Polarization

We can visualize anisotropic electronic polarization with a simple model of an atomic nucleus bound to the electron shell by springs [45] (Figure 1.5), where the spring constants in the x and y directions have different values μ_1 and μ_2 respectively.

In the presence of an electric field the force on the nucleus and the electron cloud causes them to be displaced. The displacement of a spring for a given force

8
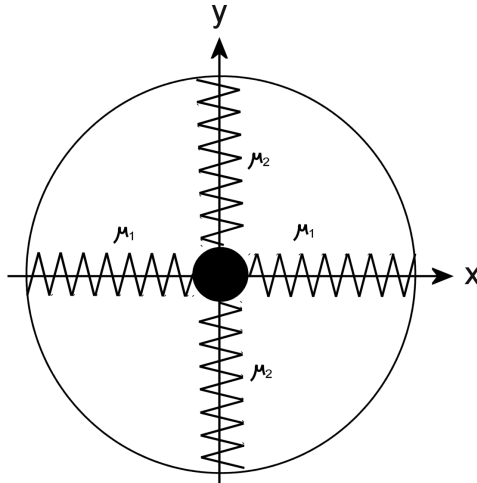
Figure 1.5: model of a nucleus bound to the electron shell by springs

is governed by Hooke's law $F = \mu\Delta x$. Where F is the force, μ is the spring constant and Δx is the displacement. The force exerted on the electron cloud and the nucleus by the electric field is governed by the equation $F = qE$, where q is the charge and E is the electric field component in the given direction. From these two equations we can see that $qE \sim \mu\Delta x$ and thus the force in the x and y direction is given by

$$qE_x \sim \mu_1\Delta x \Rightarrow \frac{qE_x}{\mu_1} \sim \Delta x$$

$$qE_y \sim \mu_2\Delta x \Rightarrow \frac{qE_y}{\mu_2} \sim \Delta x$$

Thus a smaller spring constant would result in a greater displacement Δx and a greater dipole moment. Since a smaller spring constant μ is analogous to a larger electric susceptibility χ then a larger dipole moment would be created in the direction with a lowest value of μ

Anisotropic Molecular Polarization

The polarization of the molecule arises due to contributions from the atomic polarization of the atoms in the molecule and the polarization of any de-localized

electrons in the molecule.

As an example figure 1.6 shows the chemical formula for 5CB. The benzene rings in the molecular structure give rise to a delocalized cloud of electrons. In the presence of an electric field this cloud is displaced relative to the atomic nuclei in the molecule. The amount of displacement along the long axis of the molecule is greater than the displacement perpendicular to the long axis. This leads to a larger polarization along the long axis than that perpendicular to the long axis.
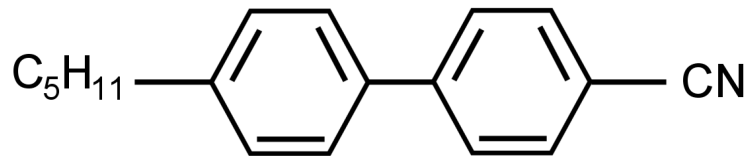
Figure 1.6: Chemical formula of 5CB

As stated in section 1.2.2 there is a tendency for the molecules in a liquid crystal to point in a preferred direction. It is the combined effect of the ordering of the liquid crystal molecules and the anisotropic nature of the molecules that the liquid crystal shows an anisotropic bulk polarization in relation to the n director.

Thermal Contributions

The alignment of dipoles is also frustrated by the thermal motion. The probability of a dipole, with dipole moment μ, pointing along a particular direction in an electric field in a linear isotropic medium is given by the *Langevin function* (Figure 1.7).

The Langevin function shows that the ordering of particles in an electric field increases with higher electric fields and with a larger dipole moment. It also shows that as temperature is increased the ordering of the dipoles decreases.
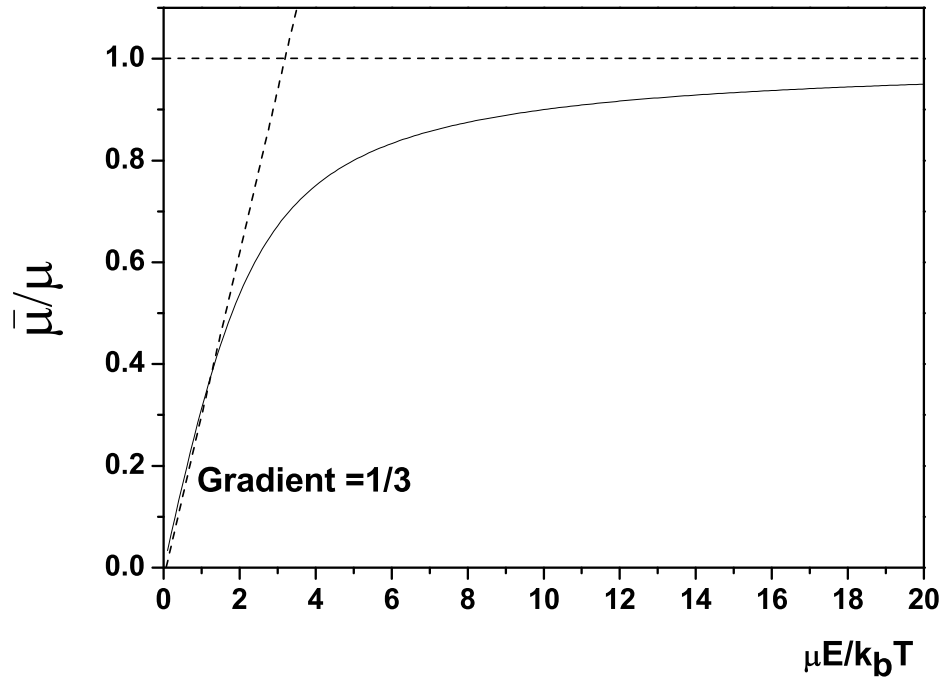
Figure 1.7: Langevin function

1.2.6 Anisotropy of Liquid Crystals

The electric susceptibility of a liquid crystal is a parameter which depends on the polarisability of the liquid crystal and is an example of an anisotropic property i.e it is dependent on the direction of the applied electric field. Since a liquid crystal is more polarisable in one direction than the other there are two values for the electric susceptibility $\chi_\parallel$ and $\chi_\perp$ for an electric field applied parallel and perpendicular to the director respectively. If the director lies in the z-direction then the total polarization of the liquid crystal for an electric field with components E_x, E_y and E_z is now given by the sum of all the contributing components of the polarization [32] i.e.

$$\mathbf{P}_x = \epsilon_0 \chi_\perp \mathbf{E}_x \qquad \mathbf{P}_y = \epsilon_0 \chi_\perp \mathbf{E}_y \qquad \mathbf{P}_z = \epsilon_0 \chi_\parallel \mathbf{E}_z$$

In the presence of an electric field the charged parts of a liquid crystal molecule,

11

i.e. the positive nucleus and the negative electrons of the molecules, experience opposite forces which lead to the formation of an *Induced electric dipole*. This induced electric dipole is dependent on the polarisability of the molecule in different directions. The difference between the polarisability in directions parallel and perpendicular to the optical axis is known the dielectric anisotropy and is governed by the equation

$$\Delta\epsilon = \epsilon_{\parallel} - \epsilon_{\perp} \qquad (1.5)$$

where $\epsilon_{\parallel}$ and $\epsilon_{\perp}$ are the dielectric constants parallel and perpendicular to the optical axis respectively. Since the dielectric constant ϵ of a material is given by the equation [46]

$$\epsilon = \epsilon_0(1 + \chi)$$

we can see that a higher electric susceptibility χ gives a higher dielectric constant ϵ. From equation 1.5 we can see that for a liquid crystal with a positive dielectric anisotropy, i.e. if $\Delta\epsilon > 0$, then the dielectric constant parallel to the optical axis $\epsilon_{\parallel}$ is greater than the dielectric constant perpendicular to the optical axis and the dipole moment of the molecule is larger in the direction along the optical axis. Conversly, if $\Delta\epsilon < 0$ then $\epsilon_{\perp}$ is greater than $\epsilon_{\parallel}$ and the larger dipole moment is in the direction perpendicular to the optical axis.

Figure 1.8 shows these two scenarios where a region of liquid crystal is under the influence of an external electric field. The average direction of molecular alignment for a large number of molecules or the n-director is marked and lies along the long axis of the region. In the figure 1.8a) the positive anisotropy of the liquid crystal gives a dipole moment along the optical axis of the Liquid Crystal. This in turn leads to forces generated in opposite directions at the tips of the region which aligns itself to the electric field. Figure 1.8b) shows a liquid crystal with a negative anisotropy and as such the rotational forces are generated at the
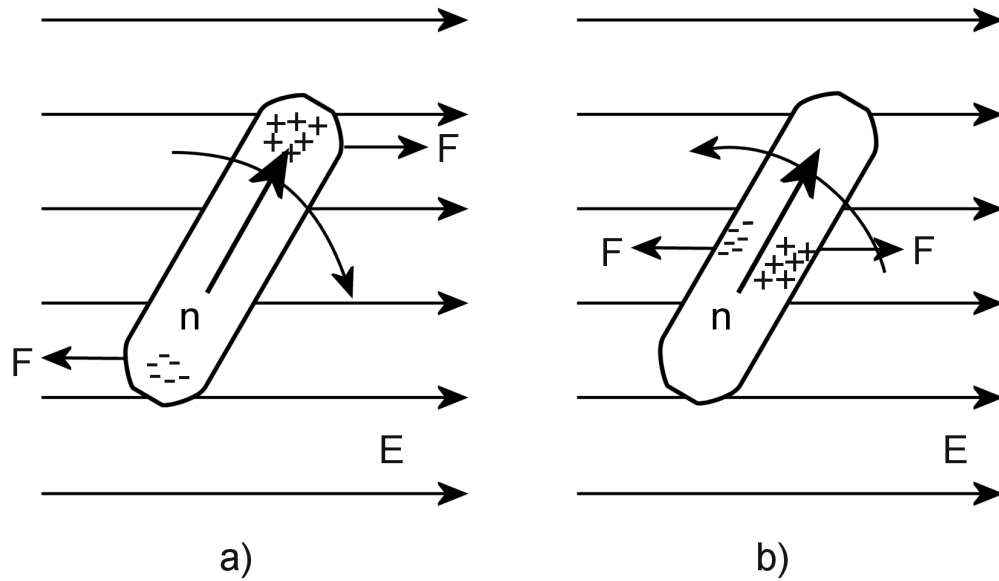
Figure 1.8: The action of an electric field on a region of liquid crystal a) shows the action if $\Delta\epsilon > 0$ and b)if $\Delta\epsilon < 0$

centre of the region and cause it to align perpendicular the electric field.

1.2.7   The Wave Plate

Polarisation controllers are generally required due to effects in long range optical telecommunications which alter the state of polarization of light such as external stresses on optical fibres changing the optical properties of the fibre [47] or where light needs to be directed into polarization sensitive components. Liquid crystal wave plates have been created with smectic and nematic liquid crystal in which a homeotropically aligned sandwich of liquid crystal is forced to re-align by the application of an in plane electric field [48–51]. With multiple electrode addressing of the liquid crystal it can be made to rotate endlessly and as such allow any polarization of light emerging from, or entering optical fibres to be controlled.

The dielectric anisotropy of a thin layer of liquid crystal allows it to be tailored via the thickness of the slab to act as a wave plate. This is a slab of material in which the two orthogonal components of the **E**-field of incoming light traverse the

thickness of the slab at different speeds. Light propagates through a transparent medium by exciting the atoms within the medium [52]. The electrons are driven by the **E**-field and the re radiated secondary wavelets recombine to from the resultant refracted wave. The speed of the refracted wave and thus the index of refraction is determined by the difference between the frequency of the **E**-field and the natural resonant frequency of the atoms. It was shown in section 1.2.6 that the electric susceptibility of a an anisotropic material is different in directions parallel and perpendicular to the optical axis. This difference leads to a difference in the resonant frequency of the atoms in these directions and thus the speed of the radiated wave is also different in these directions.

By considering linearly polarized light traversing an optically anisotropic material the incoming light can be represented as the vector sum of the components of the **E**-field parallel and perpendicular to the optical axis of the material.

$$\mathbf{E}_0 = \mathbf{E}_\parallel + \mathbf{E}_\perp \tag{1.6}$$

Where the individual components $\mathbf{E}_\parallel$ and $\mathbf{E}_\perp$ are given by

$$\mathbf{E}_\parallel = \mathbf{E}_{o\parallel} \cos(kz - \omega t) \tag{1.7}$$

$$\mathbf{E}_\perp = \mathbf{E}_{o\perp} \cos(kz - \omega t + \delta) \tag{1.8}$$

δ is now the phase difference introduced by the anisotropy of the liquid crystal as given by the equation:

$$\delta = \frac{2\pi}{\lambda}(n_\parallel - n_\perp)d \tag{1.9}$$

Where λ is the wavelength of the light, $n_\parallel$ and $n_\perp$ are the parallel and perpendicular refractive indices respectively and d is the thickness of the plate. The amount by which the phases of the components of the **E**-field differ leads to the emergent light being polarized into different configurations. Figure 1.9 shows that if the

phase difference $\delta = \pi$ then the light emerging from the wave plate is linearly polarized with its axis of polarization reversed and if the phase difference $\delta = \frac{\pi}{2}$ then the emergent light is circularly polarized. These two configurations of the wave plate with $\delta = \pi$ and $\delta = \frac{\pi}{2}$ are special cases of the plate and are known as half-wave and quarter-wave plates respectively.
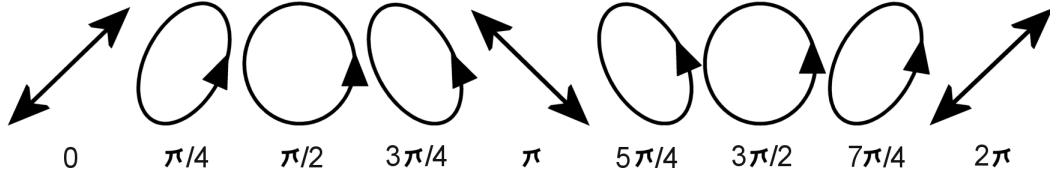
Figure 1.9: Polarization configurations for various values of the phase difference δ. it is assumed that $\mathbf{E}_{\parallel} = \mathbf{E}_{\perp}$

1.2.8 Optical Anisotropy (Birefringence)

The intensity of light passing through a birefringent slab between polarisers, crossed at an angle χ is given by the general equation[53].

$$I = E^2 \left[\cos^2 \chi - \sin 2\phi \sin 2(\phi - \chi) sin^2 \frac{\delta}{2} \right] \tag{1.10}$$

Where I is the intensity of the output light, E is the magnitude of the electric field component, χ is the angle between the polarisers, ϕ is the angle between the input polarizer and the optical axis of the slab and δ is the phase difference between the two orthogonal components on leaving the slab given by equation 1.9

If the input polarizer and the analyzer are aligned orthogonal i.e. $\chi = \frac{\pi}{2}$ this equation reduces to:

$$I_{\perp} = E^2 \sin^2 2\phi \sin^2 \frac{\delta}{2} \tag{1.11}$$

The term involving ϕ on the right hand side of equation 1.11 involves only the

optical axis of the slab and in the case of a liquid crystal this is the same as the **n**-director. Thus we can see that if the director is oriented such that it is parallel or perpendicular to the input polarizer then $\sin^2 \theta = 0$ for both cases of $\theta = 0$ and $\theta = \pi$ and any light passing through the system is completely extinguished.

The term involving δ on the right hand side of equation 1.11 is dependent on both the thickness of the slab and the wavelength of the incident light. Thus, for a slab with a particular value of $n_{\parallel} - n_{\perp}$ the light is completely extinguished if δ is an integer multiple of π.

The thickness term in equation 1.11 is also wavelength dependent, if the correct thickness of slab is chosen and the wave plate is illuminated with white light, a particular colour of emergent light can be chosen.

This method of crossed polarization microscopy is used to extrapolate possible director alignments in the liquid crystal droplets. Figure 1.10 shows a schematic drawing of this effect.
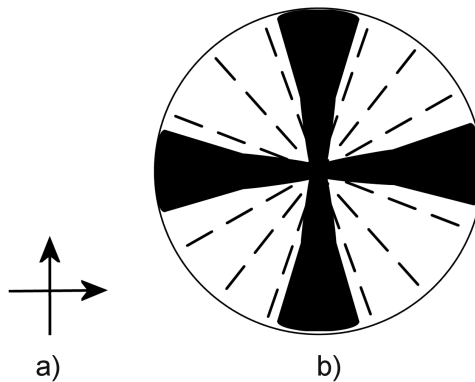
Figure 1.10: Schematic of a nematic droplet under crossed polarisers. The droplet has a radial alignment of the director shown as black bars and the brush texture under crossed polarizers is shown in black

The circular droplet in figure 1.10b) has a radial alignment i.e. the director is homeotropic at the edge of the droplet and radiates from the centre of the droplet. In this configuration the director is parallel to the crossed polarisers both horizontally across the centre of the droplet and vertically down the middle of the droplet which leads to black brushes in a cross shape. By rotating the crossed

polarisers, different regions where the director is parallel or perpendicular to the crossed polarisers allow the most likely director orientation to be extrapolated.

1.2.9 Nematic Defects

Although the molecules of a liquid crystal are ordered in the ways described in section 1.2 this order is a short range order. If a thin layer of liquid crystal is placed on a surface which imparts random planar alignment to the liquid crystal (Section 1.2.4) and viewed through crossed polarisers the texture of the liquid crystal shows small point like structures joined by black brushes (Figure 1.11). The point like structures are formed because as the director of the liquid crystal changes from one direction to another, this change is usually a gradual one. However, if the direction of the director changes abruptly at a point then the liquid crystal melts resulting in the formation of defect. The black brush structures show areas in the liquid crystal in which the director orientation is either parallel or perpendicular to one of the crossed polarisers (Section 1.2.8). Figure 1.11 shows a typical image of the texture of a thin layer of nematic liquid crystal viewed through crossed polarisers [54].
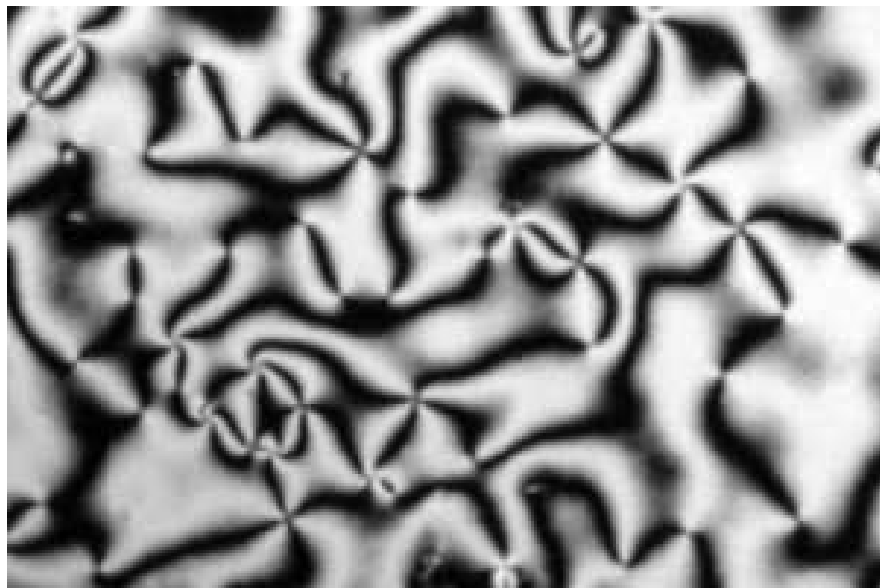
Figure 1.11: Schlieren Texture of a thin film of nematic liquid crystal viewed through crossed polarizers
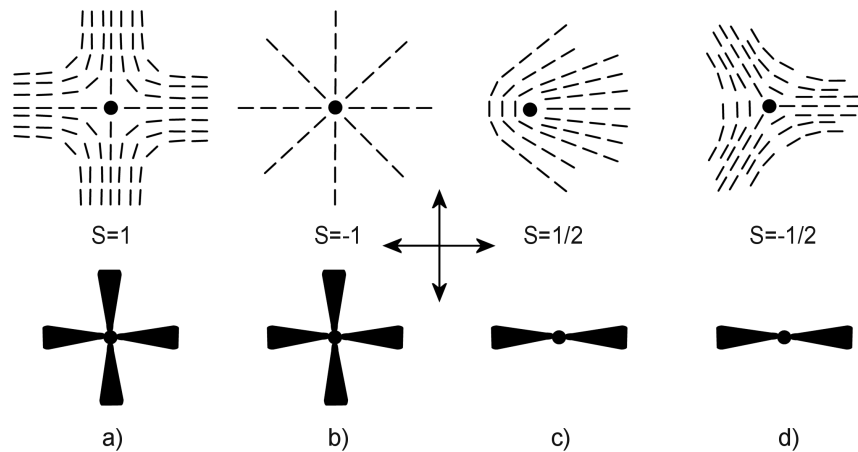
Figure 1.12: Schematics of some of the different strength defects seen in the schlieren texture of a thin film of nematic liquid crystal. The director orientation (Top row), The strength (Middle row) and The observed brush texture (Bottom row) the crossed polarizer orientation is shown as arrows in the centre of the diagram.

Closer examination of the defects under crossed polarisers reveals the brush texture in the immediate vicinity. Detailed mathematical descriptions of the director configuration have been given [55] and the strength of the defect is given as $s = \frac{1}{4}$(number of brushes) [13]. Figure 1.12 shows some of the director orientations at a nematic defect (top) and the consequential brush texture (bottom) seen when viewed through crossed polarisers. Figures 1.12a) and b) shows the $+1$ and -1 strength defects which have four brushes and figures 1.12c) and d) show the $+\frac{1}{2}$ and $-\frac{1}{2}$ strength defects which have two brushes.

1.3 Dielectrophoresis

Dielectrophoresis is the translational motion of a neutral matter resulting from polarization effects in a non-uniform field [56]. Any electric field, Uniform or non-uniform, exerts a force on a charged body. Dielectrophoresis however is known to exert a force on neutral bodies unlike electrophoresis which requires charged particles[57]. Dielectrophoresis is not really a pumping mechanism, instead it affects the hydrostatic equilibrium within a liquid [58]. It was first noticed by Pellat in his classic experiment [59] in which a dielectric liquid was seen to rise between two partially immersed parallel plate electrodes. The pumping of liquids have been achieved using dielectrophoresis in devices such as the dielectric siphon [60], but in this case the pumping of the liquid is achieved by gravity removing liquid from the system and dielectrophoresis restoring the pressure imbalance. Flow structures with millimetre spacing in the electrode dimensions usually require very high voltages $\sim 20kV$ [61] and electric field intensities that usually exceed that of air breakdown. By scaling down to much smaller electrodes, bench top experiments were performed in which a thin bead of highly insulating transformer oil was seen to rise in between vapour deposited aluminium electrodes on glass [61]. In this experiment the electrodes were planer as opposed to parallel and the finger of oil, with a semicircular cross section, rose several centimetres.

Dielectrophoresis with planer electrodes was later extended and the dielectric liquid was replaced by highly purified water. In this case the electrodes were coated with a dielectric layer to avoid electrolysis [61, 62] and down scaling of the electrode size reduced the Joule heating.

The previous work was limited to the dispensing of liquid droplets between a pair of co planer electrodes. However, it was later suggested [63] that by using an electrode array, the narrow liquid finger would be replaced by a thin film moving parallel to the electrodes.

It was suggested that dielectrophoresis could be used to separate different

types of bacteria [64]; Other uses of non-uniform electric fields to induce a dielectrophoretic (DEP) force have included the separation of breast cancer cells from blood [65] and the manipulation of bacteria with conductivity gradients [66]. Sub micron particles, including latex spheres and bioparticles, have also been manipulated and trapped using a DEP force [67–69]. All of the previous studies have relied on micro fabrication of various patterned electrodes to create the non uniform electric fields necessary.

1.3.1 Dielectrophoretic Force on Polarisable Particles

Dielectrophoresis can be compared to electrophoresis (The action of an electric field on a charged body) and figure 1.13 shows the situation for a charged and neutral particle in a non-uniform field a) and a uniform field b)
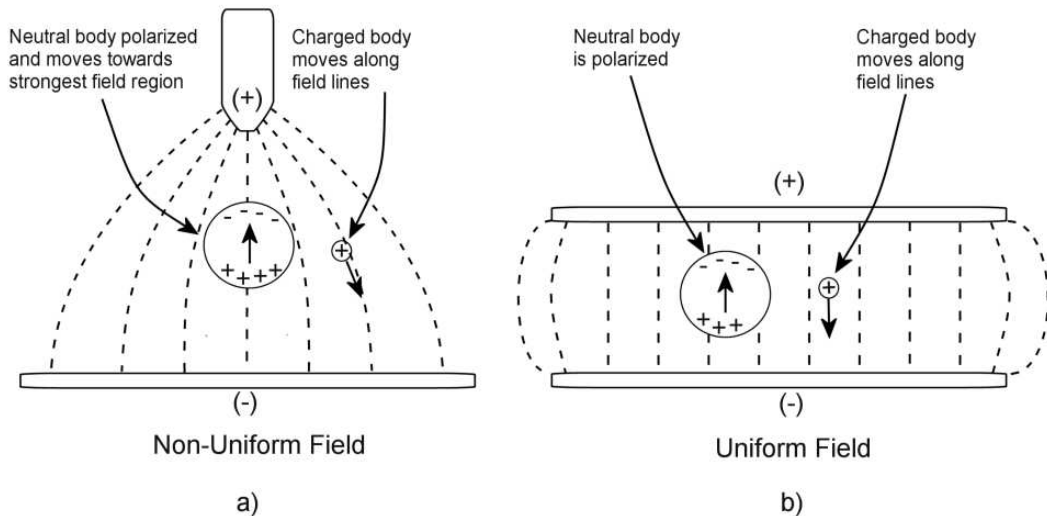
Figure 1.13: The action of a non-uniform field on both a neutral and charged particle a) and the action of a uniform field b) on said particles

In figure 1.13a) a charged particle in the non-uniform field moves along the field lines towards the plate with the opposite charge, However a neutral particle is first polarized by the presence of the non uniform field, which induces a dipole moment such that a negative charge appears near the positive electrode and a positive charge appears near the negative electrode. The particle then feels a

force towards the region of high field gradient because although the charges at opposite end of the body are equal the fields operating on the two regions of charge are not. In a uniform field (Figure 1.13b)) the neutral particle is merely polarized by the presence of the electric field but does not move, whereas the charged particle again moves along the field lines towards the plate of opposite charge.

Notice that if the polarity of the plates is changed then the neutral particle would move in exactly the same direction in a non uniform field, because the nature of the polarization would switch. For this reason the applied field generating the force could easily be an alternating electric field provided that the polarization of the body can switch as the field reverses.

1.3.2 Dielectrophoresis on a Polarizable Medium

The potential energy of a dipole is given by the equation [43]

$$U = -\mathbf{p} \cdot \mathbf{E} \tag{1.12}$$

and the Force on the dipole is given by:

$$F = -\nabla U \tag{1.13}$$

substituting equation 1.12 into equation 1.13 we get:

$$\mathbf{F} = \nabla(\mathbf{p} \cdot \mathbf{E}) = (\mathbf{E} \cdot \nabla)\mathbf{p} + (\mathbf{p} \cdot \nabla)\mathbf{E} \tag{1.14}$$

Since the dipole moment does not change with distance then $\mathbf{p}$ is constant and thus:

$$\mathbf{F} = (\mathbf{p} \cdot \nabla)\mathbf{E} \tag{1.15}$$

In the vicinity of a point in a *linear* and *isotropic* dielectric the dipole moment

per molecule is $\mathbf{p}$. If there are N molecules per cubic meter then the polarization per unit volume is given by [44]

$$\mathbf{P} = N\mathbf{p} \tag{1.16}$$

By substituting equation 1.16 into 1.15 we get the force per unit volume.

$$\mathbf{F} = (N\mathbf{p} \cdot \nabla)\mathbf{E} = (\mathbf{P} \cdot \nabla)\mathbf{E} \tag{1.17}$$

The dipole moment per unit volume of a dielectric medium can also be given in terms of the relative dielectric constant [44] where:

$$\mathbf{P} = \epsilon_0(\epsilon_r - 1)\mathbf{E} \tag{1.18}$$

Where ϵ_o is the permittivity of free space and ϵ_r is the relative dielectric constant of the dielectric medium.

By substituting equation 1.18 into 1.17 we get

$$\mathbf{F} = [\epsilon_0(\epsilon_r - 1)\mathbf{E} \cdot \nabla]\,\mathbf{E} = \epsilon_0(\epsilon_r - 1)(\mathbf{E} \cdot \nabla)\mathbf{E} \tag{1.19}$$

Using a vector identity [70] and the fact that $\nabla \times \mathbf{E} = 0$ equation 1.19 reudces to give the force per unit volume on a *linear* and *isotropic* dielectric medium in the presence of a non uniform electric field is given by

$$\mathbf{F} = \frac{1}{2}\epsilon_0(\epsilon_r - 1)\nabla \mid E \mid^2 \tag{1.20}$$

Equation 1.20 gives three important results:

1. The dielectric force is proportional to the gradient of the electric field squared. That is to say the medium is drawn to region of high field gradient

2. This force is always in the same direction irrespective of the sign of the electric field. This means that dielectrophoresis occurs in an a.c. field

3. The force is also directly proportional to the dielectric constant ϵ_r of the medium such that a larger dielectric constant will give a larger force for the same electric field.

1.4   Surface Tension

Surface tension or *inter-facial tension* is a force acting at the interface between two distinct and immiscible media. It arises because of an unbalanced force felt by the molecules at the interface. Figure 1.14 [71] shows a schematic of why this force arises. Particle B feels a force from other molecules in the bulk of the material and when this force is averaged over time the net force is isotropic, i.e. there is no particular direction. Particle A at the surface will also feel forces from other molecules within the bulk, however because of the scarcity of the molecules in the air above the interface the time averaged force will lead to a force pulling the molecule into the bulk.
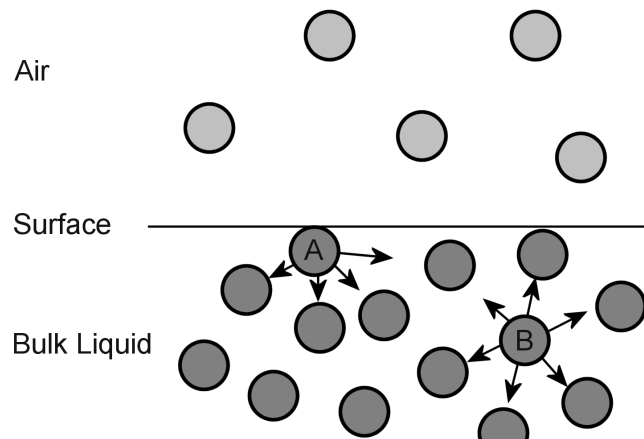
Figure 1.14: Schematic of the molecules in a liquid and the forces on two of the molecules, A at the surface of the liquid and B inside the bulk liquid

The surface tension is a restorative force and will always act to minimize the surface area of the liquid and is usually defined as a force per unit length or a force per unit area [72]. One way to envisage this is to consider a soap film stretched over a wire frame (figure1.15).

Figure 1.15: A soap film stretched over a wire frame, one end of which is movable

One end of the wire frame is movable and if the surface tension of the soap film is denoted by γ then work must be done to stretch the soap film by the amount dx. The surface tension force is restorative and the force on the sliding bar of the frame is in the opposite direction to the movement and is given by the equation:

$$Work = \gamma l dx = \gamma dA \tag{1.21}$$

Where A is the are of the soap film.

1.4.1 Contact Angle Wetting and Spreading

Another important concept regarding inter facial tension is that of a triple interface contact angle when a droplet of liquid is placed on a solid surface. Figure 1.16 shows this.

When a droplet is placed on the surface it immediately forms a spherical cap because this is the lowest surface area for the surface tension to act upon. In equilibrium i.e. the droplet is neither spreading nor contracting, the components of the interfacial tension forces along all three interfaces are in equilibrium and are governed by Young's equation:

$$\gamma_{GS} = \gamma_{LS} + \gamma_{GL} \cos\theta \tag{1.22}$$

Where γ_{GS}, γ_{LS} and γ_{GL} are the interfacial tensions between the gas/solid,
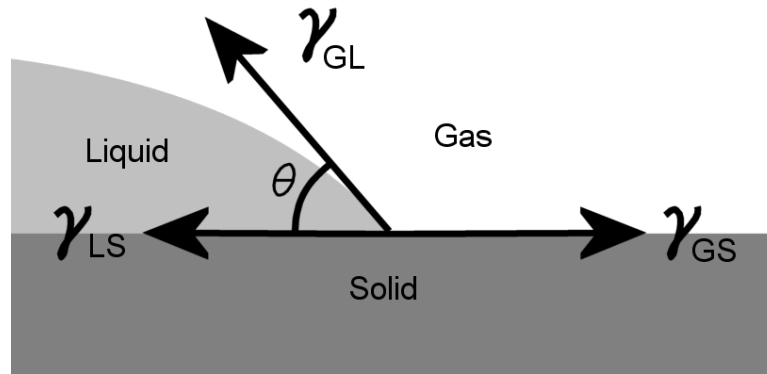
Figure 1.16: Schematic showing the triple interface formed when a droplet is placed on a surface

liquid/solid and gas/liquid interfaces respectively.

From equation 1.22 the angle θ formed a the triple interface is known as the *contact angle* and is dependent on the physical and chemical characteristics of the surface on which the droplet is placed. If $\theta < 90°$ then the surface is said to show wetting characteristics and if $\theta > 90°$ then the surface is a non wetting surface. The special case of superhydrophobicity occurs when the contact angle $\theta > 170°$.

1.5 Diffraction Gratings

A diffraction grating is a repetitive array of diffraction elements, either apertures or obstacles which have the effect of periodically altering either the amplitude, the phase or both of an incoming wavefront [45]. Tuneable gratings are of great importance in that they are able to redirect, focus or modulate light in response to a user controlled input signal [73]. Such devices include blazed gratings made from sub wavelength arrays of pillars [74], liquid crystal gratings [75–79] as well as phase gratings created by tuneably buckling gold coated elastometric surfaces or silicon sheet polymers [80, 81].

If the elements of the diffraction grating are a set of transparent and opaque

regions then it has an effect on the amplitude of the passing wave front. This type of grating is called an *amplitude grating.* On the other hand if the grating is an array of stripes with varying optical thickness then a modulation in the phase of the passing wave front occurs and this type of grating is known as a *Phase Grating.*

1.5.1 Amplitude Gratings

The *grating equation* [45] is the equation which describes the positions of the high intensity regions in the diffraction pattern created when plane waves are incident on an array of slits and is given by:

$$b \sin \theta_n = n\lambda \tag{1.23}$$

Where b is the centre to centre distance between the slits, θ_n is the diffraction angle, λ is the wavelength of the incident light and n is the order of the diffraction spot. (Figure 1.17)
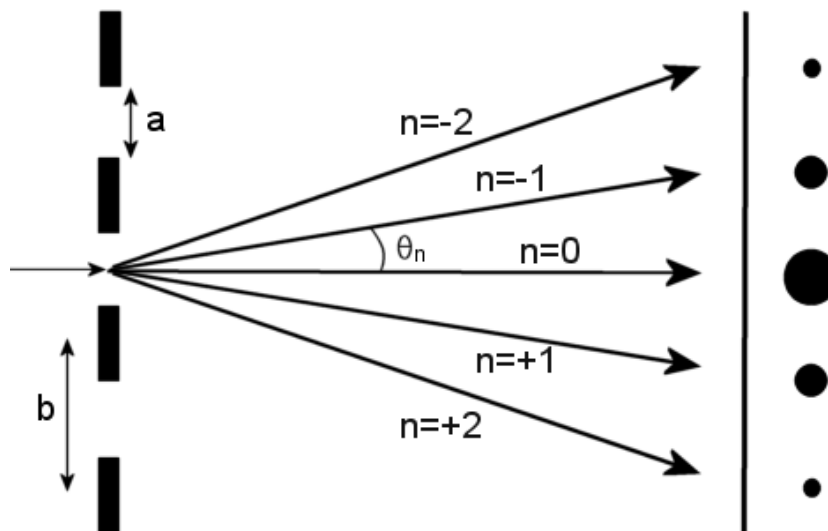
Figure 1.17: Schematic of light diffracted through an amplitude grating with N slits center to center spacing b slit width a

The intensity of the diffraction spots for a diffraction grating having N iden-

tical slits with a centre to centre spacing b and a slit width of a [45] is given by:

$$I(\theta) = \frac{I(0)}{N^2} \left(\frac{\sin \beta}{\beta} \right)^2 \left(\frac{\sin N\alpha}{\sin \alpha} \right)^2 \tag{1.24}$$

where $I(\theta)$ is the intensity at angle θ, $I(0)$ is the incident intensity, $\alpha = \frac{ka}{2} \sin \theta$, $\beta = \frac{kb}{2} \sin \theta$ and $k = \frac{2\pi}{\lambda}$ is the wave vector. The $(\frac{\sin \beta}{\beta})^2$ term in equation 1.24 is known as the diffraction envelope and governs the relative intensity of the various order diffraction spots. Figure 1.18 shows the relative intensity and positions of the zero, first and second order diffraction spots for a diffraction grating with $N = 10$ slits of width a and centre to centre spacing b. Where $b = 3a$.
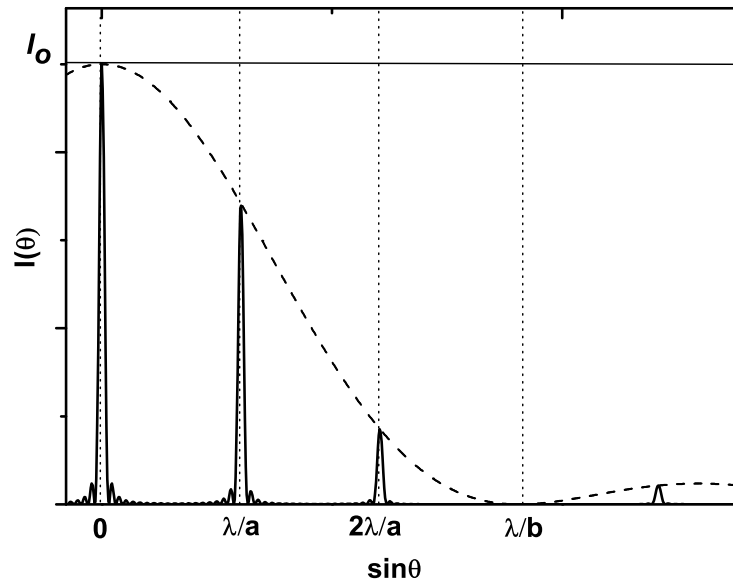
Figure 1.18: Graph showing the relative intensities of the zeroth, first and second order diffraction spots for a diffraction grating with $N = 10$ and $b = 3a$"

The important features of figure 1.18 are:

- The maxima in the diffraction pattern occur when $\sin \theta = \frac{\lambda}{a}, \frac{2\lambda}{a}, \cdots \frac{n\lambda}{a}$ as in equation 1.23

- The relative intensities of the diffraction orders are governed by the $\frac{\sin\alpha}{\alpha}$ term in equation 1.24 and this function is zero when $\sin\theta = \frac{\lambda}{b}$. It is also worth noting that if $b = \frac{a}{2}$ (i.e. the slit width is the same as the gap width) then the zero occurs at exactly the same place as the second order diffraction spot.

1.5.2 Phase Grating

A conventional phase grating (figure 1.19) consists of two materials M1 and M2 which are both transparent and have different refractive indices (Figure 1.19a). When incident plane parallel light passes through the material, a ray passing through M1 experiences a phase retardation which is dependent on the wavelength of the light, the thickness of the material and the refractive index of the material. The phase retardation of light in a particular material is given by the equation.

$$\delta\phi = \frac{2\pi t n}{\lambda} \tag{1.25}$$

Where t is the thickness of the material, n is the refractive index of the material and λ is the wavelength of the light incident on the grating.
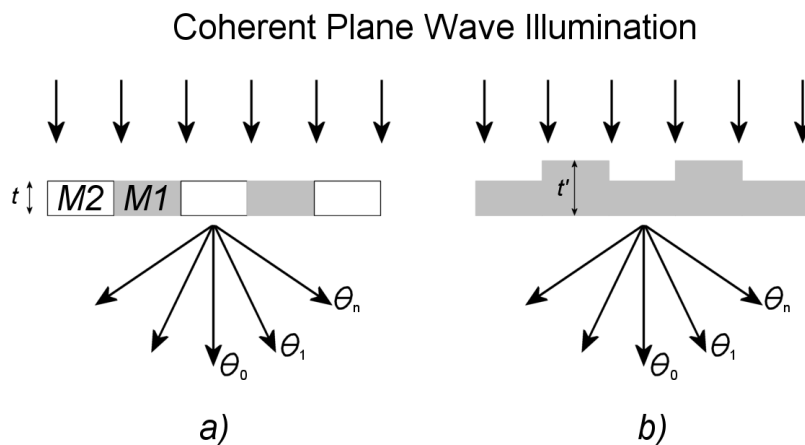
Figure 1.19: Schematic of two types of phase grating a) a grating with two different materials of different refractive index and b) a grating of one material with a periodic variation in thickness

If material 2 has a different refractive index to that of material 1, the light passing through M2 will have a different phase retardation to that of the light passing through M1. This phase retardation of the light results in interference of the emergent light which leads to a diffraction pattern in far field. In this respect the incident light is diffracted into the higher order diffraction spots where the diffraction angle $\theta_0 \cdots \theta_n$ depends on the periodic variation of different material properties and the diffraction angles are again given by the *Grating equation.* (Section 1.5.1). The phase lag created in a light ray (equation 1.25) is also dependent on the thickness of the material in question.

So for a wave front travelling trough a grating made from two materials with periodically varying refractive index (Figure 1.19a) the phase difference is given by the equation

$$\delta\phi = \frac{2\pi t n_1}{\lambda} - \frac{2\pi t n_2}{\lambda} \Rightarrow \delta\phi = \frac{2\pi t(n_1 - n_2)}{\lambda}$$

Alternatively, for a wave front travelling through a medium of singular refractive index but with a periodically varying thickness (Figure 1.19b). The path difference is given by:

$$\delta\phi = \frac{2\pi t_1 n}{\lambda} - \frac{2\pi t_2 n}{\lambda} \Rightarrow \delta\phi = \frac{2\pi t(t_1 - t_2)}{\lambda}$$

In this sense a phase grating can be produced by a periodic variation in thickness in a material with a single refractive index or a grating with periodically varying refractive index.

If the phase difference between light rays passing through regions of different thickness or refractive index is π radians, destructive interference occurs between the light rays and the maximum amount of incident light is diffracted from the zero order into the higher order diffraction spots. It should be appreciated that this situation can arise by either correct choice of the refractive index difference between the two materials used in the grating (Figure 1.19a) or by the correct

thickness difference between regions of the same refractive index (Figure 1.19b).

1.5.3 Fourier Optics

For a linear system [45] of plane waves incident on an aperture, the *Fraunhofer* or *far-field* diffraction pattern created on a distant object can be approximated by performing a Fourier Transform on the transmission function at the aperture.

In general any periodic function $f(x)$ can be written as the sum of an infinite Fourier series [45].

$$f(x) = \frac{A_0}{2} + \sum_{m=1}^{\infty} A_m \cos mkx + \sum_{m=1}^{\infty} B_m \sin mkx \qquad (1.26)$$

The coefficients A_m and B_m are found using

$$A_m = \frac{2}{\lambda} \int_0^\lambda f(x) \cos mkx dx \qquad (1.27)$$

$$B_m = \frac{2}{\lambda} \int_0^\lambda f(x) \sin mkx dx \qquad (1.28)$$

We can consider a diffraction grating as the square function wave centred about the origin. Since the function is centred on the origin it has even symmetry therefore the constants B_m are all zero and the series expansion of the square function can be written as.

$$f(x) = \frac{4I_0}{\pi} \left[\cos kx + \frac{1}{3} \cos 3kx + \frac{1}{5} \cos 5kx \cdots \right] \qquad (1.29)$$

Where I_0 is the intensity across the aperture and $k = \frac{2\pi}{\lambda}$

The coeficients of A_m in equation 1.29 are 1, $\frac{1}{3}$, $\frac{1}{5}$ $\cdots$ and represent the relative intensities of the diffraction spots. Notice that the even terms in the expansion of the square wave have completely disappeared. In real term this means that one would expect there to be no second, fourth and sixth etc order diffraction spots in the pattern. This coincides with figure 1.18 where $a = 2b$ and the diffraction

envelope is zero at the same position as the second order diffraction spot.

1.5.4 Thin Sinusoidal Phase Grating

As stated in section 1.5.2 a phase grating can be created by use of a material in which the thickness varies periodically. This kind of grating has previously been created by reflecting a laser at a grazing angle from the surface of liquid in which a surface ripple is created by means such as mechanical and thermal agitation [82–84]. If incident light is transmitted through the liquid, the periodic sinusoidal variation in the thickness of the material would lead to a sinusoidal variation in the optical path length of light traversing the material. This would also lead to a sinusiodal variation in the phase lag of light normally incident on the grating.

The Fraunhofer diffraction pattern of a thin sinusoidal phase grating can be found by performing a Fourier transform on the aperture function[85] and the diffraction angles are governed by the same equation as an amplitude grating where the spacing between slits is now replaced with the wavelength of the sinusoidal surface profile Λ i.e.

$$\Lambda \sin \theta = n\lambda \tag{1.30}$$

However the relative intensities of the various order diffraction spots are dependent on the difference in optical path length between the peaks and troughs of the sinusoid or the amplitude of the sinusoid.

It can be shown [85] that the variation in the intensities of the diffraction spots is proportional to the Bessel function

$$\eta_q = J_q^2 \frac{m}{2} \tag{1.31}$$

Where η_q is the diffraction efficiency of the qth order diffraction spot, J_q is a Bessel function of the first kind and m is the optical path length difference relative the amplitude of the sinusoidal surface. Figure 1.20 [85] shows the diffraction

efficiency of an ideal thin sinusoidal phase grating. Where q is the order of the diffraction spots.

The thin sinusoidal grating deflects energy from the zero order spot into the higher order spots and it should be noted that no power is absorbed by this kind of grating. The power appearing in the various orders is merely the sum of that which is incident on the grating and as the optical path length varies then so does the amount diffracted into the various order spots. Also the maximum achievable power diffracted into the first order spot is 33.8% [85].
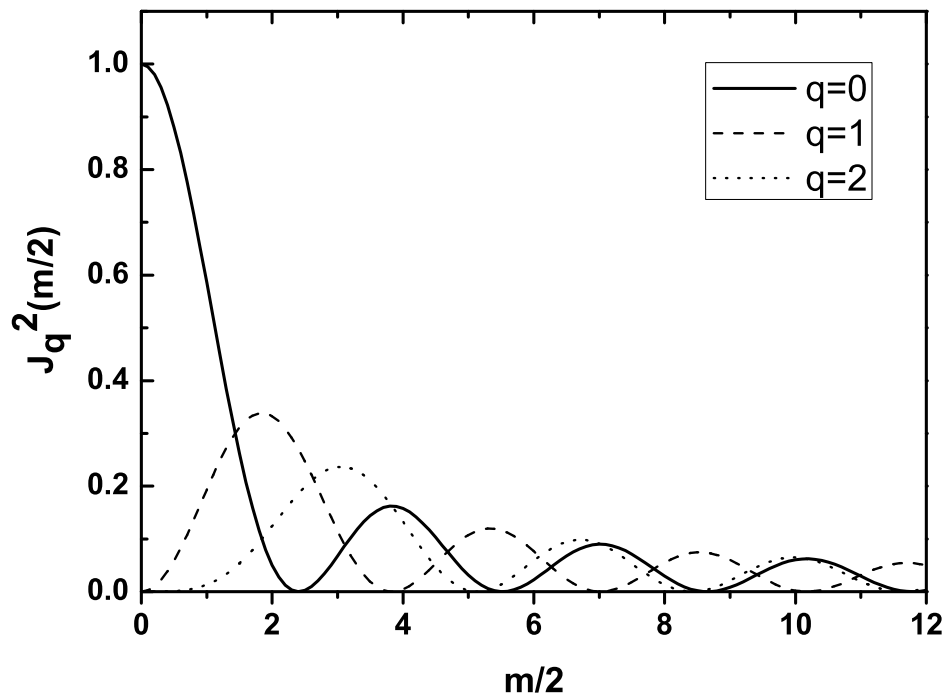
Figure 1.20: Diffraction efficiency $j_q^2(\frac{m}{2})$ versus $(\frac{m}{2})$ for three values of q

The roots and the maximums of the Bessel function from figure 1.20 are shown in table 1.1[86].

Table 1.1: The roots and maxima of the Bessel function shown in figure 1.20

	First Order	Second Order	Third order
min	2.41	0	0
max	3.83	1.84	3.05
min	5.52	3.83	5.13
max	7.02	5.33	6.71

Chapter 2

Experimental Techniques and Methods

The devices created using the methods in this chapter are shown in figures 2.1 and 2.2. The liquid crystal device consists of two pre coated borosilicate glass plates, into which electrodes have been etched. Both plates are coated with a 2μm layer of SU8-10 Photo resist and the droplet itself is confined inside a box, which is patterned into a 15μm layer of SU8-10 photo resist, such that it is centred between both sets of electrodes,

The dielectrophoretic phase grating consists of a set of interdigitated electrodes which are etched into a borosilicate glass substrate, pre coated with Indium Tin Oxide. This is then coated with a 2μm layer of SU8-10 and the oil layer is formed when a droplet is placed above the electrodes on the SU8 surface, under an applied electric field.
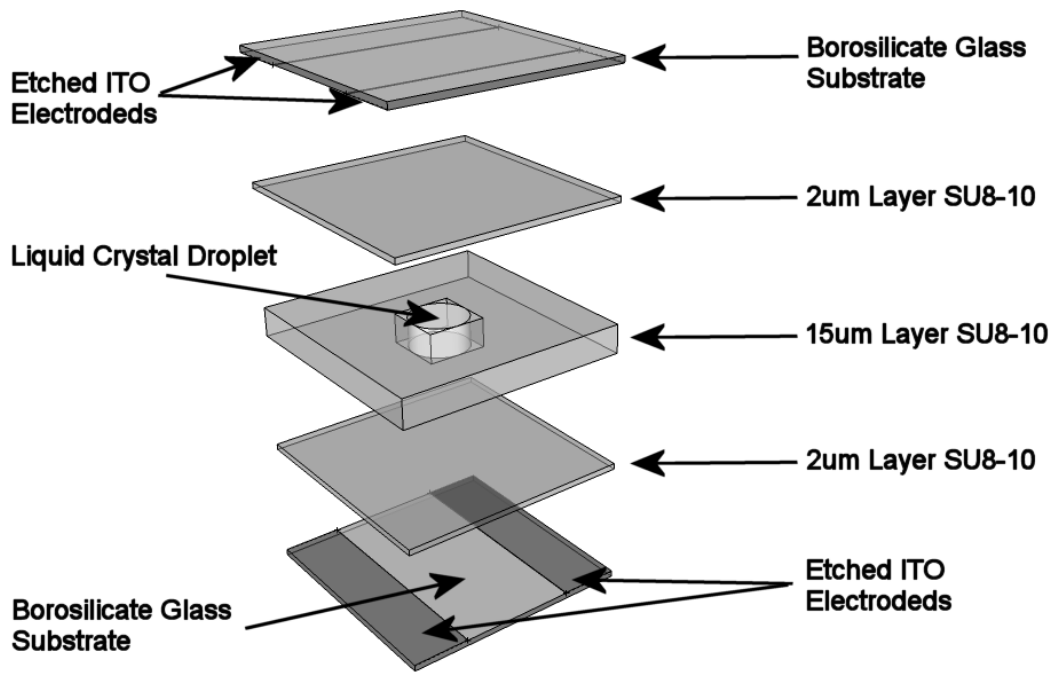
Figure 2.1: an exploded Schematic drawing of the Liquid crystal device used in this study.
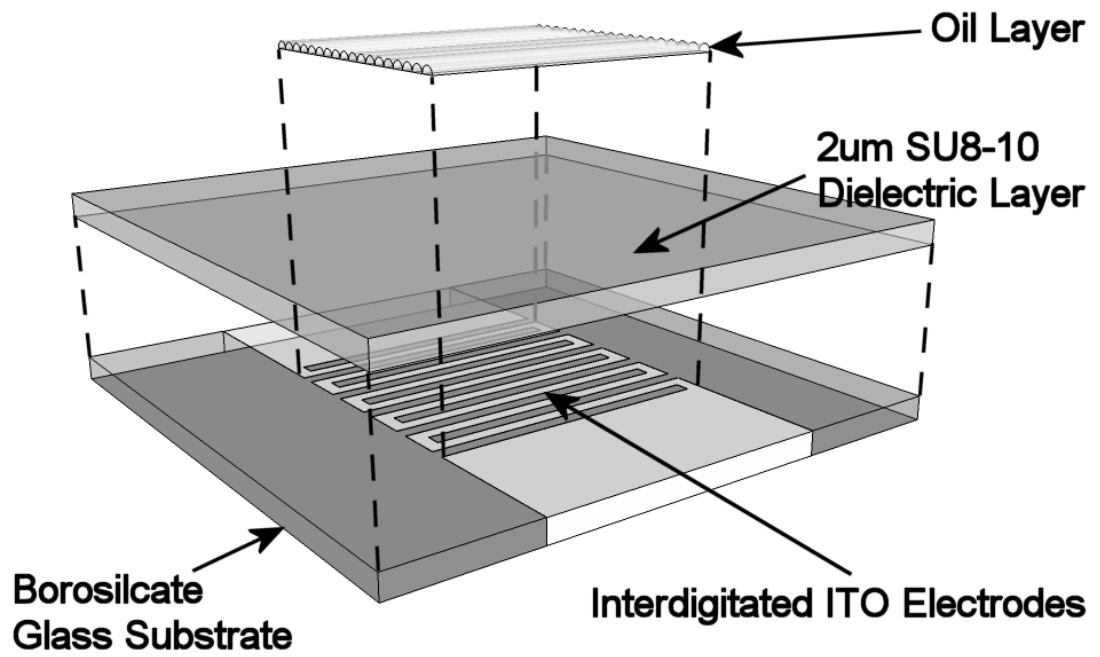
Figure 2.2: An exploded Schematic drawing of the Dilectrphoretic phase grating device used in this study.

2.1   S1813 Photo Lithography and ITO electrode Etching

The electrodes used in the devices use an interdigitated pattern of electrodes, of the type commonly used in biological particle manipulation [44, 64, 87] in which the spacing between the electrodes is a same as the width of the electrodes. Figure 2.3 shows a schematic of the electrode layout of an interdigitated pattern. They were fabricated using a Photolithographic process with Shipley S1813® [88]. Figure 2.4 shows a schematic of the processing involved in creating the electrodes. A borosilicate glass substrate, pre coated with an Indium Tin Oxide (ITO) transparent conductor, (Figure 2.4 a), was spin coated with S1813 on a Laurell WS-6505-6NPP spin coater at 500 rpm for 5 seconds and then increased to 3000 rpm for 30 seconds to give a layer of 1.5μm thickness,(Figure 2.4 b). This layer is then baked at 105° for 75 seconds on an EMS 1000-1 hotplate and the substrate is then allowed to cool. After cooling to room temperature the layer was exposed to UV light for 1.4 seconds through the patterned mask, containing the interdigitated electrode pattern, using a MicroTec SUSS MJ4B Mask aligner (figure 2.4 c). The substrate was then developed in a 50/50 mixture of Microdev developer solution and de-ionized water where the pattern of the electrodes is transferred into the S1813 layer (Figure 2.4 d). After developing the substrate was immersed in a bath of 0.5M Oxalic acid and allowed to etch for 8 Minutes. The acid etching removes the ITO coating in areas not covered with S1813 leaving only the pattern of electrodes required. After etching the remaining S1813 photo resist was then washed away using Acetone to leave only the electrode pattern (Figure 2.4e).
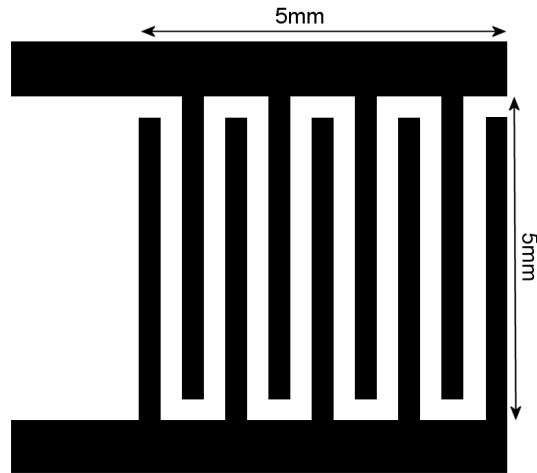
Figure 2.3: Schematic drawing of the interdigitated electrode pattern. The total electrode area is 5mm*times*5mm. However, the dimensions of the ividual electrodes depends on the mask used. The spacing in between the electrodes is the same as the electrode width.
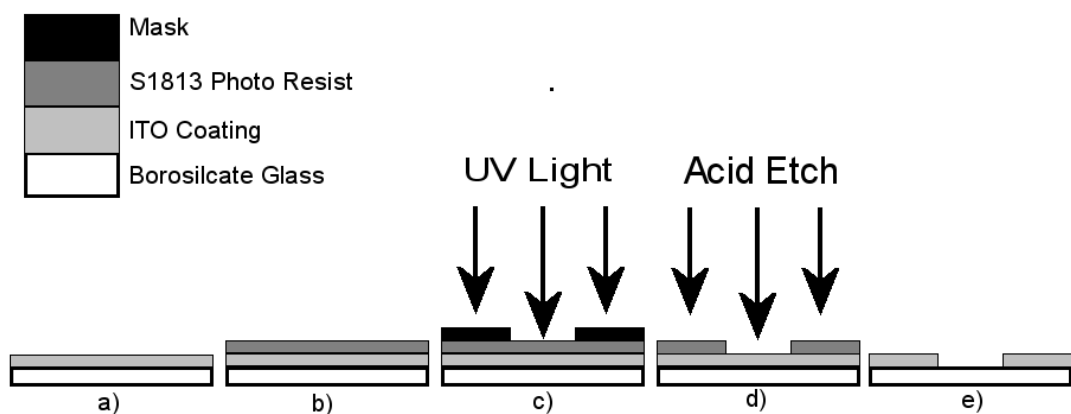
Figure 2.4: Schematic of the S1813 Photo lithography process a) ITO coated borosilicate glass substrate b) with S1813 photoresist layer c) exposure through a mask d) developed pattern etching e) resulting Pattern

2.2 S1813 Photo Lithography and Gold Sputtered Electrodes

In section 5.7 a dielectric stack coating was used in the dynamic studies of the diffraction device. The electrodes used in this experiment are created using the same Photolithographic process as in section 2.1, however, because the device was to be used in reflection, it was important that the periodic variation in the reflective dielectric stack coating, imparted by the thickness of the underlying electrodes, be minimised. Thus, in order to reduce the thickness of the electrodes they where sputter coated with a 10nm layer of gold. Since sputter coating occurs in exposed regions of glass as opposed to the removal of ITO in exposed regions, a negative mask was used to give the reverse pattern of the electrodes required, See Figure 2.5, and after pattern development the sample was sputter coated with TiO_2 for 24 seconds and Au for 15 seconds. This gives the electrodes a thickness of 10nm measured using a Pacific Nonotechnology Nano-R2 AFM.
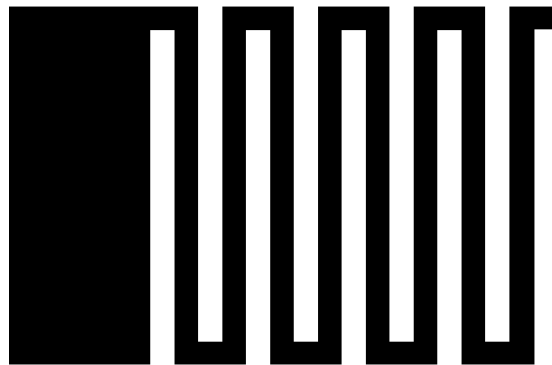
Figure 2.5: Schematic of the negative mask used in the production of gold sputtered electrodes

2.3 SU8-10 Photo Lithography

SU8-10 is a negative photoresist and was used as a dielectric layer in the manufacture of the devices used for experiments in chapter 5 and 6 and in the production of the box architectures used to confine liquid crystal droplets.

2.3.1 SU8-10 Processing

Figure 2.6 shows a schematic of the SU8 Photolithographic process. First a thin layer of SU8 of the required thickness was spin coated onto a substrate (Figure 2.6a) and b). This layer was then baked on a hot plate to promote the evaporation of the solvent before being exposed through a patterned mask (Figure 2.6 c). After exposure the layer was baked to promote polymerization, developed in PGMA developer and washed with Isopropylalcohol. This removes the parts of the layer which have not been exposed to the UV light and leaves only the areas exposed to the UV light. The pattern created depends on the mask used, see sections 2.1 and 2.2
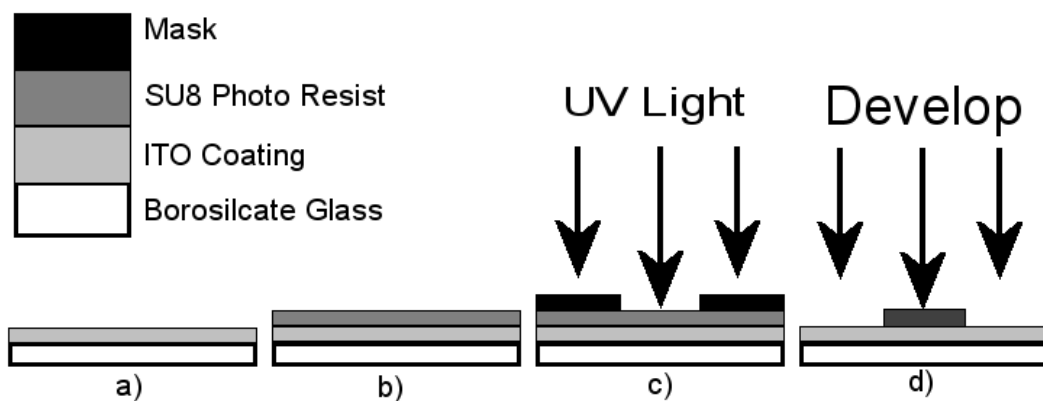
Figure 2.6: Schematic of the SU8 Photo lithography process a) ITO coated borosilicate glass substrate b) with SU8 photoresist layer c) exposure through a mask d) developed pattern

2.3.2   Creating boxes for Liquid crystal droplets

The process of creating a box to confine the liquid crystal droplet was a three stage process consisting of creating a base layer, creating the walls and finally filling and capping.

Creating a base Layer

A borosilicate glass substrate, containing pre etched electrodes (section 2.1) was spin coated with a 50% solution of SU8-10 diluted in its own developer at 500rpm for 5 seconds and then raised to 2000rpm for 30 seconds. The resulting 2μm layer was then pre baked at 65° C for 2 minutes and then ramped to 95°C at 20°/min. Once this temperature is reached the sample is baked for a further 2 minutes. It is then allowed to cool slowly and after cooling the layer is exposed to UV light, at 50mW/cm^2, for 6 seconds. The sample is baked for a further 2 minutes at 65°C and ramped at 20°C/min to 95°C for a further 2 minutes after which it is allowed to cool to room temperature.

Creating the walls

In order to create the walls of the box to confine the droplet, a 15 μm layer of SU8 was spin coated onto the existing 2μm base layer. The same baking time, temperatures and spin regime used to create the base layer was followed. However, the SU8-10 50% solution was replaced with pure SU8-10 and the exposure time was changed to 4 pulses of 3.3 seconds with a reduction filter inserted into the mask aligner to reduce the flux to 30mW/cm^2 . A mask was also inserted into the mask aligner, which was patterned with an array of squares. The baking process was the same as the previous 2μm layer but after the post bake the substrate was developed in PGMA developer for 3 minutes. The sample was finally washed in Isopropylalcohol to remove any remaining SU8-10. This Process created an array of square holes in the second layer of SU8-10. Figure 2.7 shows a scanning

electron microscope image of the box before filling with E7 liquid crystal.
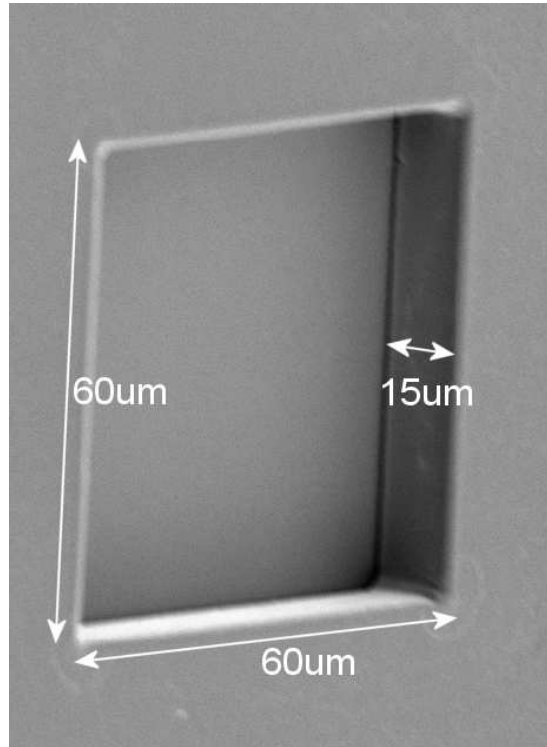
Figure 2.7: Scanning Electron Microscope Image of the SU8 box before filling and capping

Filling and capping

In order to fill the square wells with E7 liquid crystal the lower substrate containing the array of square holes was placed on a hot plate at 65°C and a thin layer of E7 liquid crystal was spread onto the surface with a pipette. To create the top substrate a second Piece of borosilicate glass, with pre-fabricated electrodes, was then spin coated with a 50% dilute solution of SU8-10 for 5 seconds at 500rpm and then ramped to 2000 rpm for 30 seconds to create a 2μm layer. Before any baking processes took place, and whilst the layer was still wet, the top plate was inverted, positioned above the base substrate and pressed into place. The relative orientation of the electrode to each other depended on the device. Two types of device were studied one of which had the electrodes oriented at 40°" and one with electrodes oriented at 90°". The device was then placed in a metal clamp

and the whole device structure and clamp placed on the hotplate for 2 min at 65°
and then ramped at 20°C/min to 95°C for 2 minutes. The whole device was then
removed from the clamp and exposed at 50mW/cm² for 6 seconds. The device
was finally placed back in the clamp and baked at 65°C for two minutes and 95°C
for 2 minutes to harden the top layer and seal the device together.

After capping and filling the device edge are glued using araldite glue to fur-
ther strengthen the bond between plates and wires are soldered to the electrodes
to allow the device to be addressed.

2.3.3 Creating a dielectric layer for the dieletophoretic phase grating

The dielectrophoretic phase grating was fabricated by etching a set of electrodes
onto an ITO coated Borosilicate glass substrate (section 2.1). The resulting
electrode set was then coated with a 2μm thick dielectric layer of SU8-10. This
was done by spin coating a 50% solution of SU8-10 in its own developer at 500rpm
for 5 seconds and 3000 rpm for 30 seconds. The substrate is then pre exposure
baked (PEB) for 1 minute at 65°C and ramped to 95°C at 20°C/min and left
for 2 minutes. After the PEB the layer is exposed to UV light for 6 seconds
to promote polymerization. After exposure It is subjected to a post exposure
bake for 2 minutes at 65°C and again ramped at 20°C/min to 95°C where it is
baked for a further 5 minutes. A final baking at 175° for 30 minutes is employed
to promote further polymerization of the surface and results in a much harder
dielectric surface. After the surface preparation the whole device is allowed to cool
slowly, to prevent shrinkage and cracking of the surface and wires were soldered
to the relevant contacts using ITO solder.

2.4 Device Addressing Techniques

The experimental setup for the analysis of the liquid crystal droplet devices is shown in figure 2.8. The device itself was placed on a Linkam LTS350 microscope temperature stage controlled by a Linkam TMS 94 temperature controller. Heat sink compound was applied to the surface of the device to allow better thermal conduction with the stage. The stage was placed in a Canon BX51 optical microscope and viewed with crossed polarisers in place. The voltages were applied to each individual set of electrodes using a TTi TGA1242 2 channel arbitrary waveform generator with each signal being amplified 100 times with a Trek PZD350 piezo amplifier. The image from the microscope was captured using a JVC TKS350 analogue video camera and transmitted to a monitor. An acetate mask containing gradations of 5° was attached to the monitor screen to allow easy reading and setting of the angle of rotation.
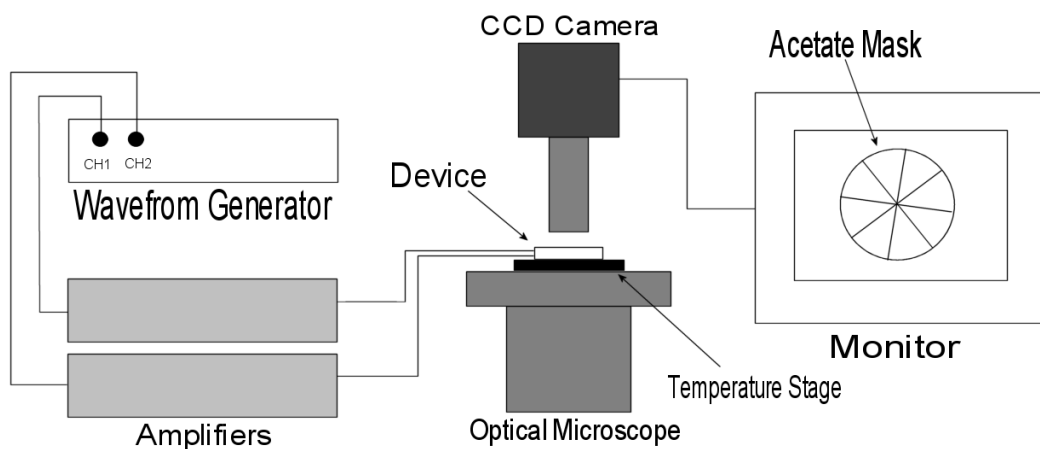
Figure 2.8: Schematic diagram experimental setup used to measure the angle of rotation of a liquid crystal with a variation in voltage at different temperatures

2.4.1 Pulsed rotation of Liquid crystal droplets

The pulsed rotation of the liquid crystal droplet was achieved by applying a burst of a 10kHz sine wave with variable amplitude to either set of planer electrodes (Figure 2.9). The number of complete sinusoids in each burst was varied allowing

44

the burst duration to be calculated.
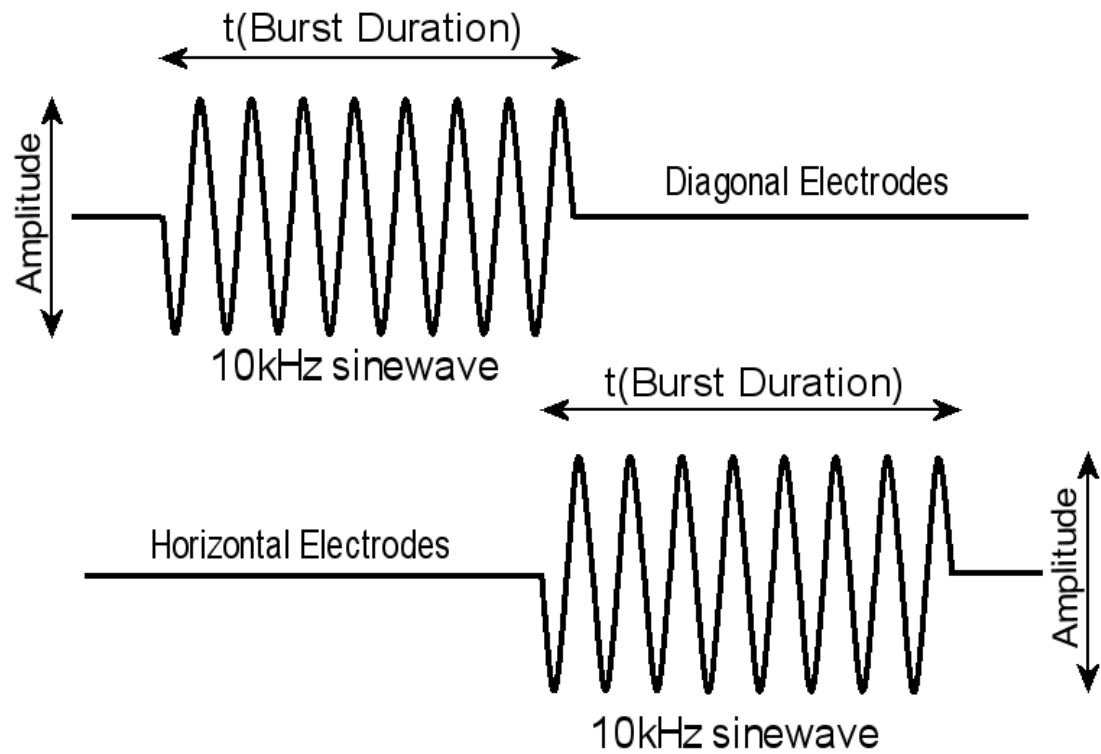
Figure 2.9: Schematic diagram of the application of burst voltages to the liquid crystal droplet

2.4.2 Continuous rotation of Liquid Crystal droplets

A rotating electric field, in the plane of the electrodes was created by modulating a 10kHz sinusoidal driving signal, applied to each electrode set, with a second signal with variable amplitude and frequency. By introducing a phase difference of 90° between the signal applied to each set of orthogonally oriented electrodes, a rotating electric field was generated in the plane of the electrodes with a variable amplitude and frequency of rotation.The resulting wave forms were amplified with a Trek PZD350 Amplifier (figure 2.10).

2.4.3 AC addressing of Dielectrophoretic Phase Grating

The experimental setup for the testing of the Dielectrophoretic phase grating is given in figure 2.12. A TTi TGA1242 two channel arbitrary waveform generator
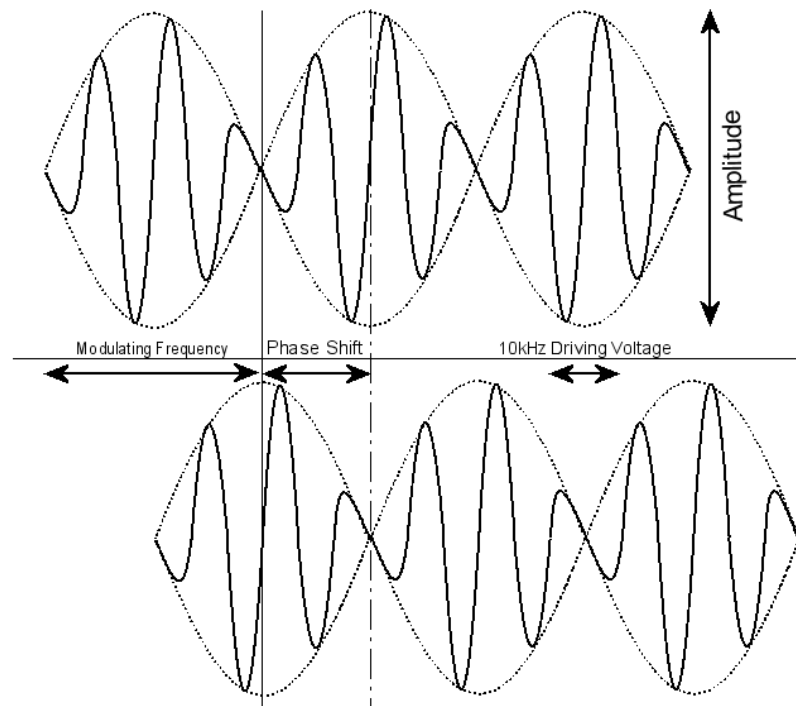
Figure 2.10: Schematic diagram of the application of a rotating electric field to the liquid crystal droplet

was used to create an AC 10Khz Signal with alternate electrodes having an ac bias of V_0(rms) and the interdigitated alternate electrodes were earthed. The signal was amplified 200 times using a Trek PZD700 piezo amplifier. This signal was then applied to the electrodes of the sample as in figure 2.11. The sample was placed in one arm of the interferometer (a full description of the Interferometer is given in section 2.5) and the resulting interferogram from the CCD camera was passed to a laptop computer for storage and analysis.

2.4.4 Modulated Addressing of Dielectrophoretic phase grating

For the measurements of the intensity of the different order diffraction spots and for the measurements of the switching time of the device, the a.c. signal applied to the electrodes was modulated with either a triangular or a square wave. This allowed for the amplitude of the applied voltage to increase and decrease linearly
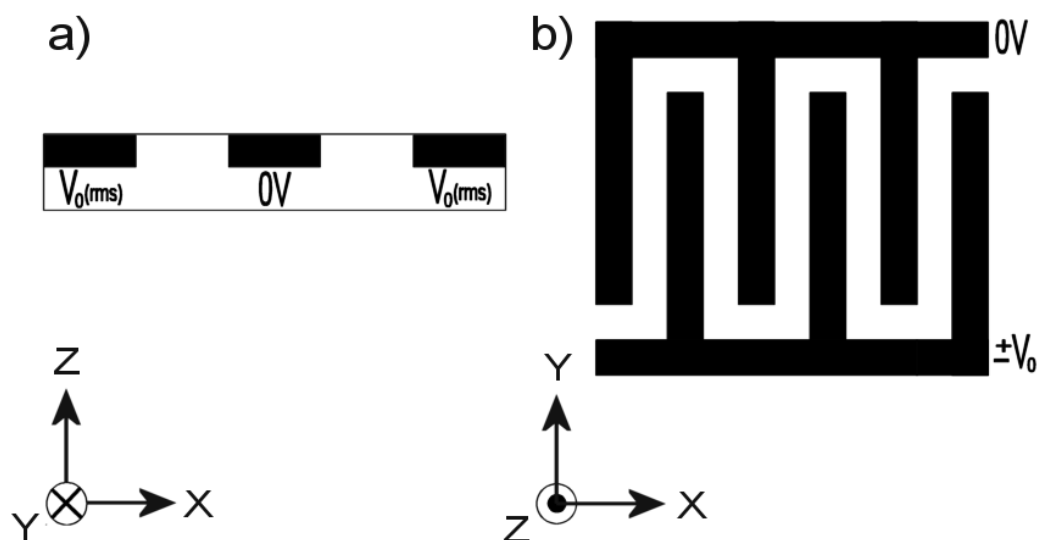
Figure 2.11: Schematic diagram of the application of an AC voltage to the electrodes in the dielectrophoretic phase grating
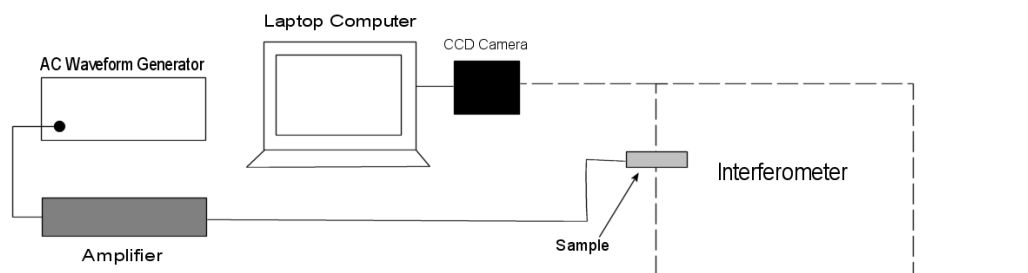
Figure 2.12: Schematic diagram of the experimental setup for the application of an AC voltage to the electrodes in the dielectrophoretic phase grating whilst in the interferometer.

with the period of the modulating waveform. The amplitude of modulating wave was adjustable such that the minimum and the maximum values required for a particular experiment could be set, see figure 2.13
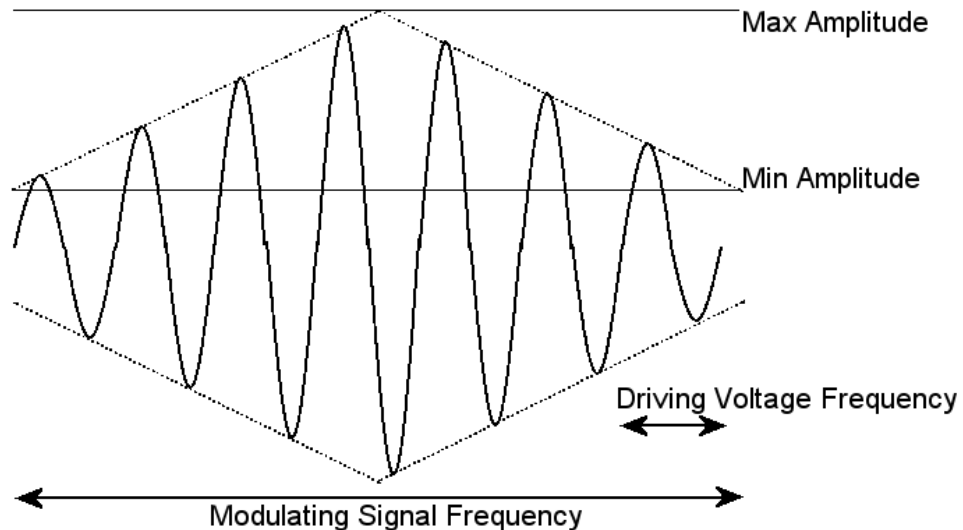
Figure 2.13: Schematic diagram of the application of an AC voltage to the electrodes in the dielectrophoretic phase grating with a triangular modulating signal

For switching speed experiments (section 5.8) the triangular modulating waveform was changed to a square wave. This allowed the applied voltage to be switched discontinuously between the maximum and minimum voltage required for a particular experiment.

2.5 Interferometry

The Mach-Zehnder Interferometer is essentially a two beam interference technique which is used to measure the changes in optical path length created by a sample introduced in to the sample beam. Figure 2.14 shows how the wavefronts travel through the interferometer. In perfect alignment the wavefronts of both beams are reflected twice and transmitted once and arrive at the detector exactly in phase, see Figure 2.14a. This condition would effectively create no interference fringes. By introducing a slight tilt angle into the reference beam the wavefronts emerging from the last beam splitter are slightly out of phase in some regions and
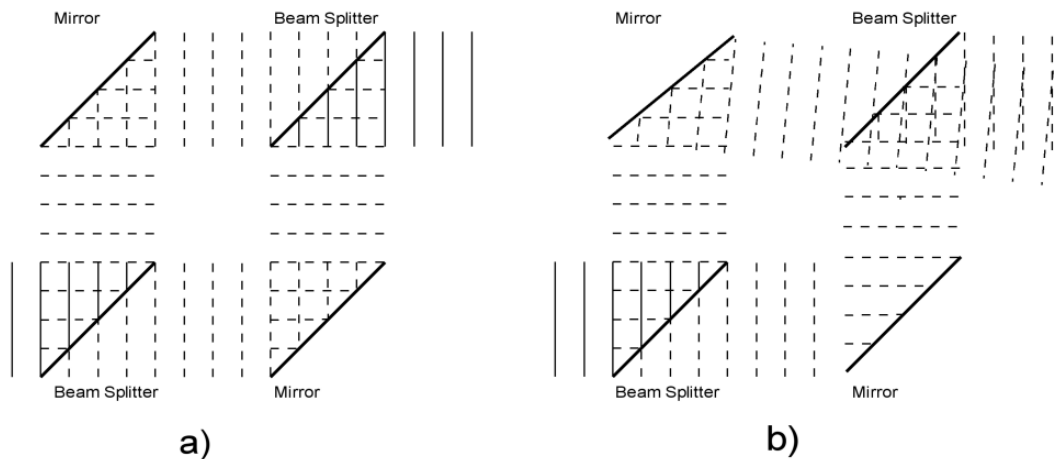
Figure 2.14: Schematic diagram showing how the wavefronts travel through the Mach-Zehnder Interferometer and create tilt fringes. a) the mirrors are beam plitters are perfectly aligned leading to no phase difference in any of the beams and no interference pattern is seen. b) The introduction of a slight angle into one of the beams leads to a phase delay in some regions of the beam creating an interference pattern.

in phase in others (Figure 2.14 b)). This variation in phase difference between the two causes parallel interference fringes localized in the plane of the sample.

2.5.1 Experimental Setup

The Mach-Zehnder interferometer (Figure 2.15) used consists of a 17mW HeNe laser source which is then spatially filtered to give a broad beam with a Gaussian distribution, which is cropped such that the intensity varies very little across the beam. The beam passes through a 50/50 beam splitter where the beam is split into a reference beam and a sample beam. A slight angle is introduced between the two beams before being recombined at the second beam splitter. This creates interference fringes which are then imaged with the CCD camera. The relay lens system allows the localized fringe pattern to be transferred to the CCD camera. The sample can also be imaged in normal light whilst in situ in the interferometer by placing a back light into the sample arm behind the sample. The device to be measured is placed in the sample arm of the interferometer and as such changes the optical path length of the sample beam further and this additional difference

in the optical path length causes the fringes to shift. An example image can be seen in figure 2.15. By measuring the relative shift of the fringes and having a knowledge of the refractive index of the oil, it is possible to determine the change in surface height of the sample. See section 2.5.4
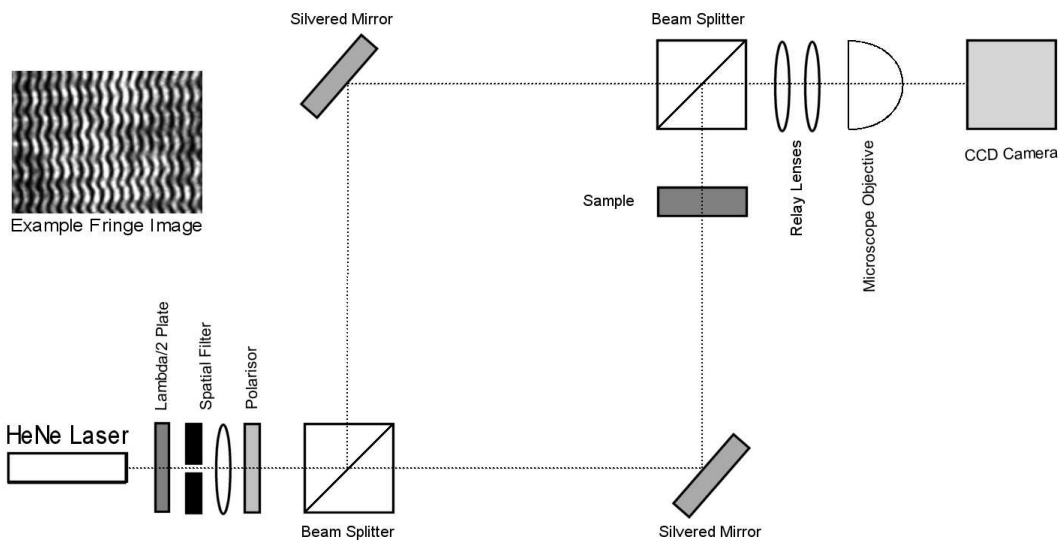
Figure 2.15: Schematic diagram of the Mach-Zehnder interferometer used to Measure the oil surface undulation

2.5.2 Reading the Interferograms

With a sample introduced into one arm of the interferometer, the tilt fringes created by the introduction of an angle between the reference beam and the sample beam is modified further. By orienting the sample such that the electrodes run orthogonally to the tilt fringes, the periodic change in optical path length, caused by the spatial variation in the sample created by the undulation of the oil surface, creates a rippling effect on the interference fringes. Figure 2.16 shows a schematic of how the fringes vary when a voltage is applied to a sample. Since the axis of the undulation is aligned with the tilt fringes any change in the surface height causes a shift to the left or right in the fringes (Figure 2.16 b).
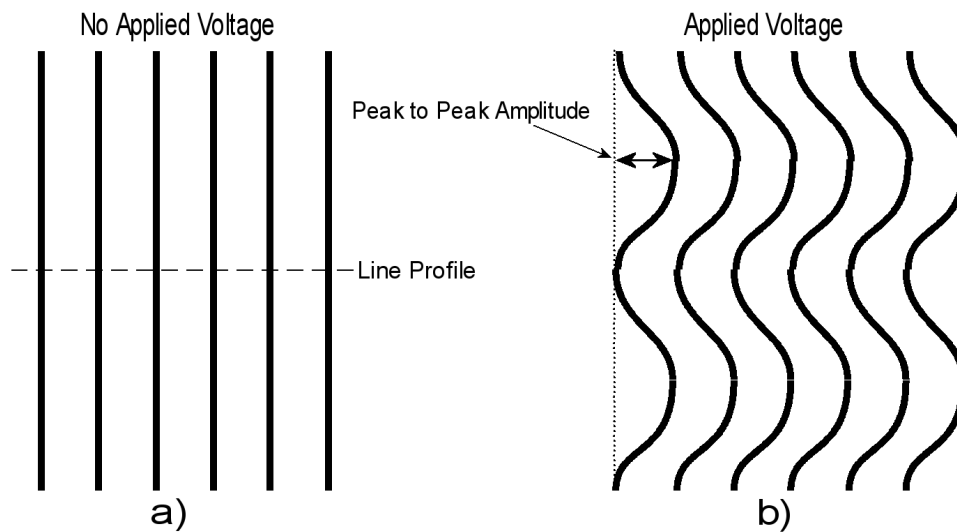
Figure 2.16: Interferograms of the Surface undulation created by the application of a voltage. a) zero volts and b) Under voltage

2.5.3 Measuring the Fractional Fringe Shift

The fringe shift of the interferograms is measured using image processing. The raw interferograms (Figure 2.17 a) are imported into ImageJ. It is first smoothed with the standard smoothing tool on the ImageJ tool bar (Figure 2.17 b). It is then converted into an 8 bit black and white image and then the threshold adjusted with a lower threshold level of 0 and an upper threshold level of 115 (Figure 2.17 c). From the resulting image six fringes are selected from the centre and the image is cropped to show only those six fringes. Any artefacts from the other fringes at the edge of the cropped image, or remaining artefacts from thresholding, are removed leaving only the six fringes to be measured, Figure (2.17 d).

After the image processing the average spacing between the fringes is calculated by plotting the grey value profile for the line across six fringes, and taking the average difference between the minima. To calculate the relative fringe displacement, as a fraction of a fringe width, the peak to peak amplitude of the fringe is measured (Figure 2.16 b) and this value is divided by the average fringe width.
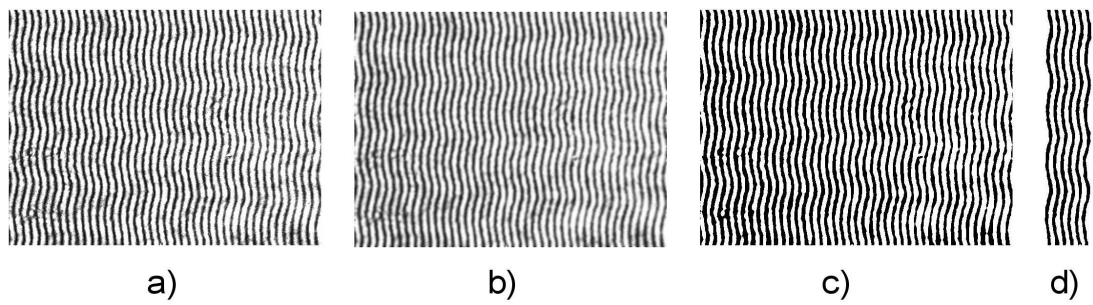
Figure 2.17: a) Raw Interferogram b) smoothed interferogram c)Thresholded interferogram d) Six remaining Fringes

2.5.4 Surface Height Change
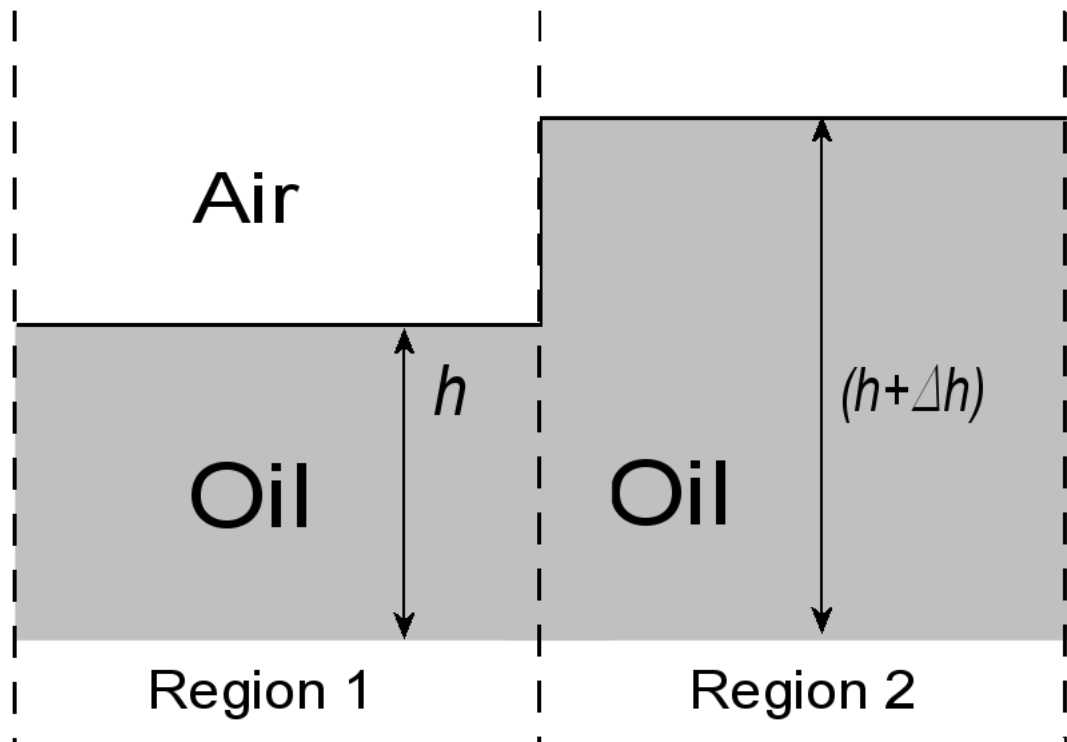
Figure 2.18: Schematic of the optical path taken through a sample with a surface height change

The relative shift of the fringes as a fraction of a fringe width can be converted into a surface height change by considering the different regions through which the light is travelling. In figure 2.18 we can see that in region 1 where the light travels through the oil for a distance h and through air for Δh the optical path

length $\mathbf{k}\boldsymbol{.}\mathbf{r}$ is given by the equation

$$\mathbf{k}\boldsymbol{.}\mathbf{r} = \frac{2\pi}{\lambda_0}(h.n_{oil} + \Delta h.n_{air}) \tag{2.1}$$

where $\mathbf{k}$ is the wavevector $\frac{2\pi}{\lambda_0}$, $\mathbf{r}$ is the distance traveled in a particular medium and n_{oil} and n_{air} are the refractive indices of the oil and air respectively. λ_0 is the wavelength of the laser used, in the case of the interferometer λ_0=632.8nm.

In region two the optical path length is given by

$$\mathbf{k}\boldsymbol{.}\mathbf{r} = \frac{2\pi}{\lambda_0}((h + \Delta h).n_{oil}) \tag{2.2}$$

The difference in optical path length is 2π moving from one dark fringe to the next or

$$\frac{2\pi}{\lambda_0}((h + \Delta h)n_{oil} - (h.n_{\text{oil}} + \Delta h.n_{air})) = 2\pi \tag{2.3}$$

by rearranging equation 2.3 an equation for the height change represented by a shift, left or right, of one fringe can be obtained.

$$\Delta h = \frac{\lambda_0}{n_{oil} - n_{air}} \tag{2.4}$$

So, by calculating the number of a fringes shifted on the interferogram and taking into account the refractive indices of air and the oil used it was possible calculate the corresponding change in the height of the surface. i.e.

$$\Delta h = N_f \times \frac{\lambda_0}{n_{oil} - n_{air}} \tag{2.5}$$

Where N_f is the number of fringes shifted by a particular fringe.

2.6 Optical Diffraction Pattern Measurements

The optical diffraction pattern created by the Dielectroporetic phase grating was measured in situ in the interferometer. This allowed the Undulation of the surface to be imaged in the interferometer, whilst at the same time the diffraction pattern, created by either transmission through the sample, or reflection from the bottom surface of the sample, could be measured.

2.6.1 Transmission

In this experiment a second beam splitter was introduced into the sample arm of the interferometer. This allows the red 632.8nm laser light for the interferometer to pass and also allows for the introduction of a green laser (λ=543nm)into the same path (Figure 2.19). This laser beam was then reflected by a silvered mirror and directed to a photo diode. The voltage output of the photo diode was read into a multimeter linked to a Lab view computer program. The photo diode is also attached to a movable swing arm such that the angle can be scanned across the diffraction pattern. A plot of the intensity versus the positive and negative angle from zero can then be obtained. The central pivot of the swing arm is offset behind the reflecting mirror such that the offset distance is the same as the distance from the sample to the mirror. This compensates for the 90° changes in the diffraction pattern and allows the angles to be measured accurately.

2.6.2 Reflection

The diffraction pattern measurements were carried out using the interferometer setup in Figure 2.20. A beam splitter is introduced above the recombining beamsplitter and the green laser is then positioned such that the light enters the beamsplitter and travels on to the sample where it is reflected off the dielectric stack coating and back to the beam splitter. The diffraction pattern created by the device is then reflected at 90° toward the photodiode as in the transmission
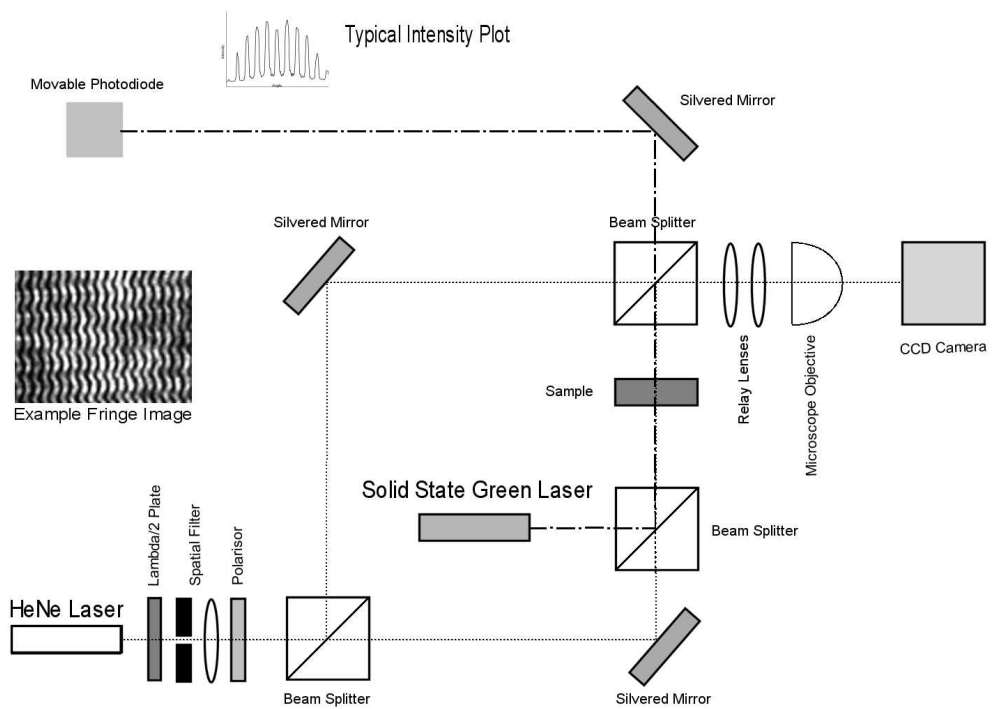
Figure 2.19: Schematic of the inteferometer with the introduction of a second laser for diffraction pattern measurments

experiments.
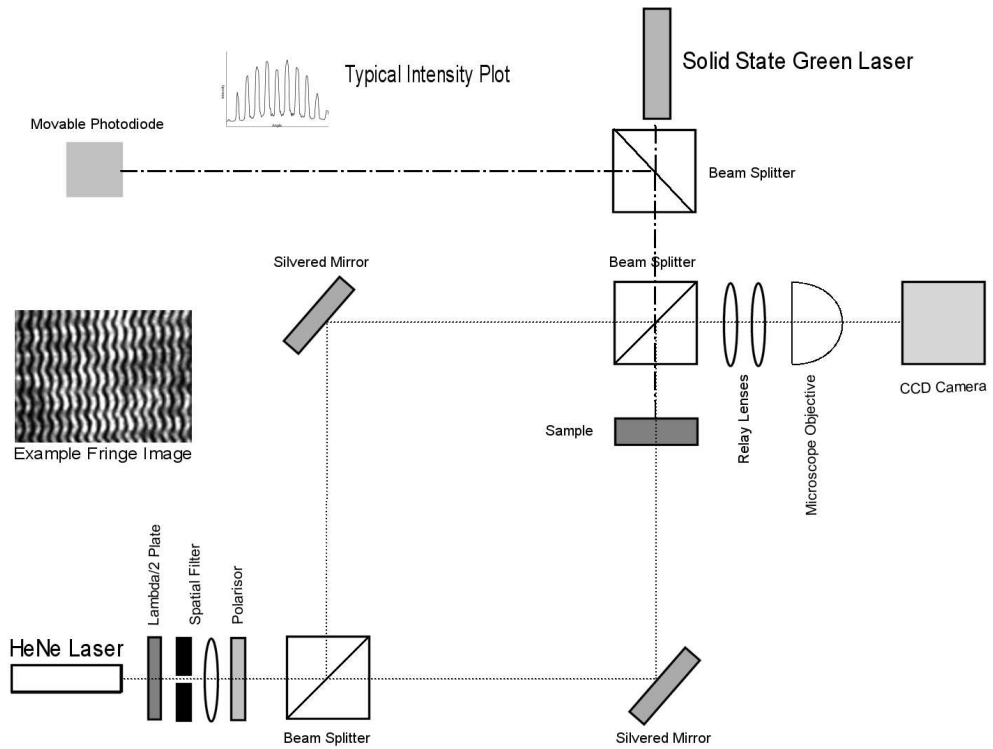
Figure 2.20: Schematic of the inteferometer with the introduction of a second laser for diffraction pattern measurments

Chapter 3

Multi Stable Nematic Liquid Crystal Wave plate

3.1 Introduction

A nematic liquid crystal droplet has been confined in a square well such that it forms a circular disc shape with edges formed by the meniscus of the liquid crystal. The optical texture of the droplet has been examined using crossed polarization microscopy and the most likely orientation of the n-director has been deduced and shown to be a bipolar configuration. The confining box is positioned such that it lies between interdigitated electrodes etched into a layer of ITO on a borosilicate glass substrate and oriented at 40° to each other. By applying electric fields in the plane of the electrodes it was possible to reorient the director in the droplet. The rotation time of a circular droplet is shown to follow the linear relationship $\theta = 0.472\tau V^2$ and also to exhibit multistability. The temperature of the droplet affects the shape and size of the droplet and in cases where the side walls of the well begin to affect the shape the V^2 relationship no longer applies. Non-circular droplets have also been seen and the most likely director orientation has been deduced. These droplets are shown to exhibit orientations similar the that seen in other work and again it has been possible to switch these multi stable

droplets between a variety of states using different electric field amplitudes and orientations.

3.2 Device Construction

Figure 3.2 shows the device in which a nematic liquid crystal droplet was formed by confining a small amount of liquid crystal in an array of boxes with dimensions $60\times60\times15\mu$m. A microscope image of the device taken in reflection without crossed polarisers and with a $200\times$ magnification is shown in Figure 3.1. Since the electrodes have a higher reflective coefficient than glass they appear as light regions in the image and it can be seen that the pixel under test lies directly between both the horizontal and diagonal sets of electrodes. The interdigitated electrodes are oriented at $40°$ to each other and were etched into a 50 nm layer of ITO on a borosilicate glass substrate using the technique in section 2.1. The electrodes used on both the upper and lower substrates have a geometry of 120μm electrode width and 120μm spacing. The confining array was created using the procedures given in section 2.3.2 and performs two important functions. Firstly, it defines the positions of the droplets relative to the electrode positions and, secondly, it segregates an otherwise continuous layer of liquid crystal into small droplets. The meniscus of the liquid crystal droplet is continuous about the circumference of the droplet and does not rupture when it comes into contact with the confining walls at lower temperatures. The shape of this free surface is however changed at lower temperature.

Figure 3.2 shows a schematic drawing of the device. a 2μm layer of SU8-10 photo resist also coats the electrode on the upper and lower substrates. This was created using the techniques in section 2.3.2 and imparts a random planar alignment to the liquid crystal [35].
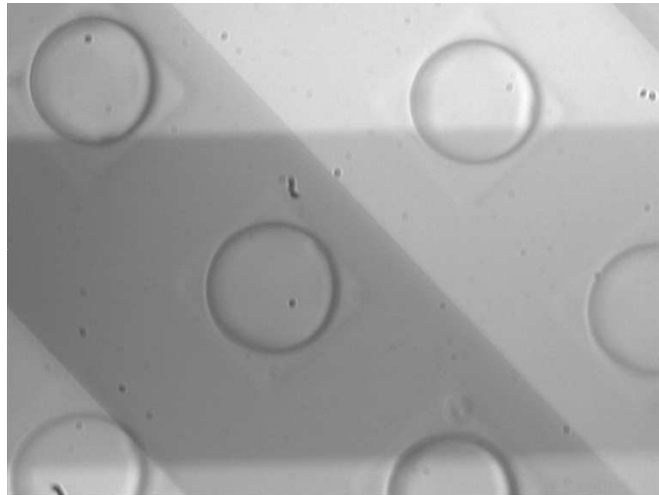
Figure 3.1: Microscope image showing a circular droplet of liquid crystal and its orientation in the electrode system. The electrodes can be seen as the lighter regions which surround the droplet
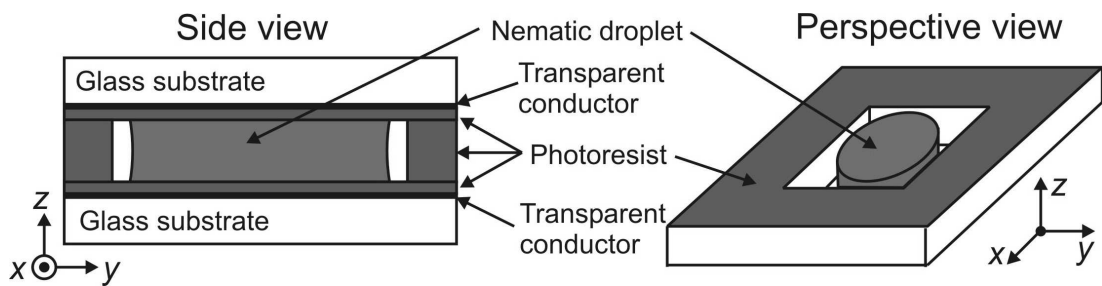
Figure 3.2: Schematic of the device containing the liquid crystal droplet

3.3   Orientation of the Optical Axis

The droplets confined in the array formed circular discs with a diameter of 50μm and a thickness equal to that of the box height, of 15μm. This geometry for the confining box of the liquid crystal is chosen such that the director lies in the plane of the layer [89] and results in the optical texture seen in figure 3.4. For this radius of droplet, 50μm, the nematic alignment is kept significantly in the plane of the substrate provided that the thickness of the droplet is not increased above 25μm. [26] for the thickness of our cell, 15μm, the anchoring forces at the SU8 surface become more important. also at this thickness if the diameter of the droplet is increased above 100μm the liquid crystal can form a random planar schlieren texture [90]

3.3.1   Optical Texture

Figure 3.3 shows the droplet at the centre of figure 3.1. The images were taken using transmitted light with $500\times$ magnification. Figure 3.3a shows the pixel oriented in the vertical direction, by applying a burst of a.c. voltage of 10 V_{rms} at 10 kHz to the horizontal electrodes, whilst figure 3.3b shows the pixel oriented in the diagonal state by applying the same burst to the diagonal electrodes. Since the layer of liquid crystal appears dark between crossed polarisers when the director is either parallel or perpendicular to the crossed polarisers (section 1.2.8) The cross shape of the brushes in figure 3.3a has two fold symmetry and indicates that the director is parallel or perpendicular to the crossed polarisers in this central "cross" region of the image. When the droplet is rotated to the diagonal state the brushes are seen at the top and bottom of the droplet and on the left and right hand side of the droplet. This indicates the director orientation at these positions is now aligned with the crossed polarisers.

Also in figure 3.3a the free edge of the droplet appears to have two dimple features at the top and bottom of the droplet. These features are moved to

the upper right and lower left quadrant when the droplet is switched and could correspond to the presence of nematic disinclinations.
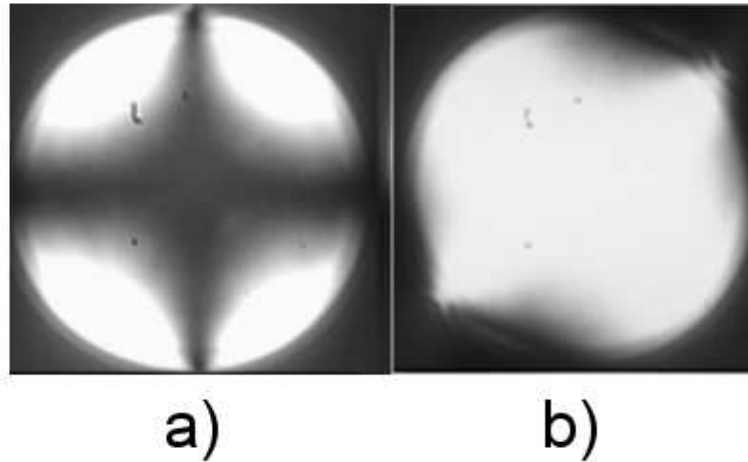
Figure 3.3: Image of the Droplet at the centre of Figure 3.1 in the vertical a) and diagonal b) states. The crossed polarisers are aligned vertically and horizontally

Figure 3.4 shows multiple microscope images of the nematic droplet at the centre of figure 3.1 between crossed polarisers. The orientation of the cross polarisers for each image is given in figure 3.4b). The top right image and the bottom left image of each set of nine images correspond to the crossed polarisers being oriented at +45° and -45° and the image at the centre correspond to the crossed polarisers being vertical and horizontal.

In figure 3.4a) when the crossed polarisers are rotated through 45° the brushes sweep out towards the edge of the droplet separating in the middle. The dark brushes now occur to the left and right of the defect at the top and bottom of the droplet. In figure 3.4b) the dark brushes initially start on the top bottom and left and right of the droplet. When the crossed polarisers are rotated through 45 ° they form the dark cross seen in figure 3.3a) but now tilted at 45°.

Figure 3.5 shows the pixel at different orientations and subject to an AC voltage. Figure 3.5a) shows the start position of the pixel; figure 3.5b) shows the pixel during the application of the burst to the horizontal electrodes; figure 3.5c) after the voltage is removed; figure 3.5d) on application of the burst to the diagonal electrodes; and figure 3.5e) after the voltage is removed and the final
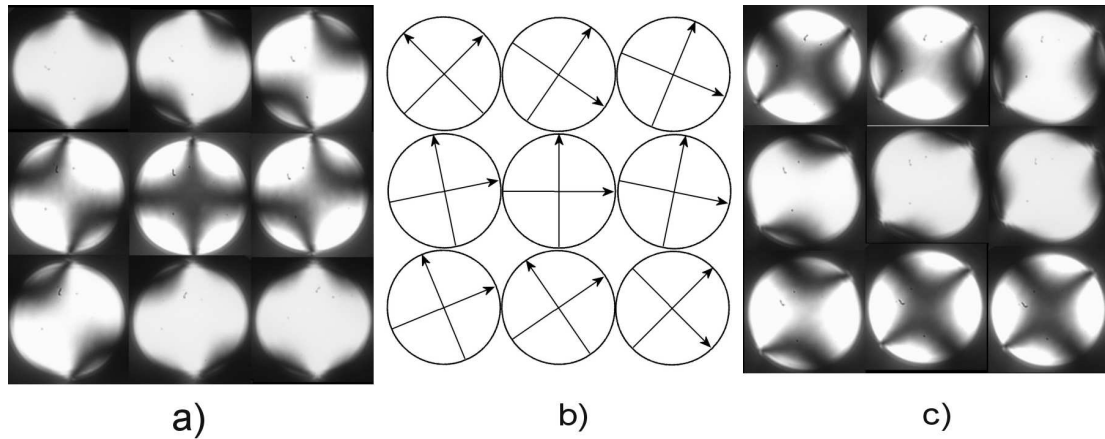
Figure 3.4: Microscope image showing a circular pixel under cross polarisers at different angles. a) the pixel switched to the horizontal state b) the position of the cross polarizers c) the pixel switched to the diagonal state

state of the pixel.
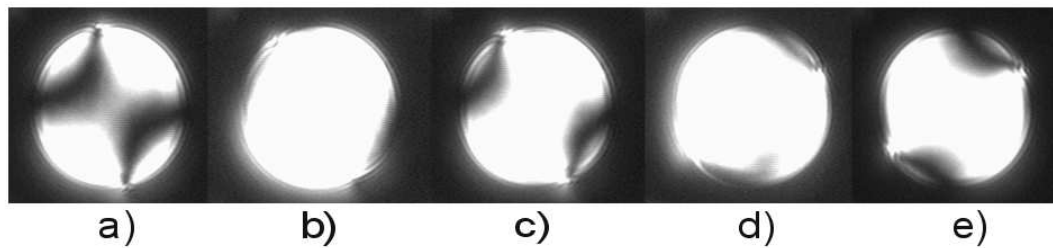
Figure 3.5: Microscope image of the droplet taken through cross polarisers and switched to two relative positions a) zero volts b) 10V, 10kHz applied to horizontal electrodes c) zero volts d) 10V, 10kHz applied to diagonal electrodes e) zero Volts all switched at room temperature.

It is clear from figure 3.5 that the orientation of the optical axis, as shown by the cross texture of the brushes, after the application of the electric field lies primarily in a direction parallel to the electric field. Since The nematic material E7 has a positive dielectric anisotropy, $\Delta\epsilon = \epsilon_{\parallel} - \epsilon_{\perp} > 0$, where $\epsilon_{\parallel}$ is the permittivity parallel to the n director and $\epsilon_{\perp}$ is the permittivity perpendicular to the n-director, the director will tend to align itself parallel to the electric field. This would indicate that the n-director is substantially vertical through the centre of figure 3.4a). There are three possibilities for the director orientation at the free surface of the droplet; homeotropic; Planar or tilted orientations [91].

The external air outside the droplet can be classed as an isotropic fluid [13]. The tilted orientation of the director at the interface is unlikely, since it would not give rise to the cross shape pattern in the brush pictures. The two possible director profiles in which the director orientation is planar and homeotropic at the droplet edge is shown in figure 3.6. The planar polar configuration has been seen previously in cylindrical cavities in optical fibres [23, 24] and in anopore and nuclepore membranes [25]. However, the fact that when this occurs the nematic disinclinations are also in line with the electric field, the most likely orientation for the director within the droplet is that given in figure 3.6a) This bipolar orientation has been seen in previous studies of polymer dispersed liquid crystal (PDLC) droplets [26, 27] where the droplets are spherical. The droplets in this study could be seen as a cross section through a spherical droplet.
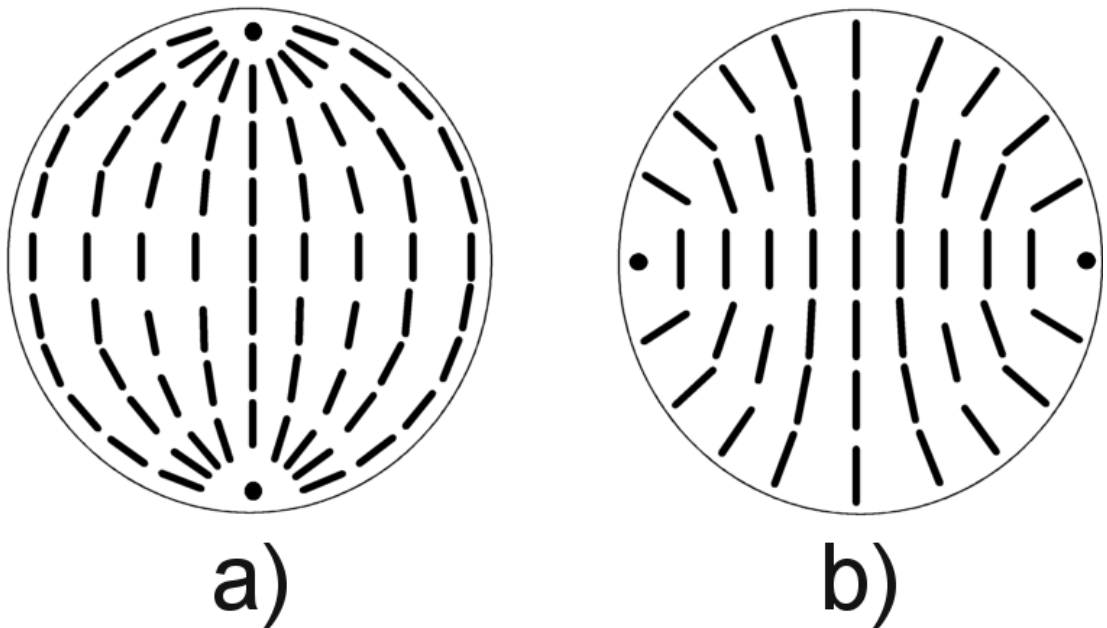
Figure 3.6: Schematic of the two possible director orientations which would give rise to the cross shaped brush texture seen in the LC droplets. a) Bipolar orientation b) planer polar configuration

3.3.2 Rotating the Director

By varying the rms amplitude of the voltage burst, it was also possible to rotate the optical axis of the droplet to other arbitrary stable states. In order to test the rotation characteristics of the droplet the device was placed in an optical microscope under crossed polarisers whilst a voltage was applied. The setup for the experiment is shown in figure 2.8 and the experimental technique is given in section 2.4. By varying the amplitude and burst duration of the applied electric field the angle of rotation of the optical axis was found to be controllable to an accuracy of 1°. The amplified signal voltage was applied to the sample in order to rotate the optical axis from the vertical state by a fixed number of degrees for several different voltages. Measurements are shown in figure 3.7 for rotations of 1.25°,2.5°,5.0° and 10.0°. The start point for each set of measurements was the vertical state shown in the centre of figure 3.4a) and after each reading the device was reset to this state by the application of a 5 second burst 20V a.c. 10kHz signal to the horizontal electrodes.

Figure 3.7 shows the burst duration, on a logarithmic scale, plotted against the voltage applied between the diagonal electrodes. This data is taken from the droplet shown in figure 3.3, however the same general trend was seen in a total of four different droplets. The best lines of fit, from regression analysis, for each angle are plotted as continuous lines. The same equation was found to fit all the data and this is given by equation 3.1

$$\theta = 0.0472\tau V^2 Degrees \tag{3.1}$$

The best line of fit for the data in figure 3.7 was obtained from the plot in figure 3.8 which shows a plot of τ/θ versus $1/V^2$ and a regression analysis of this graph gives the equation of best fit as

$$\frac{1}{V^2} = (0.00028 \pm 0.00006) + (0.0472 \pm 0.0008)\frac{\tau}{\theta} \tag{3.2}$$
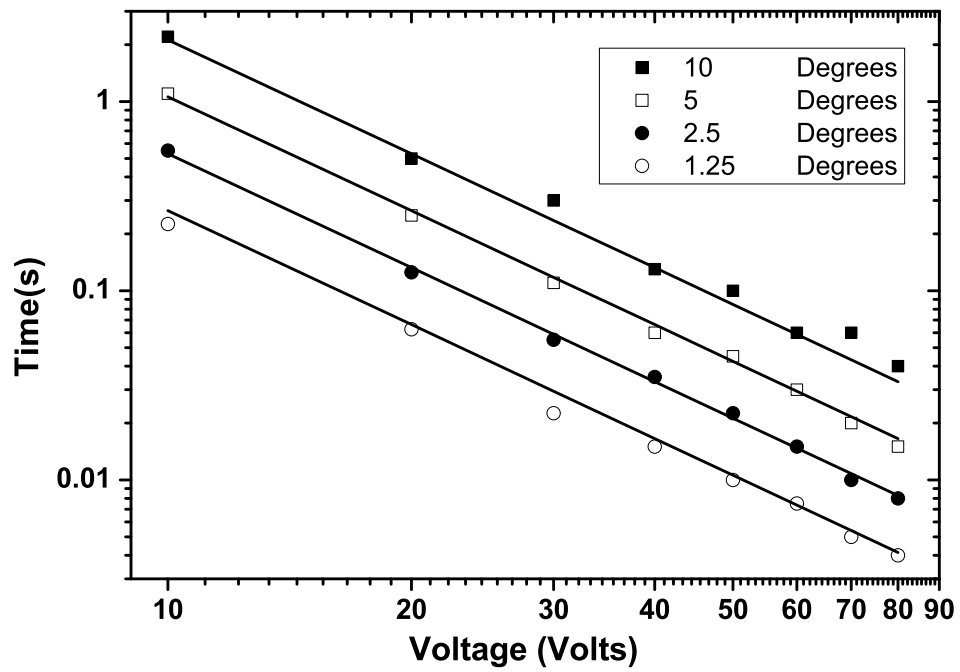
Figure 3.7: Graph showing the pulse duration at 10kHz for switching a pixel Through different angular rotations
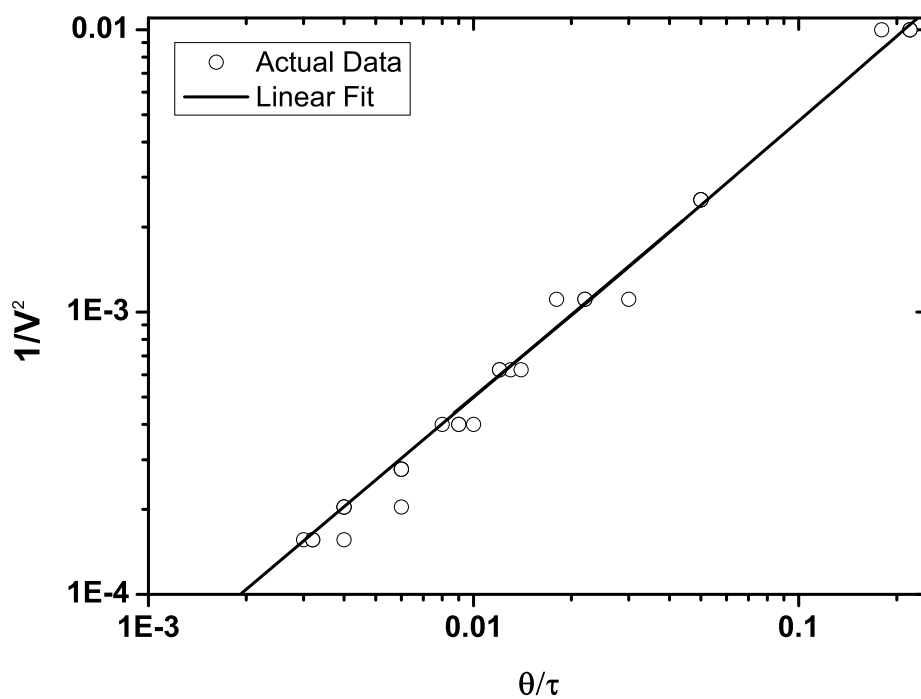
Figure 3.8: Graph showing $1/v^2$ versus θ/τ for data shown in figure 3.7

The dependence of θ on the square of the voltage can be explained with reference to the Gibbs electrostatic energy of a system, $W = -(\frac{1}{2})\mathbf{D} \cdot \mathbf{E}$ For a nematic liquid crystal material, this leads to a torque for rotation of the n-director which is proportional to the square of the electric field and to the dielectric anisotropy $\Delta\epsilon$. The time evolution of the n-director can be described using dynamic nematic continuum theory. With a single rotational viscosity γ_1. [92] A simplified form this theory is given in equation 3.3 where it has been assumed that the droplet is freely rotating and that there is no elastic coupling to the SU8 surface

$$\gamma_1 \frac{d\theta}{dt} = \frac{1}{2}\epsilon_0 \Delta\epsilon \sin 2\theta E^2 \tag{3.3}$$

For the data in Figure 3.7, the electric field was applied at an angle of $\theta = 40°$ to the initial n director orientation. The gap between the in plane electrodes was 120μm and for this electrode geometry the electric field in the centre of the gap is given approximately by $E = \frac{\pi V}{2l}$, where V is the rms magnitude of the applied a.c. voltage. When these parameters, the initial rate of rotation from Equation 3.1 and the dielectric anisotropy of E7 of $\Delta\epsilon = 13.7$ [93] are substituted into equation 3.3 this yields an estimate for the viscosity of $\gamma = 26Nsm^{-2}$.

From equation 3.1 and figure 3.7 an angular rotation speed of $450°$/s is possible at room temperature and with $100\ V_{rms}$ driving voltage. An increase in speed by a factor of 5 could be achieved by reducing the gap between the in plane electrodes from 120μm to the order of the droplet diameter. The effective viscosity calculated previously is some two orders of magnitude higher than the independently measured value of $\gamma = 0.18Nsm^2$. [93]. This indicates that the detailed structure of the droplet and the interaction with the SU8 confining well must be taken into account. A significant reduction in the effective viscosity could be achieved by reducing the azimuthal surface anchoring by, for instance, using an appropriate surface treatment.[94] Working at a higher temperature, as shown in the next section, and using a material having a higher ratio of $\frac{\Delta E}{\gamma_1}$ would lead to

a further increase in rotational speed.

3.4 Temperature Dependence

3.4.1 The Size and Increasing Temperature

The size and shape of the droplet confined in the matrix is highly dependent on the temperature of the device. Figure 3.9 shows a microscope image of the droplet using reflected unpolarised white light and a magnification of $500\times$ for different temperatures 20.7, 25, 30 and 35° C. The droplet has the most circular shape at 30°C and as the temperature falls the droplet increases in size until it begins to interact with the walls of the confining well as can be seen at 20.7 ° where the droplet is no longer circular.

As the temperature of the droplet is increased, the droplet decreases in size as can be seen when the droplet is at 35°C above this temperature the droplet begins to disappear completely although the temperature at which the droplet disappears is different for every droplet and depends on the initial volume of liquid crystal contained in the box. although changes in the surface tension of liquid crystals with temperature have been seen, they mainly occur near the nematic-isotropic transition temperature [95–97]. Indeed measurements of the contact angle of E7 liquid crystal on an SU8 surface between 20° and 63° showed no changes, with the contact angle remaining at 5°.

Figure 3.10 shows the average diameter, for a different confined nematic droplet to the one shown in figure 3.9, as a function of temperature. The diameters where obtained using ImageJ image processing software by measuring the diameter in four directions and taking the average. The size of the droplet is plotted as a percentage of the initial size at 18°C.
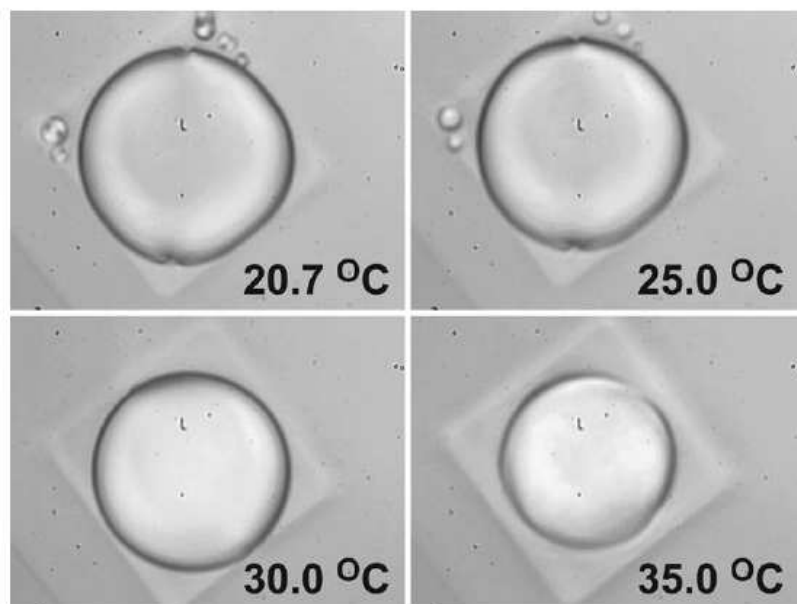
Figure 3.9: Images of a nematic droplet confined in a box matrix at different temperatures
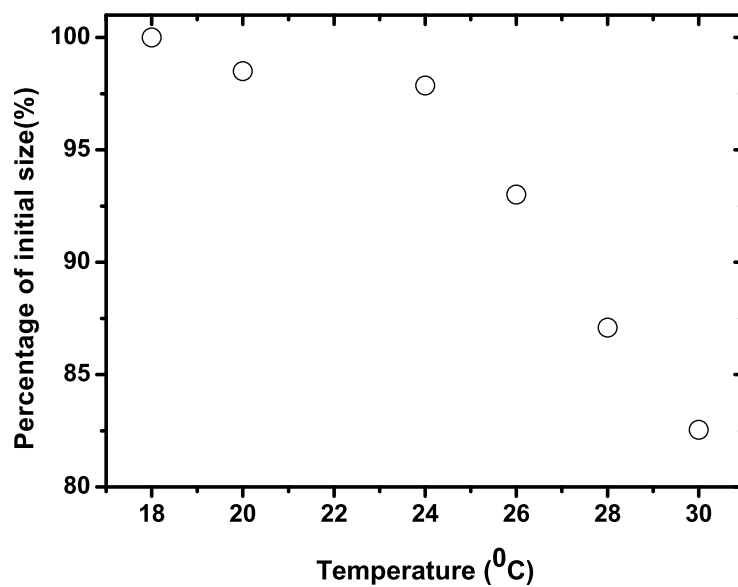
Figure 3.10: Graph showing the Percentage change in the droplets diameter with temperature

3.4.2 Droplet Recovery with Decreasing Temperature

Figure 3.11 shows images of the droplet as the temperature is lowered. In figure 3.11a) the droplet is at 35°C and is reduced in size. As the temperature begins to fall, figure 3.11b small droplets of liquid crystal appear very rapidly across the base of the confining box. These droplets then begin to coalesce and the droplet eventually regains it's original size. This process of recovery to a single droplet can take many hours. The small droplet formation is very similar to that seen in the dewetting of thin liquid films [98–103]. Possible causes for this are nucleation of dry patches in the surface via defects, dust or material heterogeneity or the amplification of thermal instabilities in surface waves at the liquid vapour interface. If this is the case then it indicates that material has been moved from the main bulk of the droplet to a thin layer covering the base of the confining well.

a)   b)   c)
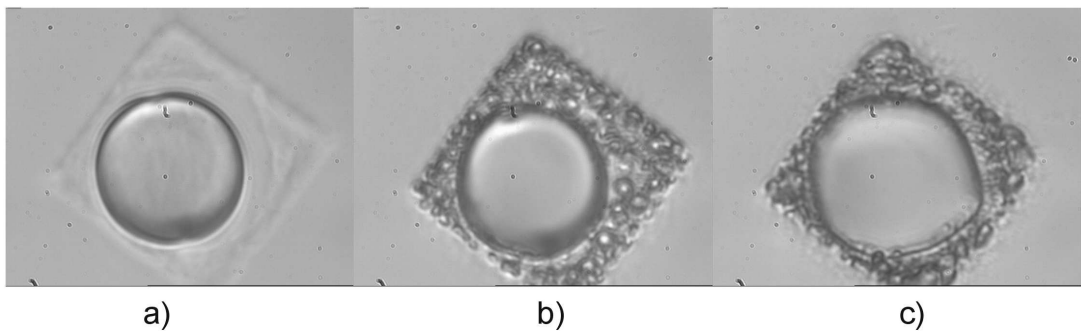
Figure 3.11: Images of a nematic droplet as the temperature falls. The starting temperature is 35°

3.4.3 Optical Texture Dependence on Temperature

As well as the size and shape of the droplet being dependent on the temperature, so too is the optical texture of the droplet. Figure 3.12 shows the droplet viewed through crossed polarisers at 20°, 28 and 30°. The optical texture of the cross shape and thus the bipolar orientation of the director becomes much less prominent at the higher temperatures with the whole droplet appearing black,

indicating that a greater area of the droplet has the director aligned either vertically or horizontally. This could be due to a change in the strength of the surface anchoring at the free surface or at the SU8 surface. It may also be due to changes in the elastic constants of the liquid crystal.
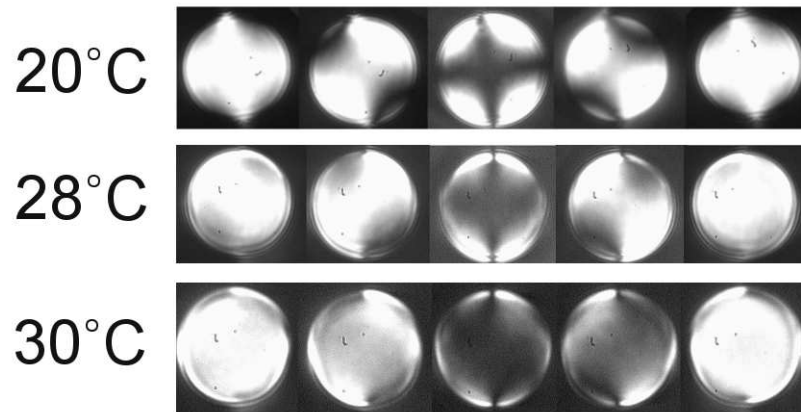
Figure 3.12: Images of a nematic droplet confined in a box matrix at different temperatures taken through crossed polarizers

3.4.4 Switching Dependence on Temperature

The interaction of the outer surface of the droplet with the walls of the box also gives rise to an interaction of the nematic disinclination with the walls of the box. Figures 3.13 and figure 3.14 show the burst duration at different voltages in switching the droplet shown in figure 3.9 from the vertical state to the diagonal state.

The affect of the surface interaction and the wells of the box are clear on figure 3.13 and figure 3.14. The contact formed with the box wall presents the defect with an energy barrier to overcome during the droplets rotation which lead to the breakdown of the relationship seen earlier in Equation 3.1 for smooth switching of the device. At 30.5 ° C (figure 3.9) the droplet follows the linear relationship, but at lower temperature, as the droplet becomes increasingly squared, the burst duration for higher voltages increasingly increasingly deviates from the previous relationship.
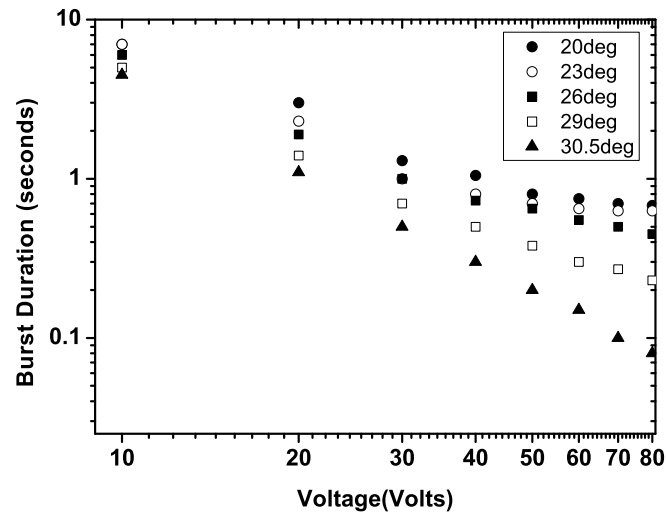
Figure 3.13: Graph showing the pulse duration at 10kHz for switching a pixel from one state to another with increasing temperature
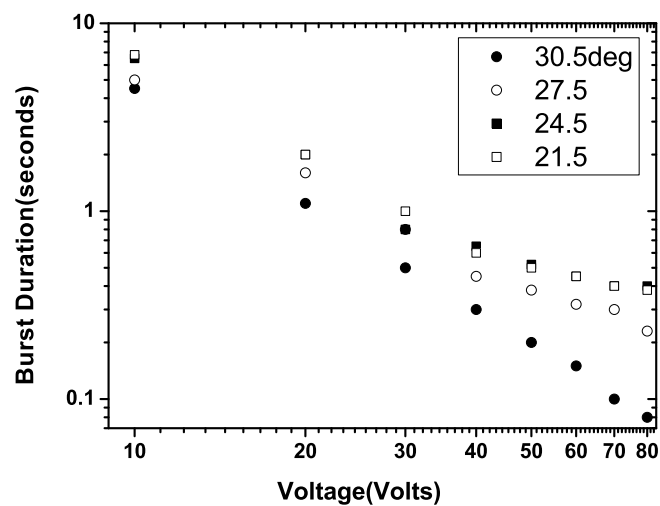
Figure 3.14: Graph showing the pulse duration at 10kHz for switching a pixel from one state to another with decreasing temperature

3.5 Non Circular Droplets

3.5.1 Static States

In some cases the liquid crystal confined by the box formed a rounded square geometry. Although this shape could be changed to circular by increasing the temperature of the device it is interesting to study the switching of device between the various states with different positions of the defects relative to the confining box. In this case the optical axis was similar to previously seen in liquid crystals confined within small wells [89] in which, in a confining well which is completely filled with liquid crystal, the director was again aligned between two nematic disinclinations but these disinclinations tended to preferentially form at the corners of the box.

Figure 3.15 shows a typical droplet in which the volume of liquid crystal is higher relative to the confining box volume. This causes it to form a rounded squared geometry at room temperature. The confining box is $60 \times 60 \times 15$ μm and the electrodes have a width of 120μm with a gap of 120μm. The electrodes can be seen as light areas, top and bottom and the electrodes to the left and right of the droplet are aligned at 40 ° to the other electrodes as in the circular droplet described in section 3.2
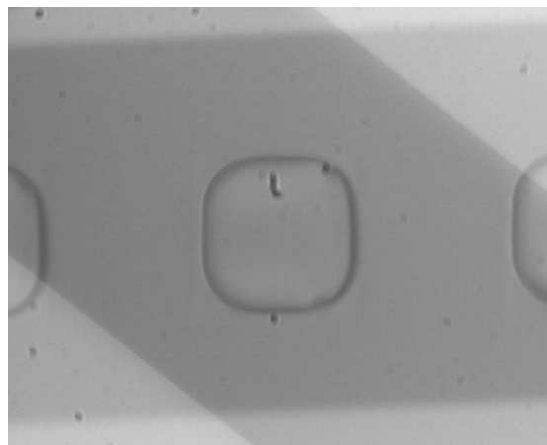
Figure 3.15: Microscope image showing a non circular pixel at 500 × magnification and its position relative the electrodes

Figure 3.16 shows images of a non circular droplet taken through crossed polarizers at angles between -45° and 45°. The different defect configurations are shown in figures 3.16 a) through to c) whilst figure 3.16 d) shows the orientation of the crossed polarisers. In this case there were six possible configurations of the nematic liquid crystal, one being the two fold degenerate state where the defects are at opposite corners of the rounded square as in figures 3.16 a) and b) and the other being the four fold degenerate state in which the defects form at the corners along one side of the square (figure 3.16 b).
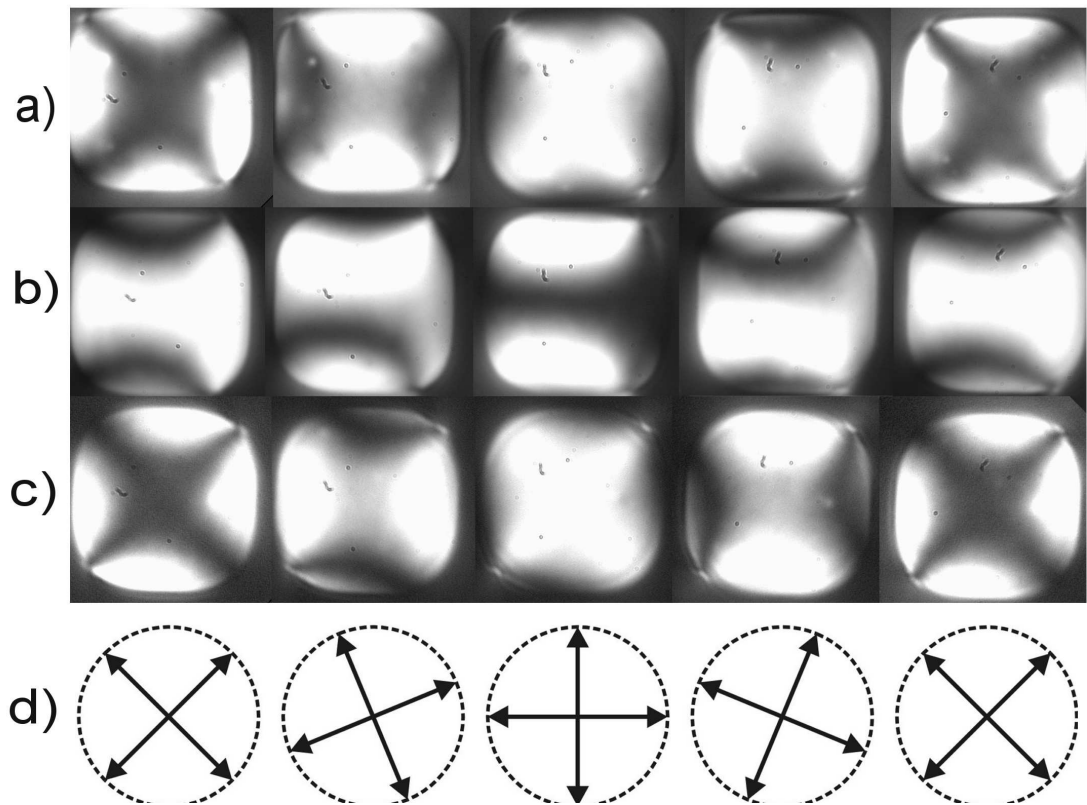
Figure 3.16: Microscope image showing a non circular pixel under cross polarisers at different angles. a) the pixel in state 1 b) the pixel in state 2 c) the pixel in state 3 d) position of the cross polarizers

The textures in the droplet in this shape are very similar to those seen previously in nematic alignments created using confining boxes of 80μm [89] Which are shown in figure 3.17 [89].

As stated previously it was found that by applying a pulsed voltage to either pair of the electrodes it was possible to reconfigure the defects and switch between
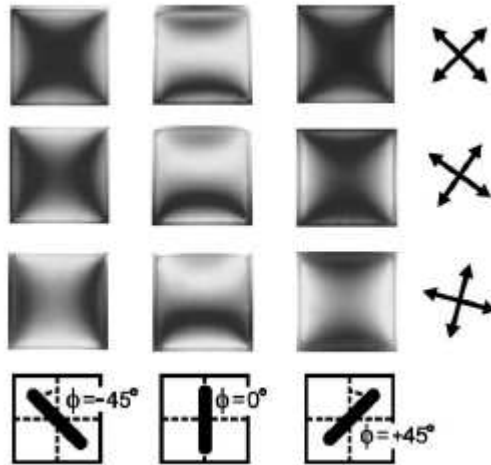
Figure 3.17: Alignment states observed in transmission between crossed polarisers under a magnification of 100×. The polarisers are rotated by 0°(upper row) 10.5° and 21.0°(lower row)relative to the device. The arrows in each case indicate the polarizer orientations. The wall were formed from squares with sides of 80μm.

the configurations shown in figure 3.16.

Figure 3.18 shows Images of the droplet in two states and a schematic of a square droplet with the defects shown as black dots in the corners of the droplet the start and finish position is shown for each switching regime and is duplicated in the schematic with arrows showing the movement of the defects.

The droplet could be switched from a diagonal state to a horizontal states, see figure 3.18a), by the application of a voltage across the horizontal electrodes. In this case the diagonal starting position is the opposite position to that in figure 3.18c) and the switching is achieved by moving the defect along the bottom edge of the droplet to the bottom right hand corner of the droplet.

The pixel could also be switched from a horizontal state to a diagonal state, figure 3.18b) and in this case the defect in the top right hand corner of the droplet was moved to the top left hand corner by the application of a voltage across the horizontal electrodes. This caused the defect to move across the top of the droplet from corner to corner.

The droplet could also be switched from one diagonal state to other by the
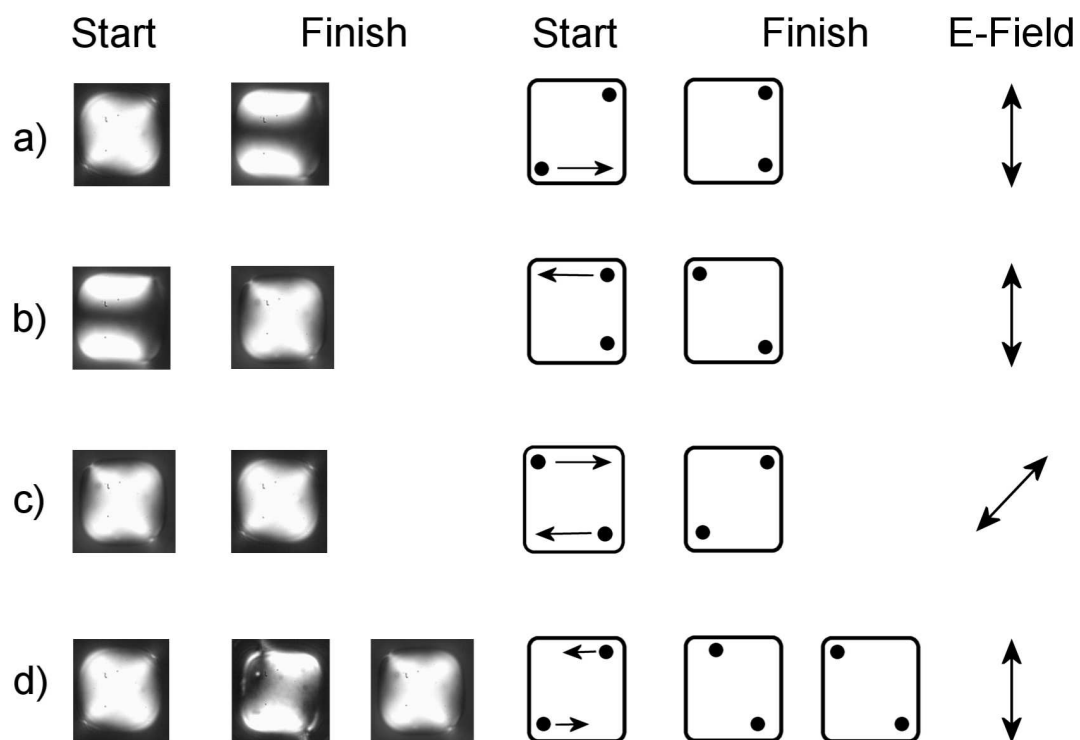
Figure 3.18: Images of the different switching states of a squared circular pixel. Crossed polarizer images start and finish position (left); Cartoon showing defects for each switching regime(center); and the direction of the applied electric field (right).

application of the voltage to the diagonal electrodes. See figure 3.18c). In this case the defects took a route along the top and bottom edges of the droplet.

The droplet could be switched from one diagonal state to the other diagonal state by moving both defects at the same time across the bottom and the top of the droplet to their opposing corners. In this case the voltage was applied to the horizontal electrodes. This method of switching also led to the formation of an intermediate state in which the two defects stopped slightly short of the true corner positions, which could be due to defect pinning at in homogeneities in the wall of the confining box, however the final corner to corner state of the droplet was formed after the voltage was removed and the defects relaxed into the corner positions of the droplet. Figure 3.18d shows these three stages of the switching of the pixel.

The droplet could also be switched from one diagonal state to other by he application of the voltage to the diagonal electrodes. See figure 3.18c. In this case the defects took a route along the top and bottom edges of the droplet.
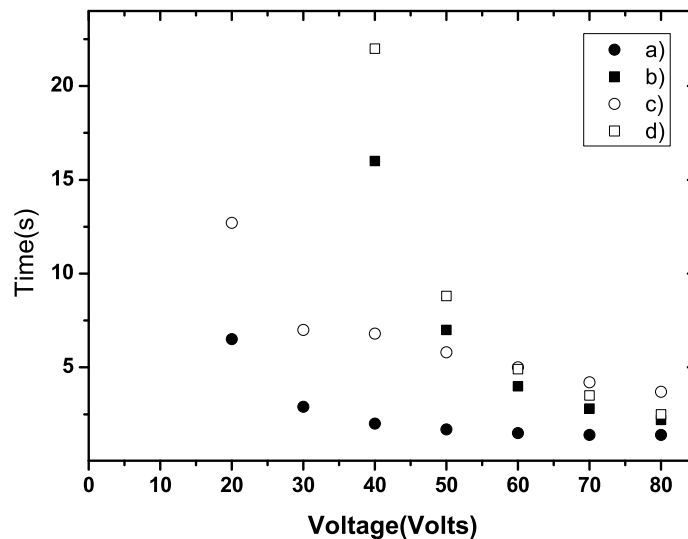
Figure 3.19: Graph showing the switching times, in response to a 10 kHz sinewave, of the different regimes of switching described. The key shows the regimes as described in figure 3.18

Figure 3.19 shows the switching times versus the voltage for the different regimes described in figure 3.18. On inspection of the graph it is clear that switching in both directions is possible from the diagonal to the other diagonal state, i.e. figure 3.19 c) and d), however, these two curves are very different. as would be expected due to the different E-field orientations meaning the rotational force is applied perpendicular to the director orientation in curve c) but not in curve d).

3.6 Conclusion

The azimuthal rotation of the optical axis of a nematic liquid crystal droplet has been demonstrated. It has been shown that the orientation of the optical axis can be switched to any arbitrary rotation angle. The governing relationship of the switching has been shown in equation 3.1. The shape of the droplet has been shown to be highly dependent on the temperature of the droplet with the disc shape droplet becoming smaller at higher temperatures. This size dependence also has an effect on the optical texture of the droplet and affects the switching relationship. As the droplets shape becomes governed, to a greater extent, by the shape of the box, the switching relationship of equation 3.1 no longer applies. The droplet within the cavity also showed other rounded squared geometries at room temperature and these droplets were able to be switched between several stable states in a variety of electric field configurations and defect movements. The study showed that the diagonal states of a rounded square droplet could be switched from one diagonal to to the other when the electric field was applied in two different orientations (figures 3.18 c) and d), however switching the pixel using the horizontal electrodes required much longer burst durations of the voltage. This switching may be explained with reference to figure 3.15 as the electrodes are not aligned perfectly parallel to the flat edges of the droplet. This would lead to a very small torque force on the nematic molecules when the field is applied,

resulting in the rotation of the optical axis. The study of these switching regimes has also given some insight into the movement of a defect on a free surface in the presence of an applied electric field.

Chapter 4

Defect-Defect Interactions in Rotating Nematic Droplets or "Defect Traffic Jams"

4.1 Introduction

In the previous chapter we looked at the pulsed switching of a nematic liquid crystal droplet in electric fields oriented diagonally to each other. In this chapter the action of a rotating electric field on the confined liquid crystal droplet is studied. With the electrodes now oriented orthogonally it is possible to create an in plane rotating electric field. The droplet shows the same director orientation as in the previous chapter and smooth rotation of the nematic defects about the circumference of the droplet has been achieved. The effect of temperature on the smooth rotation is shown to follow the relationship $T \propto \frac{1}{V^2}$ and the rotation is faster at higher temperatures. The interaction of the nematic disinclination at the edge of the droplet with the walls of the confining well are shown to affect the rotation and by adjusting the amplitude of the driving voltage and its frequency of rotation, several non periodic rotation regimes have been studied.

4.2 Device Construction

The device consists of a nematic liquid crystal droplet confined in a square well in the same way as that described in section 3.2. A schematic of the electrode orientation is shown in figure 4.1. The confining well was produced in exactly the same way, with exactly the same dimensions, as the device in chapter 3 and the process is described in section 2.3.2. However, in this device the orientation of the electrodes relative to the droplet had been altered. Figure 4.1 b) shows an image of the droplet taken at 500× magnification. The electrodes, which are now oriented at 90 ° to each other, are seen as lighter bands across the top and bottom and along the left and right hand edges of the figure 4.1b). The confining box is oriented diagonally at 45° to the electrodes. Figures 4.1 a) and c) shows a schematic of the electrodes, their orientation and the position of the droplet relative to each set of electrodes.

a)   b)   c)
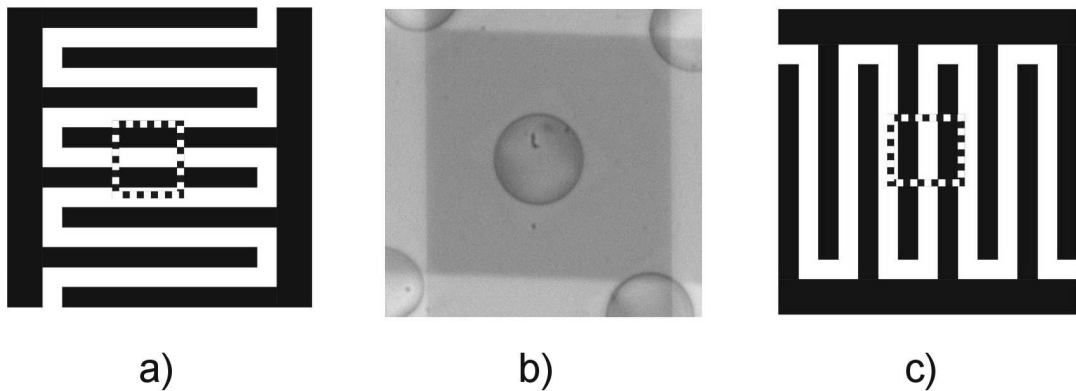
Figure 4.1: a) and c) electrodes in the device with the position of the relevant droplet marked by a dotted line b) image of the droplet taken in transmission at 500× magnification

4.3 Optical Texture

With the electrodes in this orientation it was possible to switch the droplet using either a horizontal or vertical electric field. Figure 4.2 shows the droplet viewed at 500 × magnification through crossed polarisers the droplet is shown switched

into two stable states, one vertical (figure 4.2a) and one horizontal (Figure 4.2b). The positions of the crossed polarisers are shown in figure 4.2 c) .The droplet was switched into the vertical and horizontal state by applying a 5 second burst of a.c. voltage across the horizontal electrodes and the same burst to the vertical electrodes respectively.
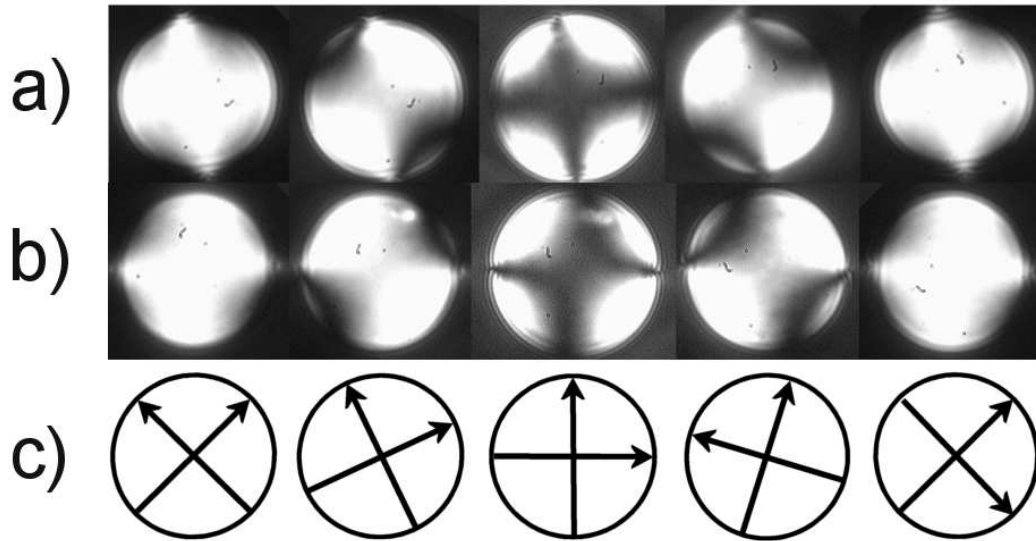
Figure 4.2: The droplet switched into the vertical state a) The horizontal state b) and the positions of the crossed polarizers c)

Applying the same arguments as that given in chapter 3 section 3.3.1. Regarding the crossed pattern seen under crossed polarisers and the tendency of the n-director and the Nematic defects to align with the electric field the director orientation is that of the bipolar pattern in chapter 3.

4.4   Smooth Rotation of the Droplet

With the electrodes oriented at 90° to each other it was now possible to create a rotating electric field using a two channel phase locked waveform generator (section 2.4.2) in the plane of the electrodes and thus rotate the optical axis of the nematic droplet though a full 360°. The rotating electric field was created by addressing the individual electrodes as described in section 2.4.2 and the

experimental setup for viewing and data capture is described in section 2.4
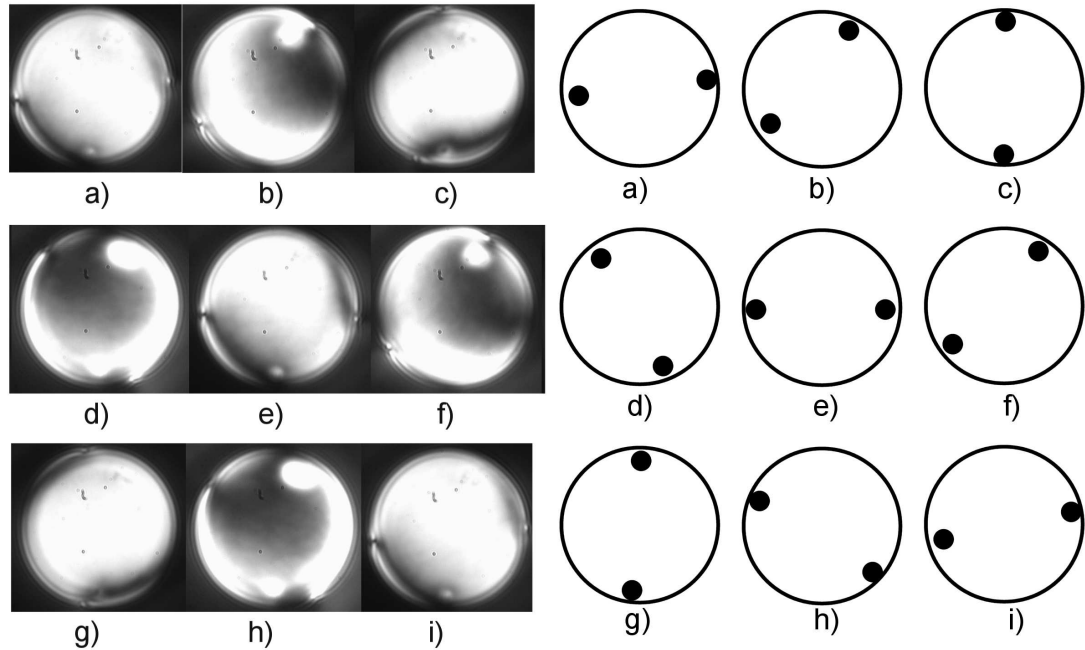
Figure 4.3: Image showing nine frames from one complete rotation of a nematic droplet (left) in a rotating electric field the images are taken at 1 second intervals. the droplet is rotating anticlockwise and corresponding cartoons of the positions of the nematic defects are shown on the right

An example of a smooth rotating droplet is shown figure 4.3. In this example of smooth rotation the peak to peak amplitude of the electric field was 80V and the frequency of rotation of the electric field was 0.1Hz. The actual droplet images are shown on the left and a schematic showing the defect positions is shown on the right. The droplet was imaged at 1 second intervals through one complete rotation. The nematic defects on the edge of the droplet do not traverse the perimeter at a constant rate. In figures 4.3 b),d),f) and h) the defects are not at exact opposite edges of the droplet. Nevertheless, this state of rotation is classed as smooth rotation for the purposes of this study because if left to rotate indefinitely it is uninterrupted and continuous. The non uniform rotation of the defects is caused by the interaction of the defects with the walls of the confining box. In figure 4.4 the droplet is shown in the confining well and the edge of the well has been highlighted with a dotted line. The instances when the defects are

not at directly opposite each other during rotation tend to be when the defect is approaching a region where the edge of the droplet is closest to the confining wall. In these areas of closest approach the walls of the well present an energy barrier to the defect.
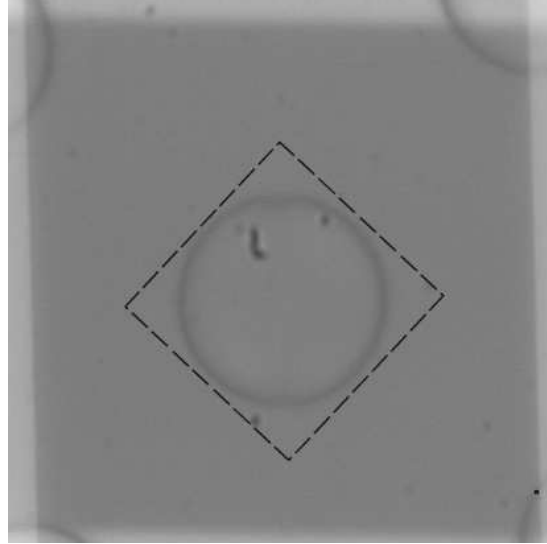
Figure 4.4: Microscope image of the nematic droplet with the confining box marked with a dotted line.

As stated in chapter 3 the shape and size of the droplet was highly dependent on the temperature. The temperature of a droplet, which was circular at all temperatures studied, also affected the relationship of the driving frequency and the voltage. Figure 4.5 shows a plot of voltage required to achieve smooth rotation against the period of rotation at different temperatures on a logarithmic scale. For each temperature, the voltage at a particular frequency of rotation, was adjusted until an uninterrupted smooth rotation was achieved. The linear fit parameters for the lines plotted on figure 4.5 are shown in table 4.1 where the line of best fit is given by the equation $\log_{10}(V) = \log_{10}(\alpha) + \beta \log_{10}(T)$. At 26 and 28° the gradient of the graph is 0.5 to within the error but at lower 20,22 and 24° the gradient is 0.53 which is close to 0.5.

Figure 4.5 follows the relationship of $T \propto \frac{1}{V^2}$ where T is the period of a complete rotation and V is the applied voltage. It also shows that as the temperature of the sample increases the applied voltage needed to achieve the same rotational
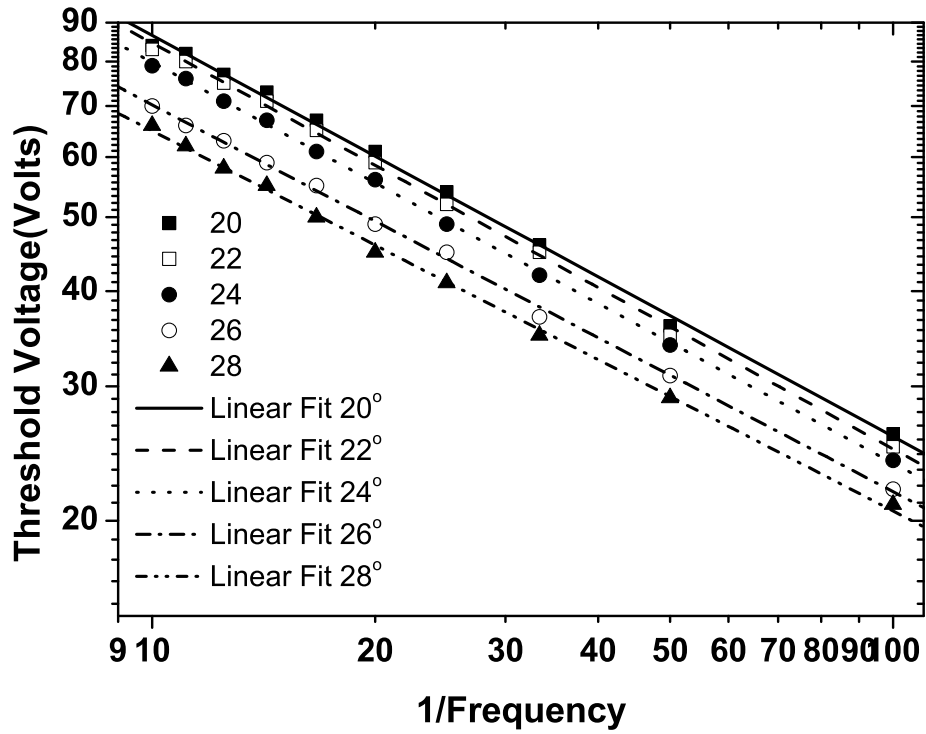
Figure 4.5: Graph showing the threshold voltage for smooth rotation of the liquid crystal droplet at different temperatures.

Table 4.1: Linear fit data for Figures 4.5

Temperature ° C	α	$\delta\alpha$	β	$\delta\beta$
20	2.463	0.011	-0.526	0.008
22	2.459	0.008	-0.532	0.006
24	2.427	0.005	-0.525	0.004
26	2.353	0.009	-0.507	0.007
28	2.311	0.009	-0.498	0.006

period decreases. This may be due to a reduction in viscosity or changes in the elastic constants, the dielectric anisotropy or surface anchoring.

4.5   Non-Smooth Rotation

As stated previously, the nematic disinclinations do not traverse the circumference of the droplet at a uniform speed. As the defects pass the regions of close proximity to the well wall there is an interaction which presents an energy barrier to the defect and causes it to slow down. These interactions hinder smooth rotations and if the droplet was driven at frequency faster than that required for smooth rotation at a particular voltage, or if it was driven with a lower voltage than that required for smooth rotation at a particular frequency the droplet no longer rotated smoothly.

These interactions with the well wall and the interaction between defects led to the formation of several interaction regimes which are discussed here. to simplify the discussion the regimes will be referred to by the names: "T-formation", "double defect" and "defect sticking".

The experiment was performed using a droplet which was circular at 18° C, the electrodes were the same as in the previous experiment and the confining well had the same dimensions as previously. The frequency of rotation of the driving voltage used was between 0.01Hz and 0.1Hz and at each frequency interval the voltage was set to such a value that smooth rotation was occurring in the droplet. The voltage was then adjusted in small increments until the droplet no longer freely rotated and the rotation led to one of the following regimes

4.5.1   T-Formation

The first regime found is shown in figure 4.6a) to h). This formation occurred when a smoothly rotating droplet had the voltage lowered at a particular frequency. The images are taken at 3 second intervals for a droplet with a driving

voltage 69V and a rotation frequency of 0.07Hz.
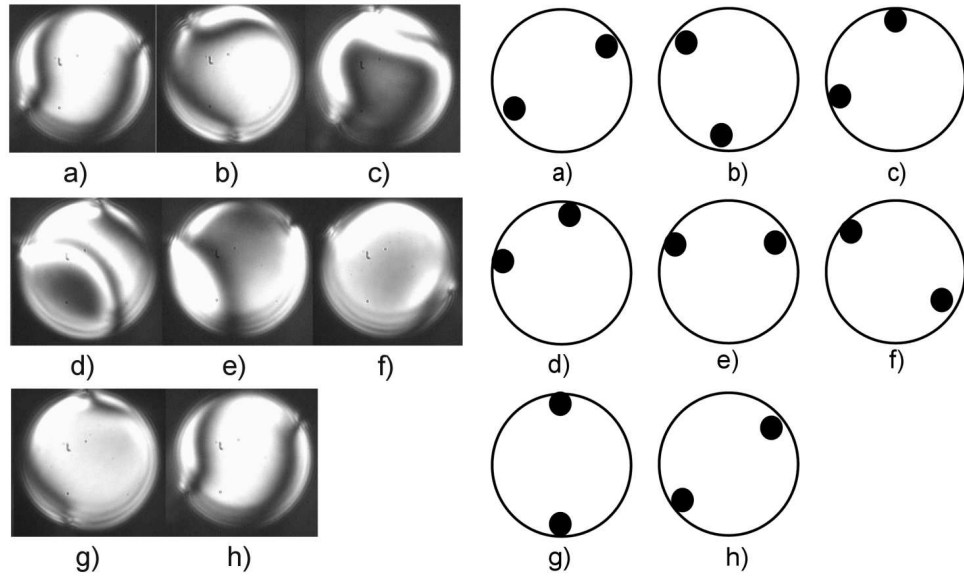
Figure 4.6: Droplet viewed through crossed polarizers showing one complete revolution with T formation for a droplet at 0.7Hz and 69V the pictures are taken at 3 second intervals

In this regime the defects are initially travelling in a clockwise direction. The first defect on the left hand side of figure 4.6a rotates to the upper left quadrant and begins to stick and slow down (figure 4.6 b). The second defect now begins to catch up with the first and leads to the T-formation. This name arises simply because of the pattern of the optical texture observed (figure 4.6 d). At this point the first defect is pushed past the sticking point moves quickly down the right hand side of the droplet whilst the second defect remains almost stationary in the top left quadrant (figure 4.6e through to f. The second defect now moves to the top of the droplet (figure 4.6 g). The second defect does not stick at the top of the droplet, which would produce a second T-formation, instead it moves continuously around to the beginning of the cycle (figure 4.6 h).

Figure 4.7 shows the voltage at which the T-formation begins at different frequencies in a nematic droplet when the voltage is decreased slowly from a smooth rotation voltage.
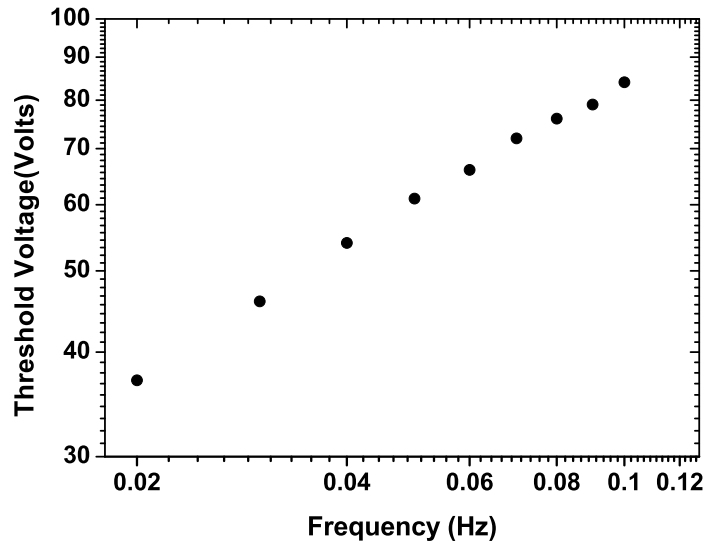
Figure 4.7: Graph showing the threshold voltage at which the T-formation regime of a rotating LC droplet beginsand is plotted on a log-log scale

4.5.2 Double Defect

In the Double-Defect regime the previously shown smooth rotation voltage was applied at a particular frequency. When smooth rotation was established the frequency of rotation of the electric field was increased until the droplet was no longer smoothly rotating. This Regime lead to the formation of what could be a third defect which quickly coalesces with one of the other defects. Figure 4.8 shows images of a droplet in this regime.

The droplet in the images is being driven by an electric field with a rotation frequency of 0.117Hz and amplitude of 90V and the rotation is clockwise. The time interval for each image is not the same because the double defect coalescence occurs very quickly whilst the rest of the cycle occurs more slowly. The time of each image is shown underneath and the eight images show one half of a complete rotation.

At 0 seconds the defects are in the top right and bottom left quadrant of the droplet. At 1 second the defect in the top right of the droplet has moved down and what could be a third defect is seen just below it. Between 1.00 and
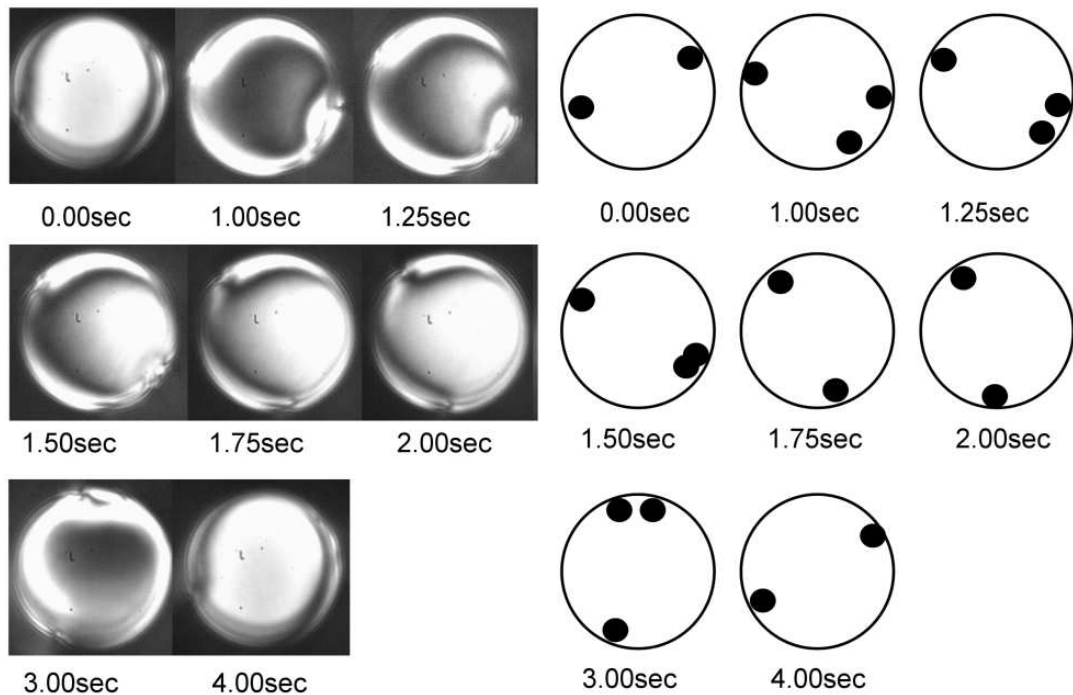
Figure 4.8: Images of a droplet being driven with a rotating electric field of 90V and a rotation frequency of 0.117Hz. The time in seconds is noted below each picture. The eight images show one half of one complete rotation and the rotation is in the clockwise direction.

1.75 seconds these two defects coalesce and the remaining defect carries on in a clockwise motion. Between 2.00 and 4.00 seconds the top defect in the droplet undergoes the same formation of two defects which coalesce, and this repeats for the next half of one rotation.

Figure 4.9 shows the applied field voltage versus frequency for the onset of the double defect rotation regime described previously.

4.5.3 Defect Sticking

If the amplitude of the driving voltage is sufficiently low, the interaction of the defects with the well walls became much more significant. Eventually, the defects become stuck at certain points on the edge of the droplet. In order to investigate this, the droplet was rotated into the position in figure 4.10 a) by the application of a smooth rotation voltage, which was removed at the correct moment. The voltage at a particular frequency was then slowly raised from zero until the defects
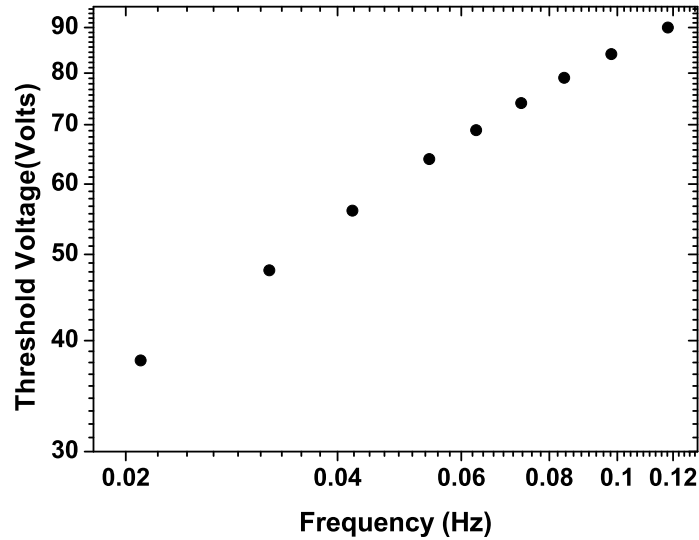
Figure 4.9: Voltage versus frequency of the threshold of the onset of the double defect rotation regime of a nematic droplet.

eventually freed themselves.

Figure 4.10 shows the droplet when the defects have become stuck. In figure 4.10a) one defect is stuck on the right hand side of the droplet and the other in the bottom left quadrant. As the direction of the rotating electric field passes the horizontal the defects can be seen to wobble and try to free themselves. The defect in the bottom left quadrant has a much greater range of motion to the defect on the right. This defect oscillates between the positions in figure 4.10a) and figure 4.10 c). It is not until there is sufficient amplitude in the applied field that this defect reaches the position in figure 4.10 c) and with a sufficiently large electric field the defects are able to free themselves.

Figure 4.11 shows the threshold voltage required for different frequencies to allow the defects to break free of the sticking points.
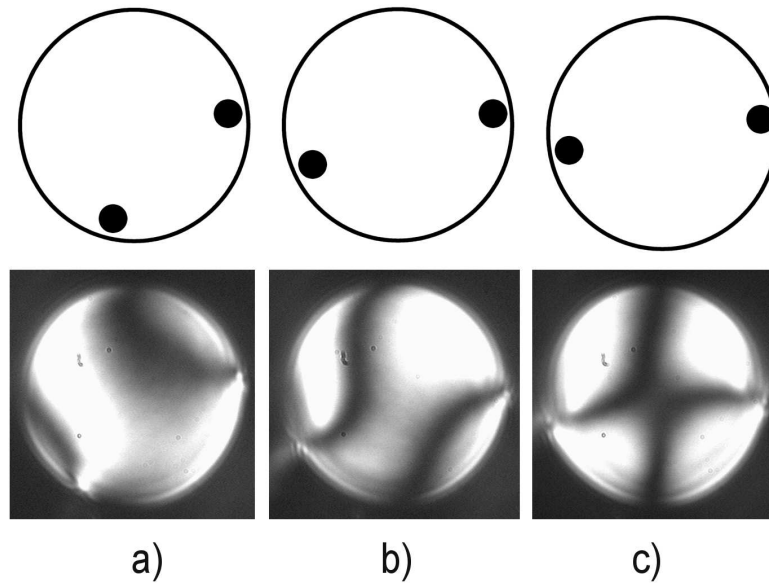
Figure 4.10: Images showing the sticking points of the defects on the edge of a droplet.
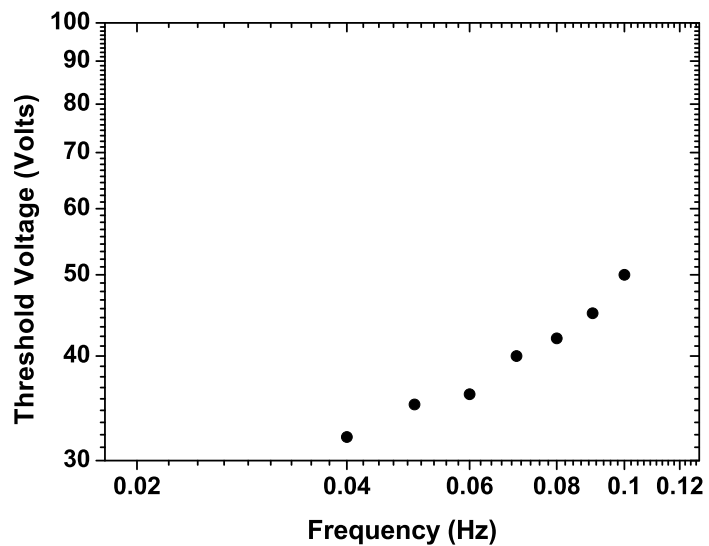
Figure 4.11: Graph showing the voltage versus frequency for the defects in a droplet to free themselves from the sticking pionts

4.6 Conclusions

A nematic droplet has been shown to rotate in a rotating electric field and the relationship between the frequency of rotation and the amplitude of the rotating field have been shown to follow the same V^2 relationship as previously discussed in chapter 3. The nematic defects at the edge of the droplet have been shown to interact with the confining walls of the confining well. This has lead to some interesting interaction between the two defects on the edge of the droplet and also to interesting rotation regimes. Four regimes have been shown and Figure 4.12 shows frequencies and voltages of these regimes.
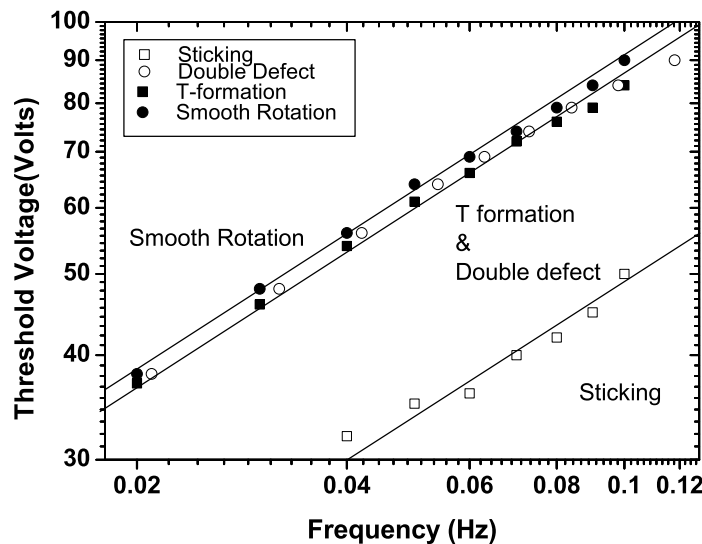
Figure 4.12: Graph showing the voltage versus frequency relationship for the different regimes studied plotted on a log log scale.

In figure 4.12, the smooth rotation of the droplet follow the relationship $T = \frac{1}{V^2}$ and if the droplet is driven with a higher voltage then smooth rotation always occurs. If the voltage is lowered from that giving smooth rotation, the droplet falls into the T-formation regime and the defects begin to catch up with each other and interact. If on the other hand the frequency is increased from smooth rotation the nematic director can no longer keep up with the rotating electric field

and more defects begin to form and coalesce. Eventually, at very low voltages the interaction of the defects with the confining well becomes increasingly significant and they begin to stick at certain points on the droplets perimeter.

Modeling the liquid crystal droplets may be possible with models which allow for changes in the order parameter [104] allowing the description of defects where the liquid crystal melts and reduces the order parameter. The model could possibly be created with a variable surface energy around the circumference of the droplet which may simulate the interactions of the defects with the well walls.

Chapter 5

Sinusoidal Undulations in the Surface of an Oil Film

5.1   Introduction

The subject of this chapter is the undulation in the surface of a thin film of liquid oil created by (DEP) forces resulting from a non-uniform electric field (section 1.3) which creates an amplitude programmable phase diffraction grating. Under the application of a non-uniform electric field a small droplet of hexadecane or 1-decanol oil placed on a surface, containing underlying interdigitated electrodes, spreads into a thin film. The film is shown to be uniform, with a thickness which is virtually independent of voltage. With the application of voltages, higher than that required to create the film, a wrinkle is induced in the oil/air interface. A static analysis of the amplitude of the undulation shows that the amplitude is dependent on the ratio of the electrode pitch and the oil thickness. It is also dependent on the dielectric constant of the oil used to create the layer. A model of this mechanism is created by taking into account the dielectrophoretic forces in the region of the undulation and the energy increase in the oil air interface. The device is then shown to operate, in both transmission and in reflection, as a voltage programmable phase grating where it is able to modulate the intensity of

an incoming laser. Finally, a preliminary study of the switching capability of the device produces switching times in excess of 40μs for modulating the intensity of the first diffracted order from its minimum value to its maximum value.

5.2 Device Construction

A schematic of the device is shown in figure 5.1a) it consists of a set of interdigitated electrodes which are etched into a 50nm thick layer of ITO (transparent conductor) pre-coated onto a borosilicate glass substrate (Section 2.1). The electrodes are arranged in the interdigitated pattern shown in Figure 5.1b). They lie in the xy-plane such that they can be addressed as in figure 5.1b) with one set of electrodes at $\pm V_0.rms$ whilst the other alternate electrodes are at $0V$. The electrodes are then coated with a thin solid dielectric layer of SU8-10 photoresist (Section 2.3.3). This layer acts to stabilize the device against current flow through the oil and also aids in the spreading of the oil under voltage by reducing the initial contact angle with the surface. Finally a thin layer of oil is spread onto the top surface of the dielectric.
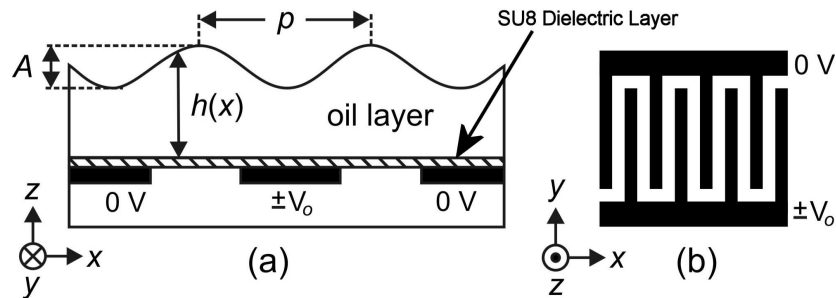
Figure 5.1: Schematic of the structure of the device a) side view b) interdigitated electrode geometry plan view

5.3 Device Operation

The layer of hexadecane or 1-decanol on the surface of the device was created by dispensing small volumes of oil in the region of the electrodes and then applying

a spreading voltage to pull the oil into a thin layer. The volume of oil dispensed was controlled using a Gilsen 0.1-2μl pipette and thus allowed some degree of control of the thickness of the oil film.

When a voltage is applied to the interdigitated pattern of electrodes it creates a highly non-uniform electric field which is periodic and has the same period as the electrodes An indication of the field created in this device is shown in figure 5.2. In this non-uniform field a dielectric material experiences a dielectrophoretic (DEP) force in the direction of the increase in magnitude of the electric field gradient. The force is given by equation1.20 derived in section 1.3.2
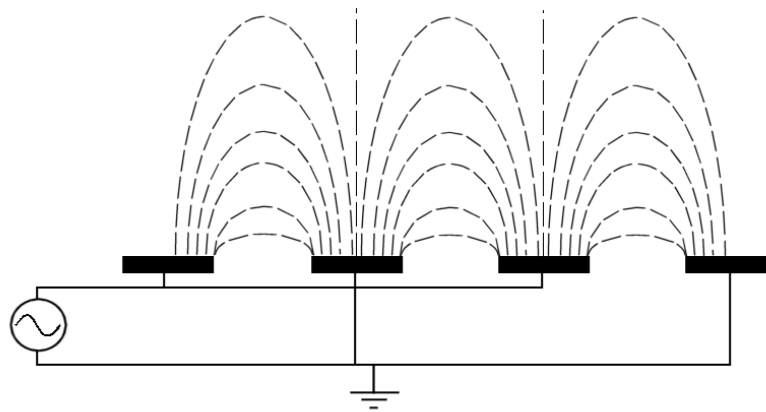
Figure 5.2: Schematic of the non uniform field profile created by the electrode arrangement in the device

On initial contact with the surface the oil remains in a spherical cap with a very low contact angle (Section 1.4.1). Figure 5.3a shows this situation in top and side view. Measurement of the contact angle of hexadecane with an SU8 surface, using drop shape analysis software, showed this angle to be $5° \pm 1°$. With the application of an electric field the oil spreads along and across the fingers of the electrodes into a flat uniform layer above the electrodes [63] as shown in figure 5.3 b). The voltage required to spread the oil into a thin layer was initially 200V, however once a thin uniform layer was created it could be maintained in position above the electrodes with a voltage as small as 20V. On the removal of the electric field the oil begins to recover its original spherical cap shape by

means of a restorative force generated by the surface tension of the oil. However the recovery of the layer into a spherical cap shows hysterisis and is much slower than when drawn out into a film.
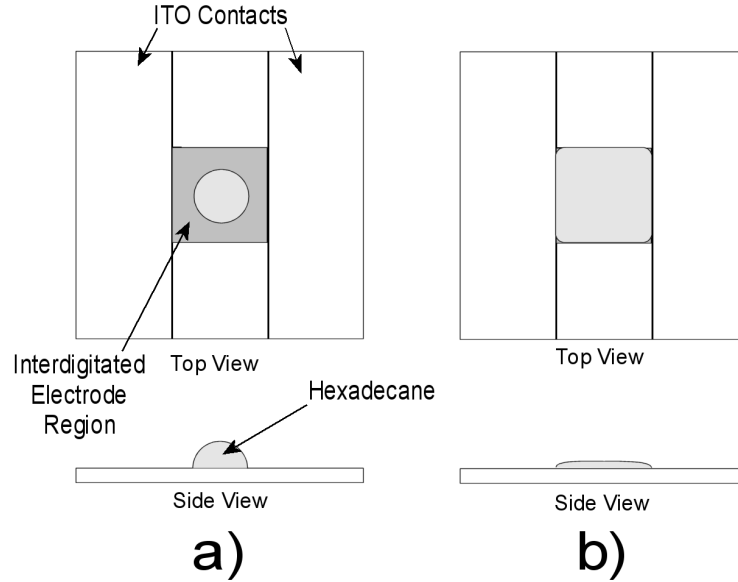
Figure 5.3: Schematic of the way oil contacts the surface of SU8. a) a side and top view before the application of any electric field b) after the application of an electric field, but before surface undulations appear

With the application of voltages greater than that used in the initial spreading of the oil the DEP force creates wrinkles in the surface of the spread oil film. This wrinkle is static, reproducible and stable [105–107]. The period of the wrinkle is equal to the electrode pitch and the peaks and troughs are parallel to the electrodes along the y-direction. This periodic undulation is the result of the force on the oil towards the regions of highest field gradient [64], which in this case occur at the electrode edges [1, 2, 108] and cause the oil to collect there preferentially. The relationship between the amplitude of these wrinkles to the applied voltage and the thickness the layer was the subject of the first study.

In order to study the amplitude, voltage and thickness relationship the complete device was imaged in transmission an interferometer [53] using a He-Ne laser of wavelength 632.8 nm. The interferometer allows the spatial variation of an optical path length, resulting from a variation in thickness of the hexadecane/1-

decanol film to be directly imaged in transmission. With a knowledge of the refractive index of the oil used the peak to peak amplitude of the undulation can be calculated (See section 2.5.2). The two arms of the interferometer had been turned into a vertical position to allow the sample to be placed horizontally to avoid any gravitational effects on the layer (Section 2.5).

An example of the fringes produced is given in figure 5.4 where the Amplitude of the wrinkle (filled circles) created in a 12μm thick layer of oil is plotted against the r.m.s amplitude of the applied voltage squared. The solid line shows the linear regression fit to the data: $A = (5.107 \times 10^{-5})V^2 + 0.118$, in micrometers. The inset photographs show the interferograms for the undulation at 80V (Top left) and 160V (Bottom right).
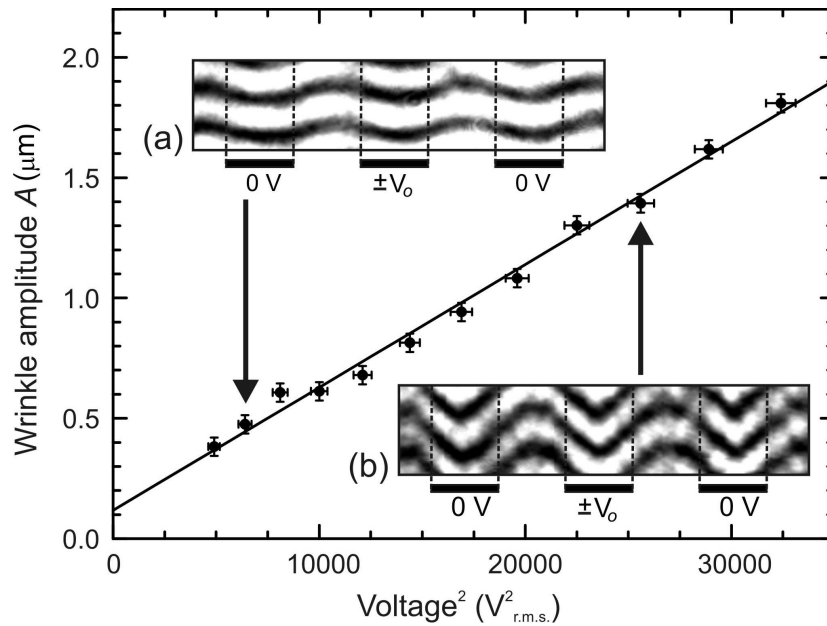
Figure 5.4: Graph showing the amplitude of the undulation in the surface plotted against the voltage squared. Inset are the slices of the interferograms at 80V (top left inset) and 160V(bottom right inset).

Under an applied periodic potential the appearance of the undulation in the oil-air interface reduces the dielectric energy of the system. The surface tension (Section 1.4) acts as a restorative force and resists the deformation of the film. The observed dependence of the amplitude if the undulation on the square of the voltage is calculated in section 5.6.

5.4 Characterizing the Oil Layer

5.4.1 Measuring the Oil Thickness

The thickness of the particular oil used in the experiments was obtained by analysis of interferograms taken in a position at the edge of the electrodes. Figure 5.5 shows an example of an inteferogram from which the thickness can be measured. In figure 5.5 hexadecane is under an applied voltage of 300V. At the bottom of figure 5.5 there is a region which does not contain any oil and is just below the last electrode in the pattern. Just above this is a region the oil is rapidly increasing in thickness and the interference fringes are seen to bend sharply towards the left of the picture. Above this area of rapid change is an area where the thickness of the oil remains constant and a slight undulation is seen in the surface. By measuring the relative number of fringes shifted, by a particular fringe in traversing from a region of zero oil to a region of constant thickness, the thickness of the oil can be determined using the method in section 2.5.4 and equation 2.5.
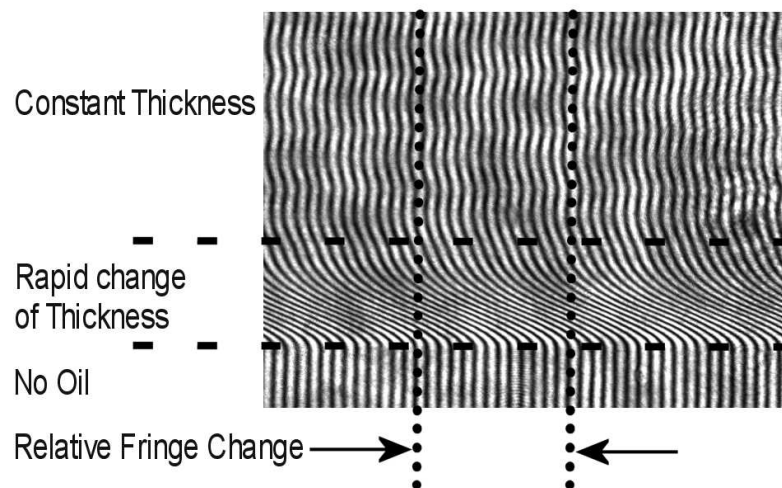
Figure 5.5: Inteferogram showing the characteristic edge profile of hexadecane under voltage over 40μm electrodes. The bottom edge of the electrodes can be seen with no oil on this part of the surface

5.4.2 Surface Undulation and Electrodes

Figure 5.5 also provided valuable information about the profile of the layer surface relative to the underlying electrodes. The surface distortion and the underlying electrode placement that causes it was obtained by taking an image of the electrodes in a particular region of the sample, using white light in transmission, whilst the sample was in situ in the interferometer. The electrodes, being only 80% transmissive, appear as dark regions on the image and the gaps appear as light regions. Exactly the same region on the sample is then imaged in transmission with the He-Ne laser and the resulting interferogram is overlaid with the white light picture to find the phase of the surface undulations with reference to the electrode pattern.

Figure 5.6 shows an image of a set of 320μm pitch electrodes. The image is taken in transmission so the marked electrodes appear as the dark region in the image. Figure 5.6a) and c) are extracts of an image taken in exactly the same position on the sample using the interferometer and overlaid in the correct position. When the fringe change is compared with the underlying electrodes the fringes can be seen to move rightward on top of the electrodes and leftward in the regions between. By comparison with figure 5.5 a rightward change can be associated with the oil becoming thinner and a leftward change can be associated with the oil becoming thicker. Using this technique it is clear that the peak in the undulation is above the gap between the electrodes and the trough is above the electrodes. The period of the undulation is determined by the period of the electrodes.

In figure 5.6 the undulation above the electrodes appears to have a flat top, giving the undulation a non sinusoidal shape. This shape variation will be discussed later in chapter 6.
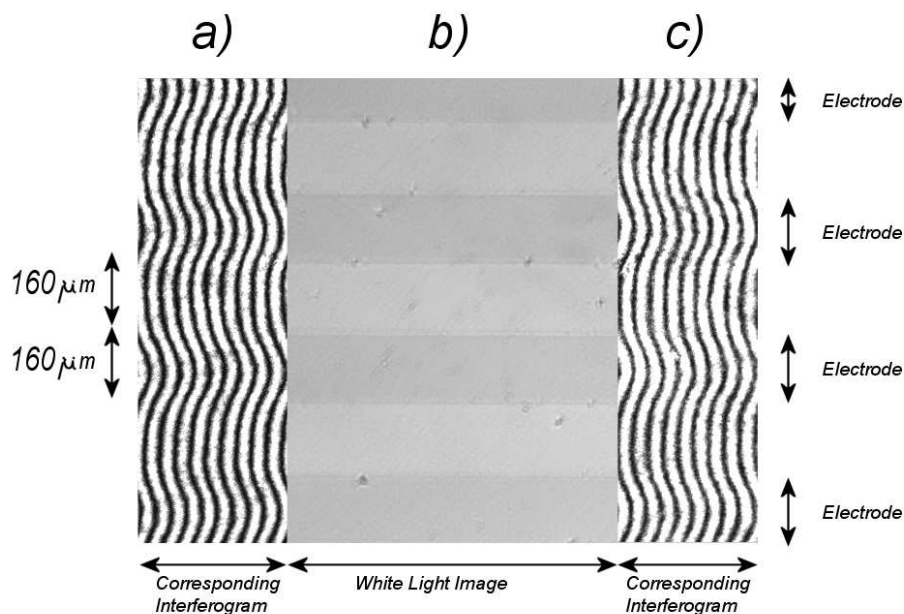
Figure 5.6: An overlay of an interferogram and an optical image of the same region of electrodes, taken in transmission. The electrodes can be seen as dark regions in b and have been marked on the right hand side of the image. The interference fringe pattern for an undulating layer of Hexadecane is seen in a and c.

5.4.3 Uniformity of the Layer Thickness

With both hexadecane and 1-decanol the thickness changes very rapidly at the edge of the electrodes, reaching its maximum thickness over the first few electrodes and then becomes constant over the rest of the surface. This can be seen in figure 5.5 because the fringe pattern above the rapidly changing region becomes a uniform undulation parallel to the electrodes. The thickness of the oil layer was found to be almost independent of the applied voltage (figure 5.7). The graph shows the edge profile of a hexadecane layer of average height 8.45μm above electrodes with a 320μm pitch. The average thicknesses over half a wavelength of the surface undulation (Figure 5.8) are given in table 5.1. The average thickness is marked on the graph and can be seen to vary very little as the voltage increases. The first two electrodes in the array are marked with bold lines, and this rapid change becomes much steeper as the voltage is increased, however the overall thickness of the layer remains almost constant.
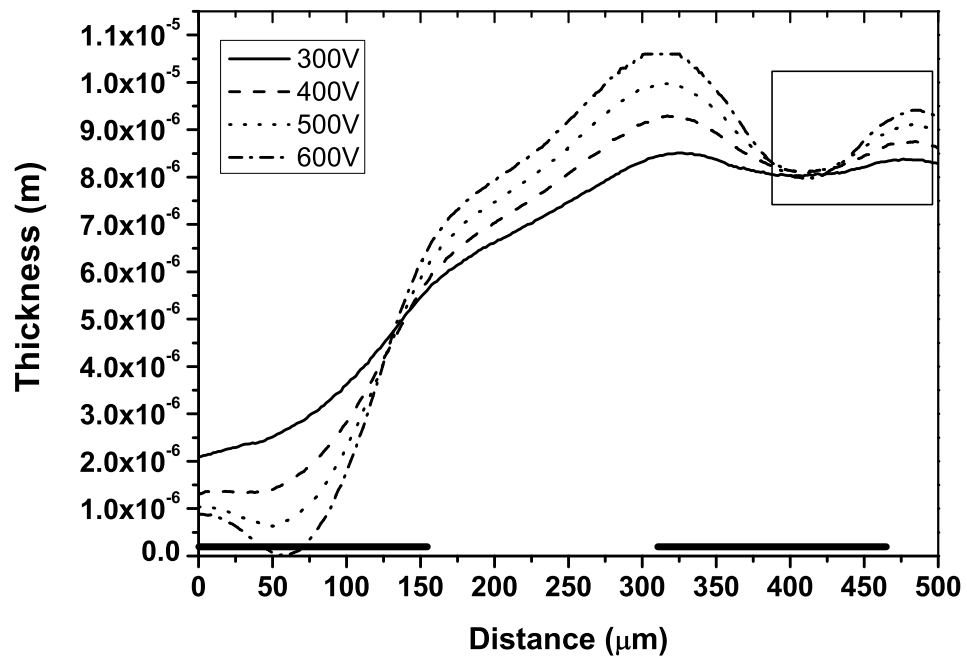
Figure 5.7: Graph showing the edge profile of a 8.5μm thick layer of oil, at 300V, 400V, 500V and 600V, the electrodes have a 320μm pitch and are shown as thick black lines.
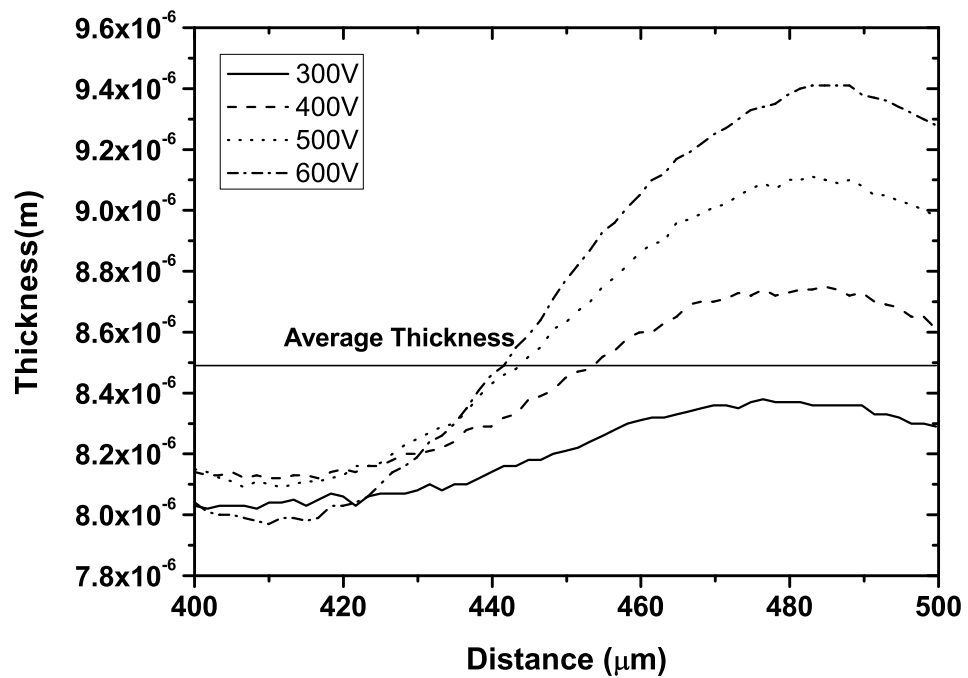
Figure 5.8: Close up of marked region in figure 5.7 With the average height of 8.45μm marked on the graph

Table 5.1: Average height of the $\frac{\lambda}{2}$ region shown in figure 5.8

Voltage	Min Height$\times 10^{-6}$(m)	Max Height$\times 10^{-6}$(m)	Average$\times 10^{-6}$(m)
300V	7.79	9.40	8.59
400V	8.10	9.10	8.60
500V	8.12	8.73	8.30
600V	8.02	8.36	8.19

5.4.4 The Uniformity of the Undulation Amplitude

The shape of the undulation was seen to vary depending on the position along the length of the electrode. Figure 5.9 shows the wrinkle created by placing 0.25μl of hexadecane on electrodes with a 160μm pitch, with an applied voltage of $600V_{rms}$

The images show the shape of the undulation in six different positions above the electrode region. The positions of the images are shown schematically in figure 5.9 a) as the regions bounded by dotted lines. The maximum amplitude of the undulation above the electrodes can be seen to vary along the length of the electrode. This effect is shown schematically in figure 5.10 The depth of the trough above the electrodes and at the tip of the electrode is smaller than the depth of the trough at the base of the next consecutive electrode, whilst in the centre of the electrodes the depth of the trough is equal on consecutive electrodes. This variation is most likely due to resistive loss in the electrodes.
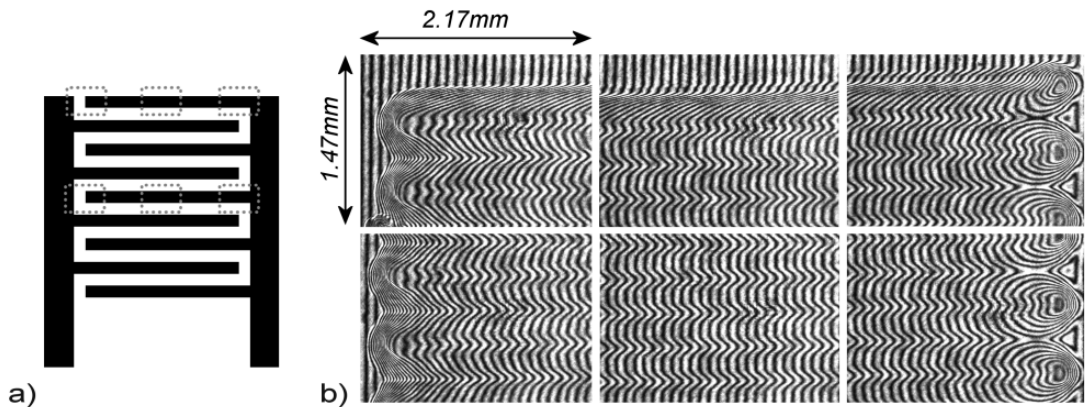
Figure 5.9: Interferogram showing how the amplitude of the ripple shows a double periodicity depending on its position on the electrodes.
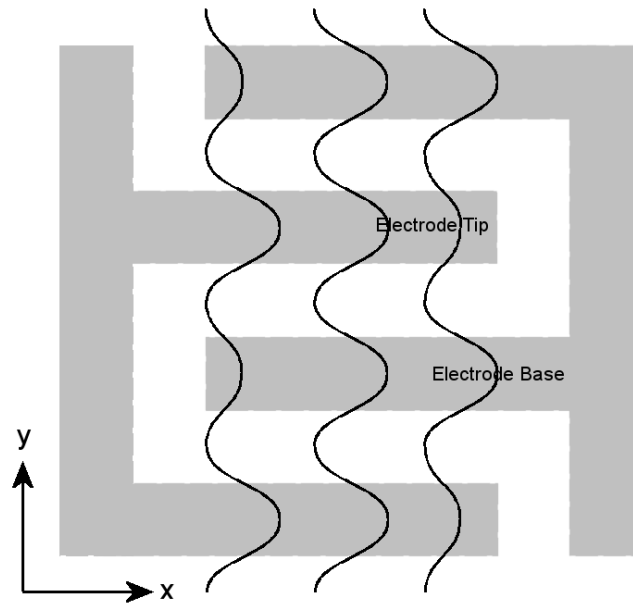
Figure 5.10: Schematic of the shape variation of the undulation probably due to resistive loss in the electrodes.

5.5 Static Amplitude Measurements

Figures 5.11 through to figure 5.18 show the amplitude of the undulation created at the surface of the hexadecane and 1-decanol film as a function of voltage squared. Hexadecane has a dielectric constant of 2.05 whilst 1-decanol has a dielectric constant of 8.10 [109]. The Samples tested were 320μm, 240μm, 160μm and 80μm pitches, in each case the electrode width is the same as the electrode spacing so in the case of a 240μm pitch the electrodes are 120μm and the gaps between electrodes are 120μm. Each graph shows this relationship with different oil layer thicknesses and the linear fit for each data set. The linear fit results are shown in table 5.2 where the equation of best fit is given by:

$$A = \alpha + \beta V^2 \tag{5.1}$$

where A is the peak to peak amplitude of the undulation.

The variation of the thickness of the oil was achieved by controlling the volume of hexadecane or 1-decanol initially deposited onto the surface before the

spreading voltage was applied as outlined in section 5.4.

Figures 5.11 through to figure 5.18 along with table 5.2 show that a higher amplitude can be achieved for a given voltage if:

- A larger pitch of electrode is used for a given layer thickness.

- A smaller layer thickness is used for a given pitch of electrodes.

- An oil with a larger dielectric constant is used.
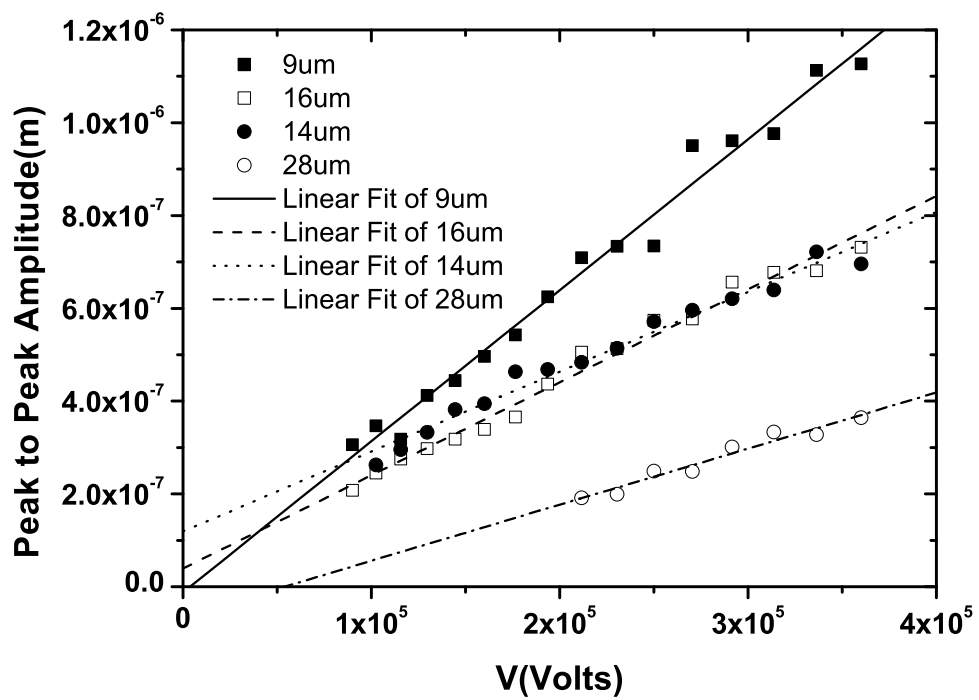
Figure 5.11: Graph showing peak to peak amplitude of the surface undulation as a function of applied voltage squared and hexadecane thickness for 80μm pitch electrodes
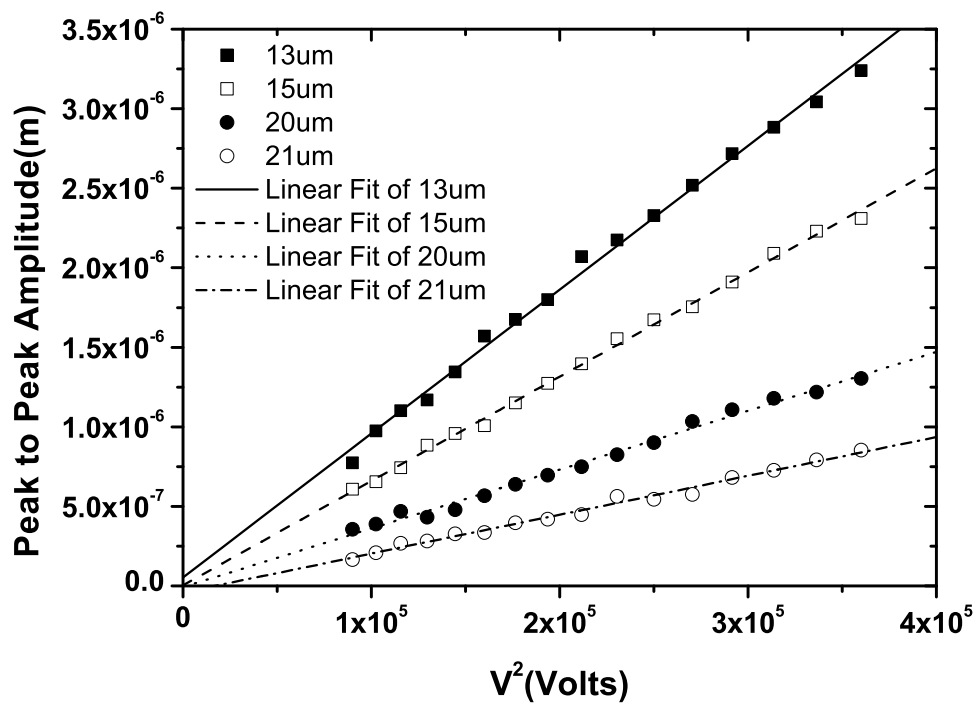
Figure 5.12: Graph showing peak to peak amplitude of the surface undulation as a function of applied voltage squared and hexadecane thickness for 160μm pitch electrodes
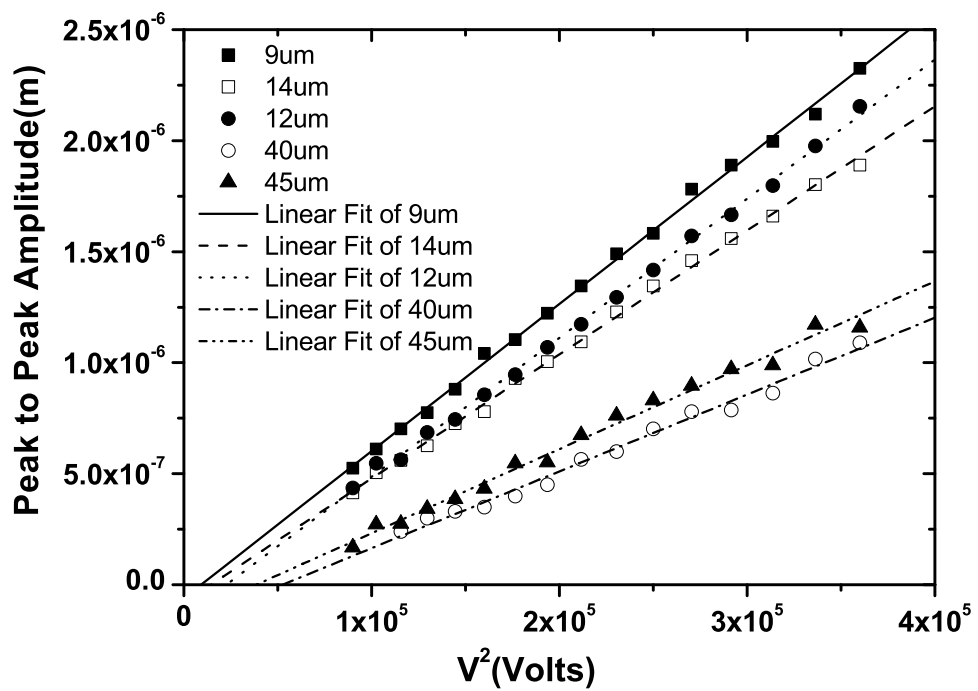
Figure 5.13: Graph showing peak to peak amplitude of the surface undulation as a function of applied voltage squared and hexadecane thickness for 240μm pitch electrodes
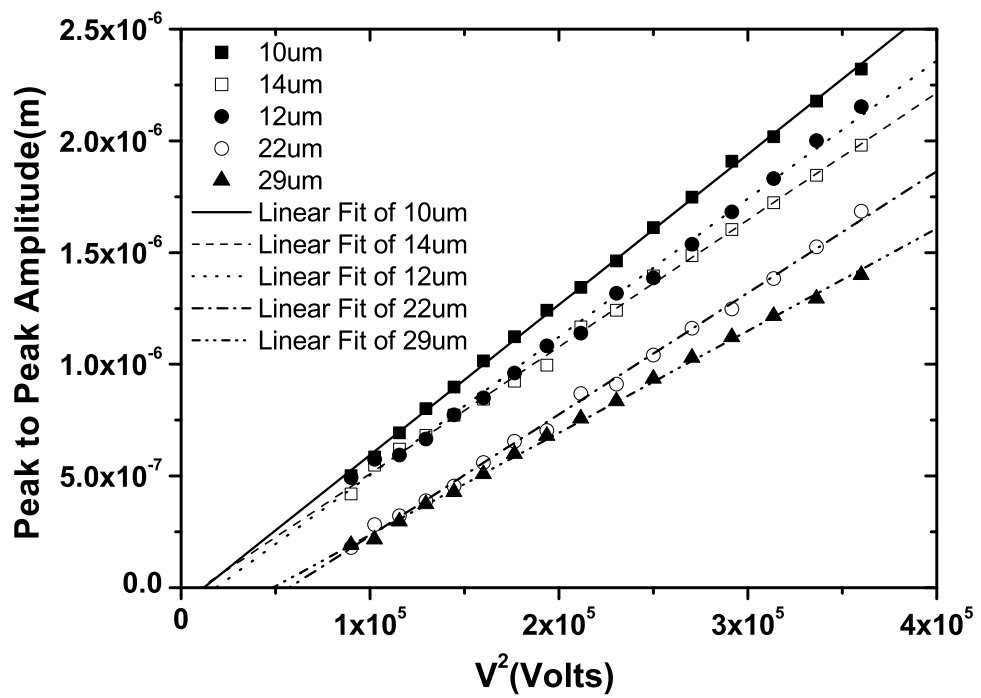
Figure 5.14: Graph showing peak to peak amplitude of the surface undulation as a function of applied voltage squared and hexadecane thickness for 320μm pitch electrodes
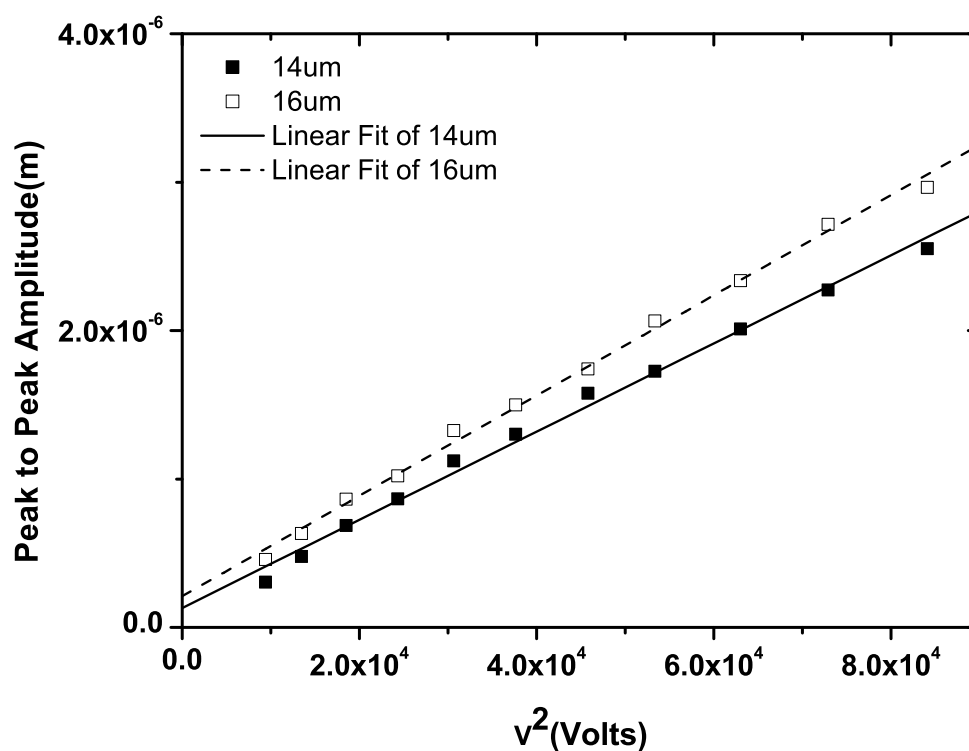
Figure 5.15: Graph showing Peak to Peak amplitude of the surface undulation as a function of applied voltage squared and 1-Decanol thickness for 80μm pitch electrodes
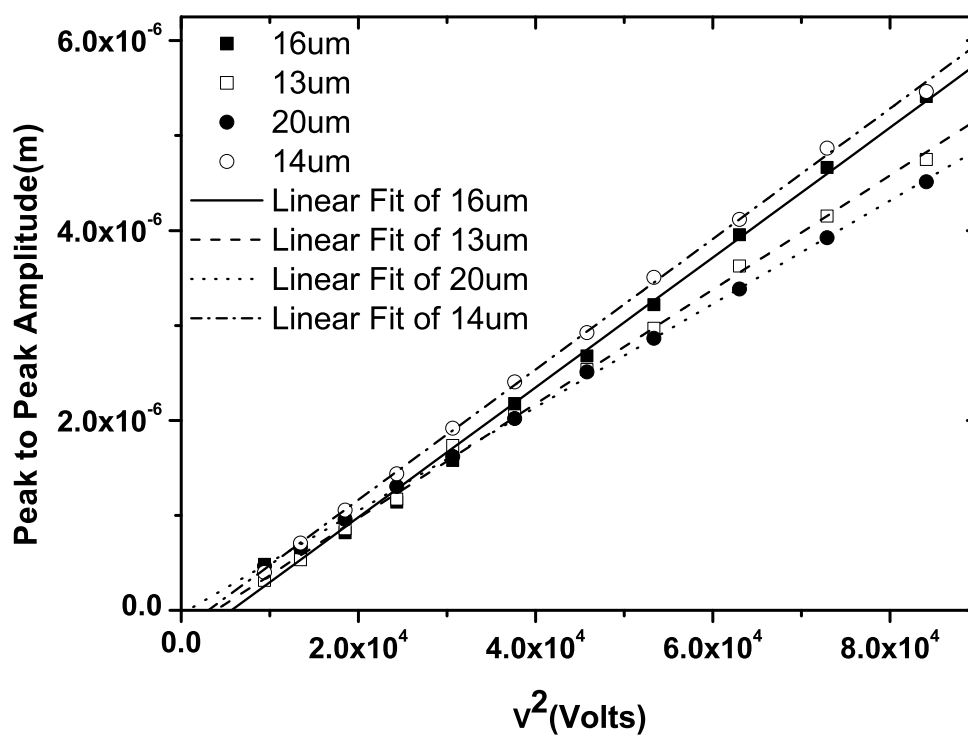
Figure 5.16: Graph showing peak to peak amplitude of the surface undulation as a function of applied voltage squared and 1-decanol thickness for 160μm pitch electrodes
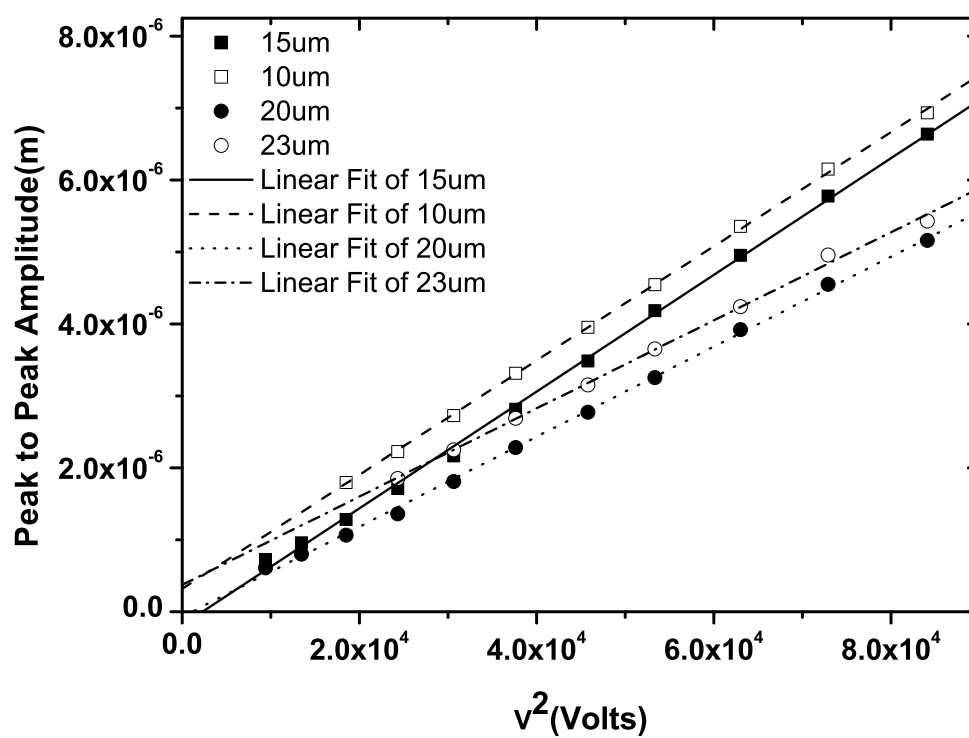
Figure 5.17: Graph showing peak to peak amplitude of the surface undulation as a function of applied voltage squared and 1-decanol thickness for 240μm pitch electrodes
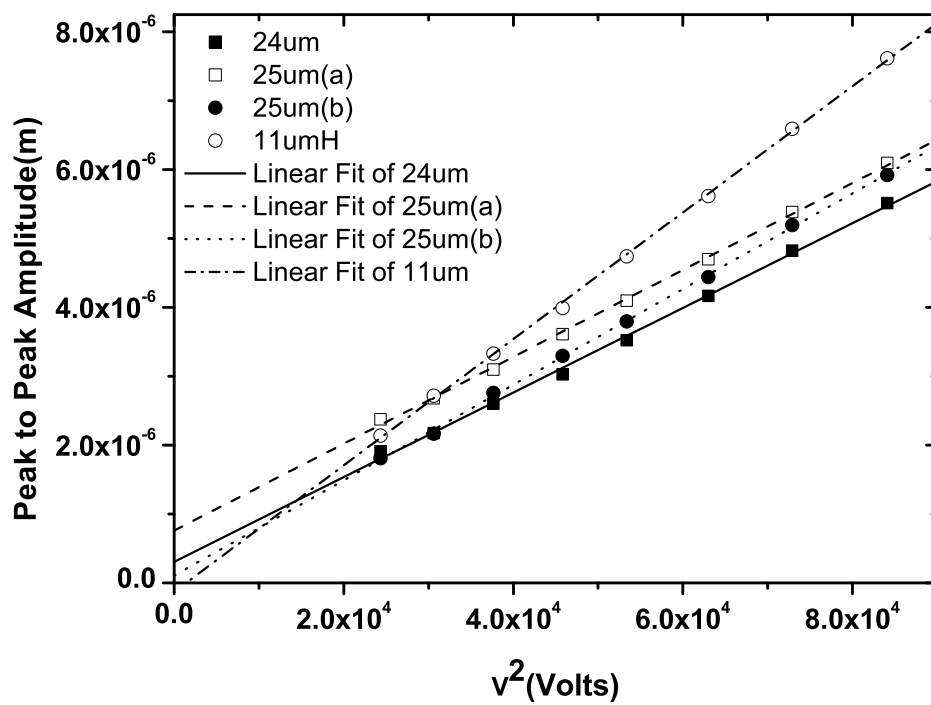
Figure 5.18: Graph showing peak to peak amplitude of the surface undulation as a function of applied voltage squared and 1-decanol thickness for 320μm pitch electrodes

Table 5.2: Linear fit to equation 5.1 for data in figures 5.11 through to figure 5.18

Oil	d(μm)	h(μm)	$\alpha \times 10^{-8}$	$\delta\alpha \times 10^{-8}$	$\beta \times 10^{-12}$	$\delta\beta \times 10^{-12}$
Hexadecane	320	10	-8.04	1.13	6.74	0.05
		14	-5.85	1.47	5.68	0.07
		12	-1.14	2.27	6.18	0.10
		22	-3.11	1.56	6.74	0.07
		29	-2.21	1.05	5.45	0.05
	240	14	-7.97	1.47	5.59	0.06
		12	-1.40	1.54	6.26	0.07
		40	-1.81	2.57	3.46	0.10
		45	-1.45	2.30	3.78	0.10
	160	13	5.33	3.58	9.04	0.16
		15	5.03	1.94	6.55	0.09
		20	-7.13	2.14	3.69	0.09
		21	-4.09	1.54	2.44	0.07
	80	9	-1.21	2.59	3.26	0.11
		16	3.92	1.59	2.00	0.07
		14	1.19	1.77	1.72	0.08
		28	-6.50	3.07	1.21	0.11
1-Decanol	320	24	30.70	6.94	61.41	1.26
		25	76.00	4.57	63.04	0.83
		25	10.44	3.91	69.34	0.70
		11	-12.74	4.70	91.71	0.85
	240	15	-18.5	4.84	81.0	1.01
		10	31.77	2.83	79.37	0.54
		20	-6.91	3.29	62.57	0.69
		23	37.66	6.44	61.23	1.17
	160	16	-38.81	6.66	68.40	1.40
		13	-23.22	3.66	60.12	0.77
		20	-39.24	1.49	54.42	0.31
		14	-21.13	2.97	68.70	0.63
	80	14	13.07	3.91	29.70	0.82
		16	21.15	3.23	33.76	0.68

5.6 Modeling the Undulation

The equation $\Delta h = \frac{16\epsilon V_0^2}{3\gamma\pi^4} \exp\left(-\frac{2\pi h}{d}\right)$, which governs the amplitude of the ripple with respect to the parameters of the device, was derived for an applied voltage on a film of oil directly on top of the electrodes by considering the change in the dielectric energy stored in the liquid and the interfacial energy stored in the assumed sinusoidal wrinkle of the liquid-air interface above the electrodes and minimising with respect to the wrinkle amplitude. The assumptions made are:

1. The wrinkle amplitude is small ($A << p$).

2. The periodic potential profile due to the electrodes, $V(x, y)$ is described by a Fourier series expansion to the second order only.

3. The potential profile is unperturbed by the presence of the oil/air interface.

4. The oil-air interface for the wrinkle is sinusoidal.

For a given electrode width and gap, a Fourier series expansion of the voltage profile can be made and the dielectric energy calculated [1]. To obtain an analytically tractable result in the calculation of the dielectric energy $W_E = \frac{1}{2}\mathbf{D} \cdot \mathbf{E}$, Terms to the second order were retained and the energy was then integrated over the fluid volume above the electrodes. The integral involves a series expansion for the case where the wrinkle amplitude is much less than electrode gap widths. The net result is an energy that depends on V_0^2, multiplying terms involving a factor with the wrinkle amplitude, and exponentials containing the wrinkle amplitude to pitch. The wrinkling of the liquid-air interface changes its area and this can be calculated for small amplitudes. The combination of these two energies was minimized with respect to changes in wrinkle amplitude.

The potential profile is a solution of Laplace's equation and can be determined for $y > 0$ if the boundary conditions at $y = 0$ are known. Assumptions are made such that the potential goes to zero as y goes to infinity and the thickness of the

electrodes can be ignored since they are much thinner than they are wide [1].
The boundary condition for the potential at $y = 0$ is shown in Figure 5.19.
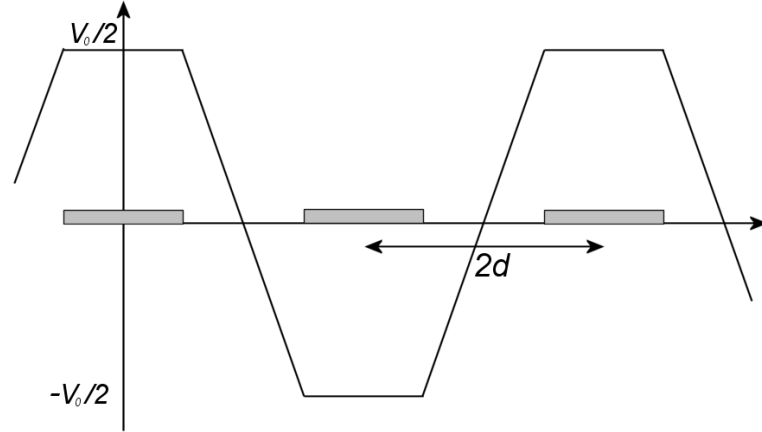
Figure 5.19: Boundary conditions for the potential at $y = 0$ used to solve the elctrical potential in the system

The potential profile crated by the electrodes is:

$$V(x, y) = \sum_{n=1}^{\infty} A_n cos(k_n x) e^{-k_n y} \tag{5.2}$$

Where A_n are the Fourier coefficients given by

$$A_n = \frac{8V_0}{\pi^2 (2m + 1)^2} cos[(2m + 1)\frac{\pi}{4}] \tag{5.3}$$

and

$$k_n = \frac{(2m + 1)\pi}{2d} \tag{5.4}$$

We calculate the electric field profile from

$$E(x, y) = -\nabla V \tag{5.5}$$

and thus calculate the energy W [44] from

$$W = \frac{1}{2}\mathbf{D} \cdot \mathbf{E} = \frac{1}{2}\epsilon \mathbf{E} \cdot \mathbf{E} \tag{5.6}$$

This then gives the energy as

$$
\begin{aligned}
2W ={}& \epsilon[A_1^2 k_1^2 \exp(-2k_1 y) + A_2^2 k_2^2 \exp(-2k_2 y) + \cdots \\
& 2A_1 k_1 A_2 k_2 \sin(k_1 x)\sin(k_2 x)\exp(-(k_1+k_2)y) + \cdots \\
& 2A_1 k_1 A_3 k_3 \sin(k_1 x)\sin(k_3 x)\exp(-(k_1+k_3)y) + \cdots \\
& 2A_1 k_1 A_3 k_3 \cos(k_1 x)\cos(k_3 x)\exp(-(k_1+k_3)y) + \cdots \\
& 2A_1 k_1 A_3 k_3 \cos(k_1 x)\cos(k_3 x)\exp(-(k_1+k_3)y) + \cdots]
\end{aligned}
$$

$$
\begin{aligned}
\text{where} \quad & k_1 = \frac{\pi}{2d}, & A_1 &= \frac{16V_0}{\pi^2}\cos\left[\frac{\pi}{4}\right] = \frac{16V_0}{\sqrt{2\pi^2}} \\
& k_2 = \frac{3\pi}{2d}, & A_2 &= \frac{16V_0}{9\pi^2}\cos\left[\frac{3\pi}{4}\right] = -\frac{16V_0}{9\sqrt{2\pi^2}} \\
& k_3 = \frac{5\pi}{2d}, & A_3 &= \frac{16V_0}{25\pi^2}\cos\left[\frac{3\pi}{4}\right] = -\frac{16V_0}{25\sqrt{2\pi^2}}
\end{aligned}
$$

The orders of the terms in the Fourier expansion are:

First Order $\qquad \exp(-2k_1 y) = \exp\left(\frac{-\pi}{d}\right)$

Second Order $\qquad \exp(-(k_1+k_2)y) = \exp\left(\frac{-2\pi}{d}\right)$

Third Order $\qquad \exp(-2k_2 y) = \exp\left(\frac{-3\pi}{d}\right), \qquad \exp(-(k_1+k3)y) = \exp\left(-\frac{3\pi}{d}\right)$

Terms in the expansion higher than the second order are ignored to give this equation 5.7

$$
W = \frac{8\epsilon V_0^2}{d^2\pi^2}\left[\exp\left(\frac{-\pi y}{d}\right) - \frac{2}{3}\cos\left(\frac{\pi x}{d}\right)\exp\left(\frac{-2\pi}{d}\right)\right] \tag{5.7}
$$

The electrical energy within the volume of oil is then found by performing a volume integral on equation 5.7 with the limits of the integral being the electrode pitch and the height of the oil from the electrodes. When evaluating this integral it is assumed, as previously stated, that $e^x = 1 + \frac{x^2}{2} + \frac{x^3}{6} + \ldots \approx 1 + x$ Thus

$$
W_T = \frac{8l\epsilon V_0^2}{d^2\pi^2} \int_{-2d}^{2d} \int_0^{h-\Delta h\cos(kx)} \left[\exp\left(\frac{-\pi y}{d}\right) - \frac{2}{3}\cos\left(\frac{\pi x}{d}\right)\exp\left(\frac{-2\pi}{d}\right)\right] dx\,dy \tag{5.8}
$$

Evaluating the integral using the previous assumptions leads to the equation for the energy stored in the volume of oil on the surface.

$$W_T = \frac{32l\epsilon V_0^2}{\pi^3} \left[\left[\exp\left(-\frac{\pi h}{d}\right) - 1 \right] - \frac{\pi \Delta h}{3d} \exp\left(-\frac{2\pi h}{d}\right) \right] \tag{5.9}$$

The inter-facial energy in the oil/air interface is found by performing a line integral of the sinusoidal undulation and multiplying by the inter-facial tension. Thus the length of the sinusoidal interface

$$L = \int_{-2d}^{2d} \left[1 + \left(\frac{dy}{dx}\right)^2 \right]^{\frac{1}{2}} dx \tag{5.10}$$

evaluating the integral gives

$$L = 4d \left[1 + \left(\frac{\pi \Delta h}{2d}\right)^2 \right] \tag{5.11}$$

and the energy in the surface is given by

$$W_I = 4dl\gamma \left[1 + \left(\frac{\pi \Delta h}{2d}\right)^2 \right] \tag{5.12}$$

By equating the energy in the volume with the energy in the surface of the oil we can say that the total energy in the system is the inter-facial energy minus the volumetric energy i.e. $W = W_I - W_T$ and for the interface to be in it's lowest energy state then $\frac{\partial W}{\partial \Delta h} = 0$, so for our system.

$$\frac{\partial W}{\partial \Delta h} = 8dl\gamma \left(\frac{\pi}{2d}\right)^2 \Delta h - \frac{32l\epsilon V_0^2}{3d\pi^2} \exp\left(-\frac{2\pi h}{d}\right) = 0 \tag{5.13}$$

And by rearranging to make Δh the subject we get

$$\Delta h = \frac{16\epsilon V_0^2}{3\gamma \pi^4} \exp\left(-\frac{2\pi h}{d}\right) \tag{5.14}$$

Equation 5.14 shows that the amplitude of the undulation created on the surface of the oil has a V^2 relationship to the voltage. The equation also shows that larger ripple amplitudes can be achieved by selecting a oil with a larger dielectric constant or a lower surface tension.

Equation 5.14 provides good design insight into the various physical properties needed to achieve the photonic effects, but experimentally there is a need for a calibration factor in the exponential term. Figures 5.20 and 5.21 show plots of $\ln(\frac{A}{V^2})$ versus $\beta(\frac{h}{d})$ (where A is the peak to peak amplitude of the ripple) for the undulation amplitudes in both hexadecane and 1-decanol where the pitch $p = 2d$. Linear regression analysis of the data in figures 5.20 and 5.21 give the following two scaling relationships of the form $\ln(\frac{A}{V^2}) = \alpha + \beta(\frac{h}{d})$:

$$\text{1-Decanol} \quad \ln\left(\tfrac{A}{V^2}\right) = (-23.00 \pm 0.03) + (2.70 \pm 0.14)\left(\tfrac{h}{d}\right)$$

$$\text{Hexadecane} \quad \ln\left(\tfrac{A}{V^2}\right) = (-25.71 \pm 0.02) + (2.89 \pm 0.07)\left(\tfrac{h}{d}\right)$$

The data gathered from the static undulation measurements of hexadecane and 1-decanol are also plotted in figures 5.22 and 5.23 where for each oil, the data has been plotted as amplitude versus $V^2 exp(\frac{\beta h}{d})$, where β is the constant which gives the best fit for the data from the previous regression analysis.

In figure 5.22 the data for hexadecane is best fitted to the model when β is -2.89 and in figure 5.23, the data best fits the model if β is set to -2.73. although these values for the constant β do not match the theoretical value 2π.

The theory leading to equation 5.14 has a number of approximations given in section 5.6. To keep it analytically tractable and produce a formula with the key dependencies correctly described. The Fourier modes are truncated and the complexities introduced by the dielectric layer and the interface at the oil-air boundary, are not taken into account. A complete theoretical treatment of the device would require corrections to the theory. However the scaling relationships for hexadecane and 1-decanol have been shown and the analysis correctly indentifies the dependencies on particular parameters.
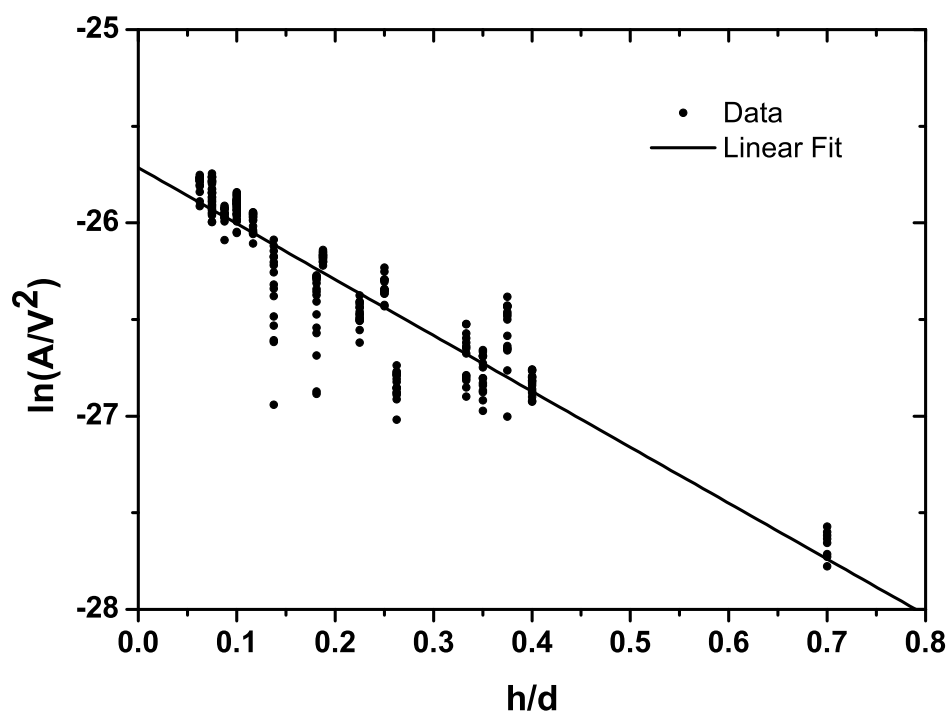
Figure 5.20: Plot of $\ln(\frac{A}{V^2})$ versus $(\frac{h}{d})$ for all the amplitude data on hexadecane. The linear fit to this data is shown as a solid line

Figure 5.21: Plot of $\ln\left(\frac{A}{V^2}\right)$ versus $\left(\frac{h}{d}\right)$ for all the amplitude data on Decanol. The linear fit to this data is shown as a solid line
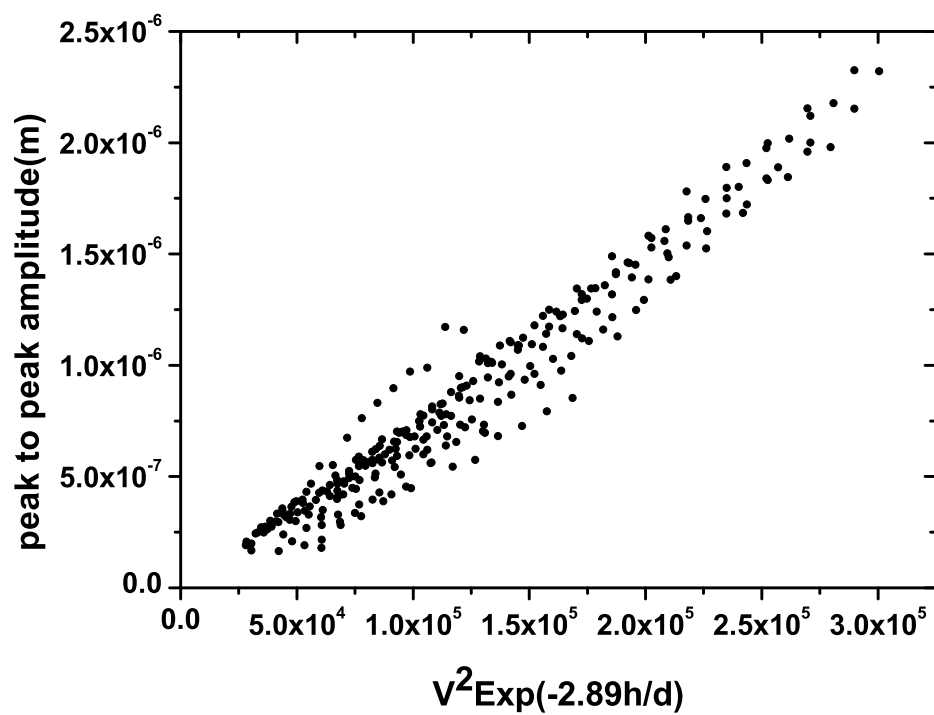
Figure 5.22: Graph showing the amplitude, of all data for samples with 2μm layer of SU8 and various thicknesses of hexdecane, against V^2 times the exponential function
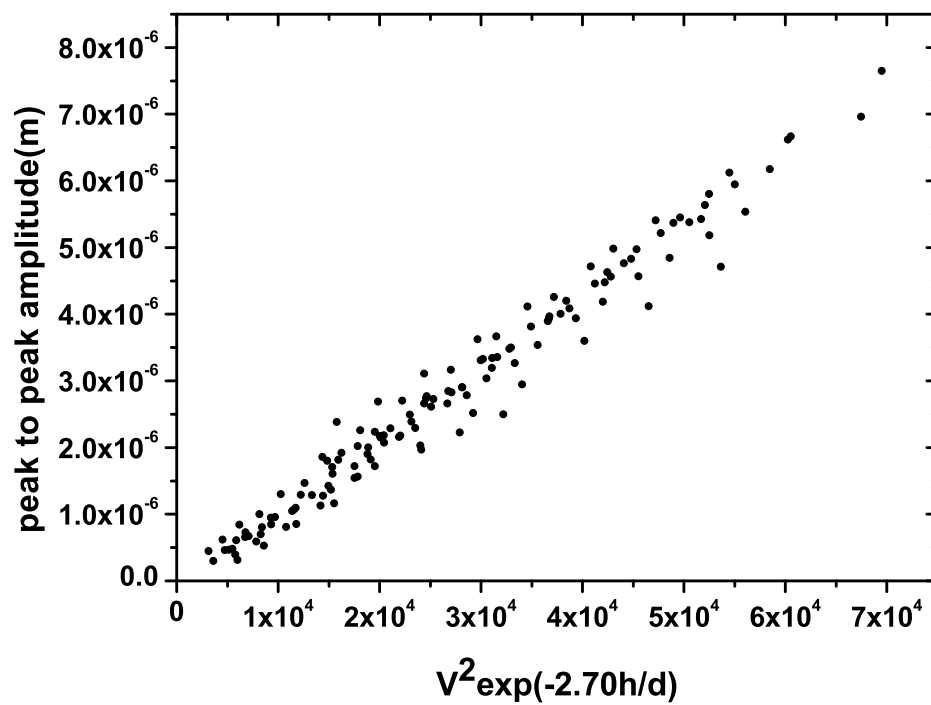
Figure 5.23: Graph showing the amplitude, of all data for samples with 2μm layer of SU8 and various thicknesses of 1-decanol, against V^2 times the exponential function

5.7   Phase Grating

As discussed in section 1.5.2 a device in which there is a periodic undulation in the surface of a transparent medium could, in theory, be used as a phase grating by causing the optical path length of any light passing through it to be periodically modified. This periodic modification of the optical path length would also lead to an interference pattern of various diffracted order spots. The intensity of the various order spots is directly dependent on the relative phase shift between the maximum and minimum value of the optical path length. The optical path length difference in our device can be varied by varying the amplitude of the undulation. The device was tested to verify that it could deflect the energy from the zero order undeviated spot into the other higher orders by using the voltage.

In order to test this hypothesis the device was illuminated either in reflection or transmission with a green laser ($\lambda = 543nm$) whilst in situ in the interferometer. The experimental setup for reflection experiments is described in sections 2.6.2 and for transmission experiments in section 2.6.1. For transmission experiments the dielectric coating above the electrodes consisted of a 2μm layer of SU8-10 photoresist, which was deposited using the method in section 2.3.3. For diffraction experiments in reflection the dielectric coating consisted of dielectric stack made up of 17 alternate layers of Titanium Dioxide (TiO_2) and Silicon doixide (SiO_2), which had thicknesses of 54.28nm and 87.22nm respectively. The total thickness of the stack was 1.13μm. The specification of the dielectric stack [110] was such that the red laser light, used to capture the interferograms, would be transmitted and the green laser light, used in the diffraction experiments, was reflected. In all of the following experiments the voltage applied was a 20kHz a.c. square wave. This voltage was modulated using the method described in section 2.4.4 for the experiments in section 5.7.1 and section 5.7.2.

5.7.1 Hexadecane in Transmission

The first device tested had an 80 μm pitch with a 2μm dielectric layer of SU8-10. It was illuminated in transmission with the green laser whilst being imaged in the interferometer. An a.c. 20kHz applied voltage was manually adjusted in 10V steps between 200V and 580V. A photodetector was scanned across the interference pattern at each interval and the maximum intensity of each spot between the -3 and +3 orders where measured. Figures 5.24 through to 5.27 show the variation in the peak intensity of the various order spots plotted against the voltage. Only the Peak intensity of the spots is plotted and the relative width of the spots has not been taken into account.

Figures 5.24 through to 5.27 show that the all the spots vary in intensity and it can be clearly seen that the zero order spot decreases in intensity to a minimum at around 450V whilst the first, second and third order spots increase to a maximum at around 400V, 450V and 530V respectively. This observation is consistent with the theory of the intensities of the diffraction spots being dependent on the difference in optical path length between the peaks and troughs of the sinusoid or the amplitude of the sinusoid (section 1.5.4)[85]. In this case the phase shift is due to a difference in optical path length in traversing different regions of the undulating oil film. (See also section 2.5.4). However, if the oil was acting as an ideal thin sinusoidal phase grating, The spot intensity for the zero order should be zero at its first minimum (section 1.5.4 figure 1.20). It is clear that this is not the case. The intensity of the zero order has only decreased to 60% of its initial intensity. Other characteristics of figures 5.24 through to 5.27 are similar to that for a thin sinusoidal grating in that the intensity of the first, second and third order diffraction spots all rise to a peak as the amplitude of the undulation increases and the zero order falls to a minimum.
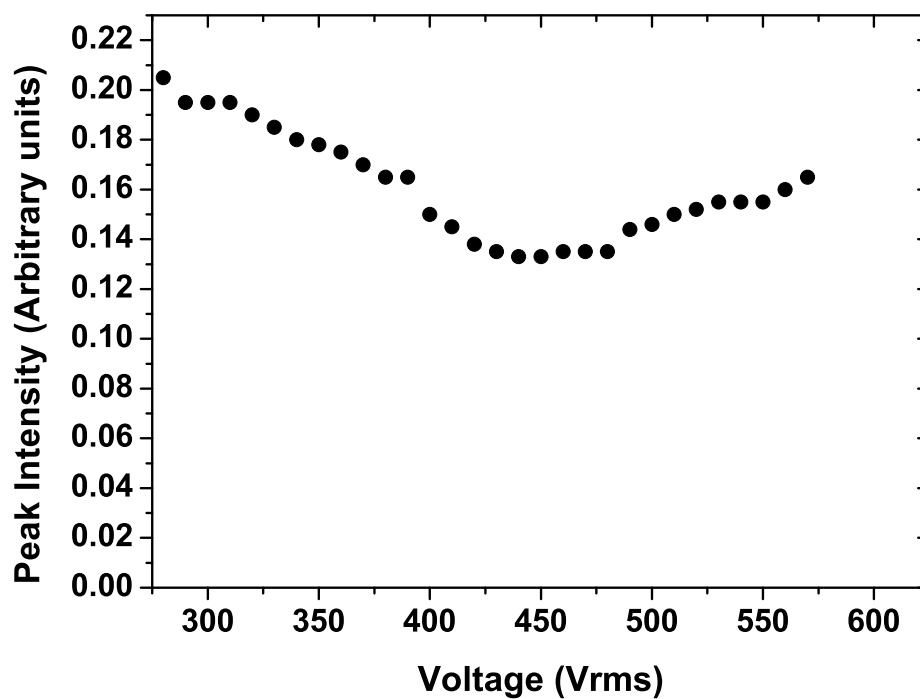
Figure 5.24: Graph showing the variation in Peak intensity for the Zero order diffraction spot for hexadecane in transmission
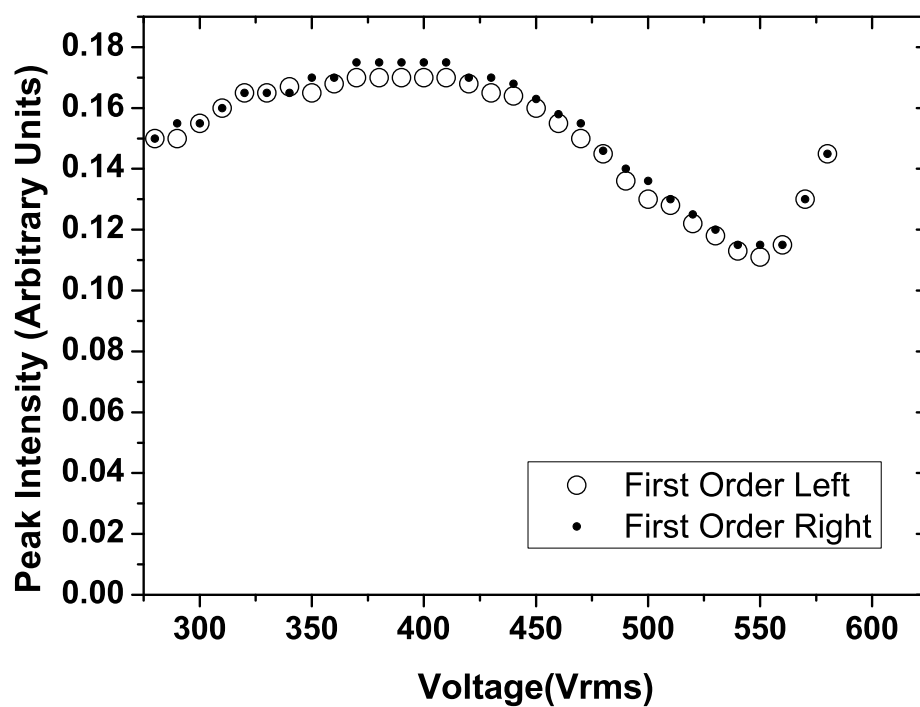
Figure 5.25: Graph showing the variation in Peak intensity for the first order diffraction spots for hexadecane in transmission
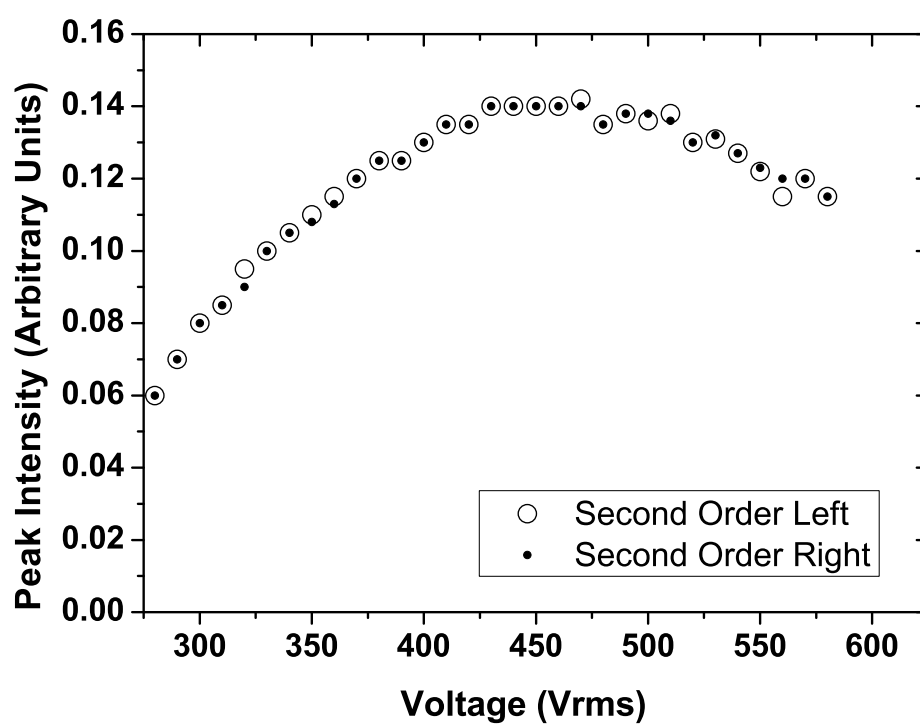
Figure 5.26: Graph showing the variation in Peak intensity for the Second order diffraction spots for hexadecane in transmission
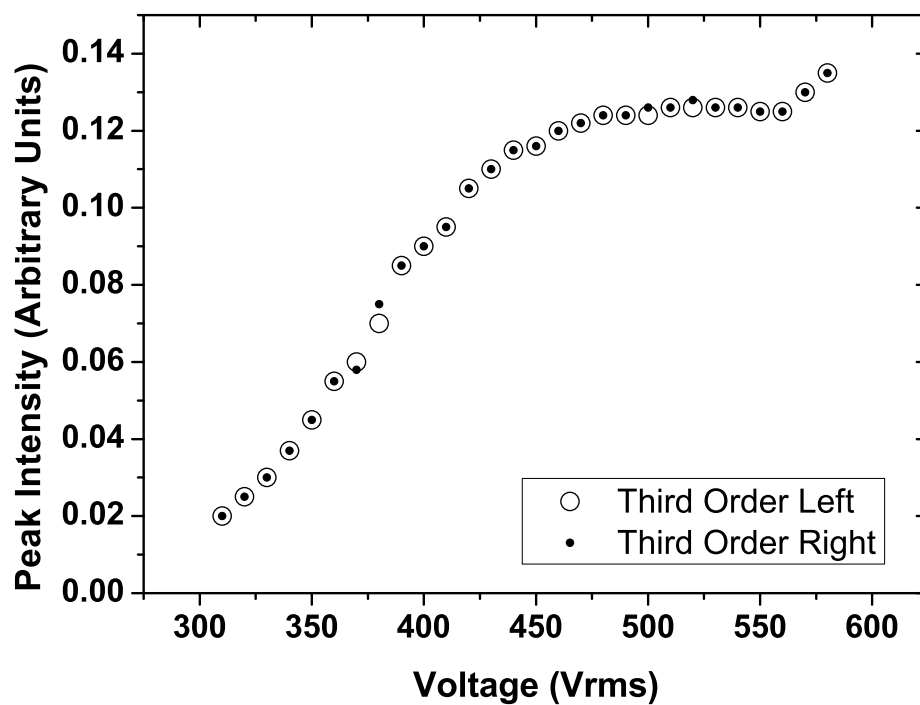
Figure 5.27: Graph showing the variation in Peak intensity for the Third order diffraction spots for hexadecane in transmission

5.7.2   Decanol in Transmission

Since the voltage at which first minima in intensities of the various order spots was so high and since equation 5.14 shows that the amplitude of the undulation can be increased by choosing an oil with a higher dielectic constant, the next experiment was done with 1-decanol as the oil layer. 1-Decanol has a dielectric constant of 8.1 and a surface tension very close to that of hexadecane of 28.4mN/m.

The same 80μm pitch sample was illuminated in transmission and the oil layer used was 1-decanol. The applied voltage V_o across the terminals was a 20 khz a.c. square wave which was modulated using a 1Hz triangular wave as explained in section 2.4.4. The photo detector was now kept in position on a particular spot of interest and the output through a complete cycle of the modulating triangular wave recorded and captured using an Agilent 54622A oscilloscope. This procedure was then repeated for the various order spots. At the same time the amplitude of the ripple was measured using the interferometer and the results are shown in figure 5.28 where the intensity traces for the zero, first, second, and third order spots are plotted against the voltage on the left hand axis and the amplitude is plotted against the voltage on the right hand axis.

From table 1.1 it is now possible to calculate the theoretical value for the peak to peak amplitude of the undulation at the maximum and minimum intensities for all the order spots.

The function is at a minimum or a maximum when $\frac{m}{2}$ is at one of the values given in table 1.1 from arguments in section 2.5.4 for a surface undulating such that the peak to peak amplitude is Δh the optical path difference is given by

$$\frac{2\pi}{\lambda_0}((h + \Delta h)n_{oil} - (hn_{oil} + \Delta h_{air})) = 2n \qquad (5.15)$$

Where n is a value of root of the Bessel function table 1.1 and rearanging for Δh we get

$$\Delta h = \frac{n\lambda_0}{\pi(n_{oil} - n_{air})} \tag{5.16}$$

From table 1.1 it is now possible to calculate the theoretical value for the peak to peak amplitude of the undulation at the maximum and minimum intensities for all the order spots when the device is used in transmission (Table 5.3).

Table 5.3: Ripple amplitude corresponding to the roots of the Bessel function 1.20

	n=0	n=1	n=2	n=0 Amplitude $\times 10^{-6}(m)$	n=1 Amplitude $\times 10^{-6}(m)$	n=2 Amplitude $\times 10^{-6}(m)$
min	2.41	0.00	0.00	0.97	0.00	0.00
max	3.83	1.84	3.05	1.53	0.74	1.22
min	5.52	3.83	5.13	2.21	1.53	2.06
max	7.02	5.33	6.71	2.82	2.14	2.69

In order to avoid saturation of the photodiode in this preliminary experiment the intensity of the Zero order spot was reduced by the introduction of a rotated polarizing filter into the path of the green laser before it entered the device. For this reason the relative intensities of the spots do not match with theory i.e. the sum of the powers in all the spots is not equal to the total incident power [85] (section 1.5.4) From figure 5.28, the sum of the first and second order powers is greater than that of the undeviated zero order.

It is also clear that the minima and maxima in the intensities of the spots do not correlate with the theoretical values calculated in table 1.1 and thus in this experiment the 1-decanol layer is not acting as an ideal sinusoidal phase grating. However this graph does show the feasibility of the device as a sinusoidal phase grating.

5.7.3 Decanol in Reflection

The values of the undulation amplitude can also be calculated for the minima and maxima in the various diffraction order spots when the device is used in reflection. In this case Equation 5.16 becomes:
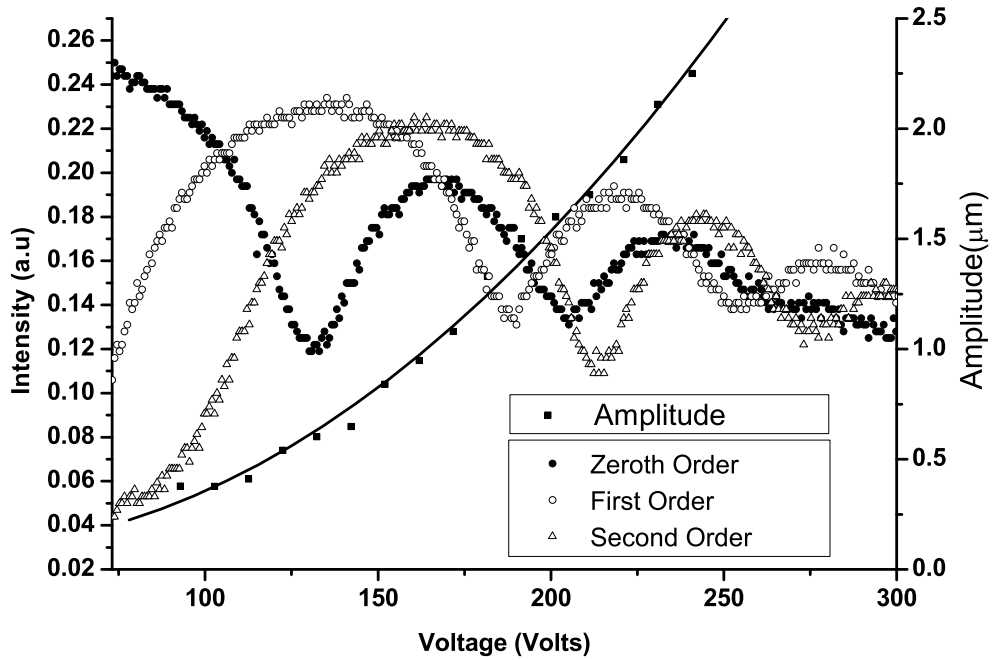
Figure 5.28: Graph showing the variation in intensity for the various order spots for 1-decanol in transmission and the amplitude of the undulation

$$\Delta h = \frac{n\lambda_0}{2\pi(n_{oil} - n_{air})} \tag{5.17}$$

Since the light traversing the oil layer travels from the oil-air interface to the electrode surface and back to the interface, the optical path length difference for a particular amplitude of undulation is effectively doubled. Since the amplitude of the device is proportional to V^2 using the device in reflection mode should also lower the operating voltage.

The calculated amplitude values are given in table 5.4

In this experiment the SU8-10 dielectric layer was replaced with a dielectric stack layer described in section 5.7. In this situation the green incoming light passes through the oil air-interface is reflected from the dielectric stack and again passes through the interface.

Figure 5.29 shows the equivalent plot as for the previous transmission experiment except the device is in reflection. In the transmission experiment, the point

Table 5.4: Ripple amplitude corresponding to the roots of the Bessel function for the device operated in reflection mode 1.20

	n=0	n=1	n=2	n=0 Amplitude $\times 10^{-6}(m)$	n=1 Amplitude $\times 10^{-6}(m)$	n=2 Amplitude $\times 10^{-6}(m)$
min	2.41	0.00	0.00	0.48	0.00	0.00
max	3.83	1.84	3.05	0.77	0.37	0.61
min	5.52	3.83	5.13	1.10	0.77	1.03
max	7.02	5.33	6.71	1.41	1.07	1.35
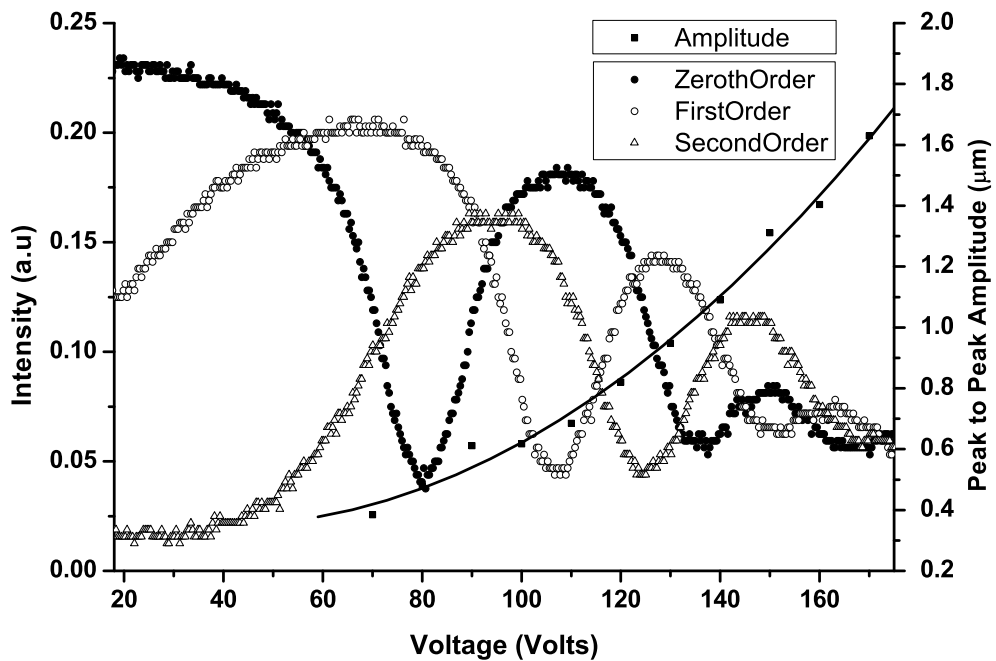
Figure 5.29: Graph showing the variation in Intensity for the various order spots for Decanol in transmission and the amplitude of the undulation

at which the zero order spot is at its minima is at 132 V_{rms}. In the Reflection mode the same corresponding first minima occurs at $80V_{rms}$ Thus, by operating the device in reflection the operating voltage has been reduced as expected.

Again the relative intensities of the various spots do not fit with theory since different beam intensities were used in each case.

5.7.4   Shorter Pitches

A 20μm pitch sample was used and the layer of 1-decanol had an average thickness of 3μm. The dielectric layer of the sample was a 2μm layer of SU8-10 photoresist and the device was illuminated in transmission. The applied voltage was again modulated with a triangular wave as in section 2.4.4. However, on this device, the scale of the electrodes did not allow for accurate imaging of the amplitude of the undulation at the same time as measuring the intensity of the diffraction orders.

Figure 5.30 shows the intensity of the zero, first and second order spots as a function of applied voltage squared. The minima and maxima are marked on the graph where the first subscript refers to the order of the spot and the second subscript refers to which maximum or minimum is being used. i.e. max_{01} refers to the first maximum in the zero order spot. The intensities of the spots relative to each other are correct because in this experiment the same intensity reduction was used for all of the spots. The ratio of the intensity of the first to the zero order peaks is 32.6%. This is close to the value of 33.8% that would be predicted by the Fraunhofer approximation for a thin sinusoidal phase grating [85].

Since the amplitude is proportional to V^2 the ratios of the positions of the maxima and minima in the intensity can be compared with the theoretical roots of the Bessel function by reading these points from the data in figure 5.30. Table 5.5 shows both the theoretical and actual values of these calculations. These values show a reasonable correlation with theory when the amplitude of the undulation

is small but the correlation is not so good as the amplitude increases. By looking back at table 1.1 and considering the fact that the electrode pitch is 20μm then we can see that assumption that the amplitude is small compared to the electrode pitch used in the derivation in section 5.6 is not true. Thus the V^2 relationship may no longer be true.
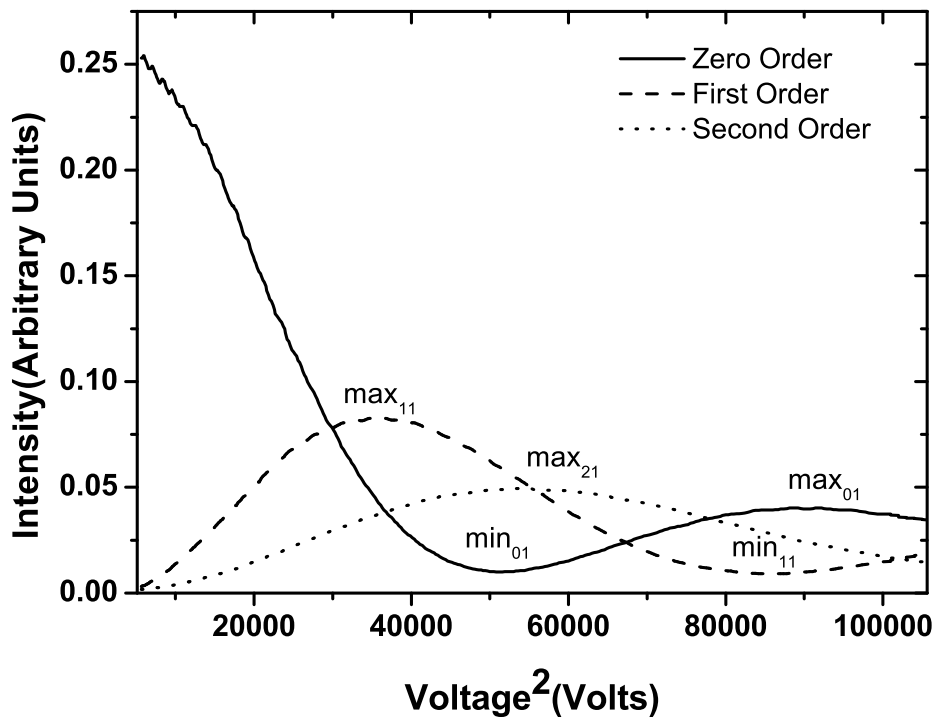
Figure 5.30: Graph showing the intensities of the diffracted orders of a 543nm transmitted green laser through a 3μm layer of 1-decanol

Table 5.5: Comparison of the ratios of the positions maxima and minima in figure 5.30

Ratio	Actual	Theoretical
max_{11}/max_{21}	0.65	0.60
max_{21}/max_{01}	0.53	0.79
min_{01}/min_{11}	0.59	0.62

5.8 Dynamic Switching and Relaxing

Section 5.7 shows that the device is capable of being used as amplitude programmable phase diffraction grating. i.e. the amplitude of the ripple, and thus the applied voltage, can be used to divert light from the first zero straight through diffraction order into the higher order diffraction spots. The next experiments were performed as preliminary experiments in order to gain some insight into the switching capabilities of the device.

The switching speed of the device was measured on an 80μm pitch device with a dielectric stack. The device was thus illuminated in reflection with the green laser and the applied voltage was switched discontinuously between a high and a low voltage by means of modulating the applied signal with a square wave. The frequency of the modulation signal was 200Hz. The low voltage of the modulating signal was just sufficient to keep the oil spread into a thin film. The high voltage was adjusted to achieve a peak in the intensity of the first diffracted order for each thickness of the 1-decanol layer. Three different thicknesses of 1-decanol where measured h=20μm, 18μm, and 14μm with the respective high voltage values of V_0= 93, 90 and 86V. The interferometer was used to simultaneously measure the amplitude (A) of the ripple. The maximum in the first order spot intensity was found to be A=0.36μm for all cases. Figure 5.31 shows the data for the low to high voltage transition labelled 'switch' and the high to low transition, labelled 'relax'. The times for the intensities to change from the value at 0 μs to 90% of the difference between the initial and the asymptotic intensities were 35μs, 40μs, 49μs (switching) and 79, 89, 108μs for h= 20μm, 18μm and 14μm respectively.

5.9 Conclusion

By placing a small drop of hexadecane or 1-decanol onto a dielectric surface, under which an interdigitated array of electrodes have been pre fabricated, it has
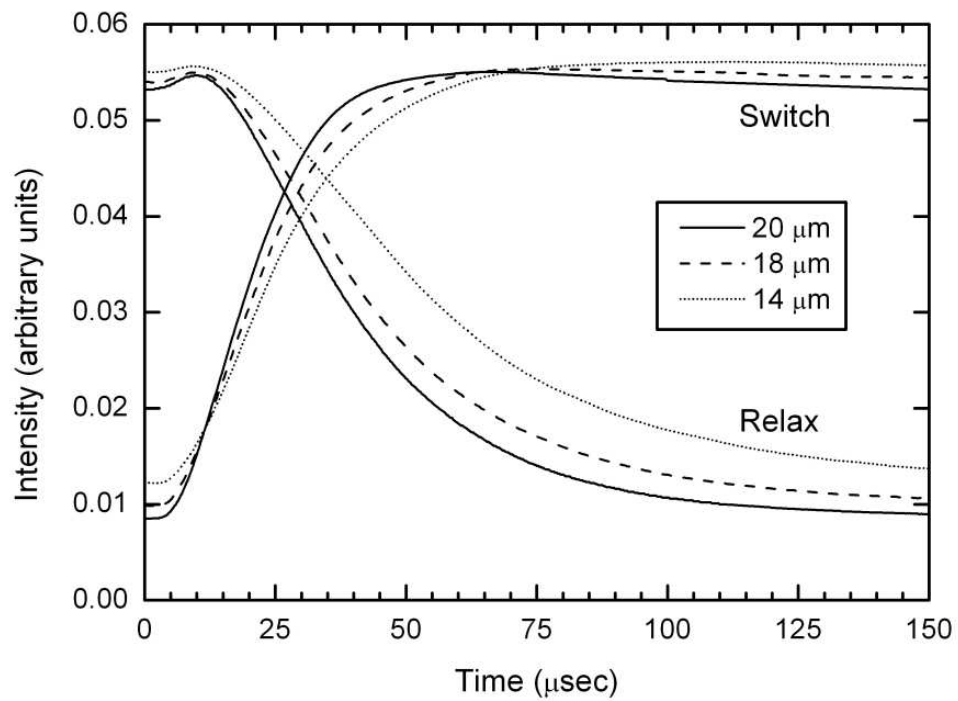
Figure 5.31: Graph showing switch and relax times for the first order spot of a 40μm pitch sample at various thicknesses of oil

been shown that the oil can be drawn into a thin film which uniformly covers the electrodes by applying a voltage between the electrodes. The thickness of the layer is almost independent of the applied voltage and on the application of higher voltages an undulation is induced in the oil/air interface. This undulation forms because of a dielectrophoretic force due to highly non-uniform fields created by the electrode pattern. This force changes the hydrostatic pressure in the layer of liquid and causes it to gather in regions of high field gradient. The shape of the undulation is to some extent governed by the position directly above the electrode with resistive losses causing shape variation at the very tips of the electrodes. Experimental data for the peak to peak ripple amplitude relationship to the applied voltage for two different oils, hexadecane and 1-decanol, has been shown. This data shows that the ripple amplitude is proportional the applied voltage squared and exponentially proportional to the ratio of the thickness and electrode pitch. A first approximation for the ripple amplitude has been derived and shown to be consistent with the observed data within the assumptions of the model. The device has also been used as a phase diffraction grating and the feasibility of the device as both a reflection phase grating and a transmission phase grating have been shown. The dimensions of the grating have been further scaled down and shows a better agreement with the theory of an ideal sinusoidal phase grating.

Chapter 6

Non Sinusiodal Wrinkles

6.1 Introduction

Under certain conditions the shape of the undulation at the liquid/air interface
can assume non sinusoidal forms. Although the modelling in Chapter 5 did not
incorporate a non-sinusoidal profile in its derivation, these surface profiles are
still an interesting phenomenon. For this reason this chapter is included as a
preliminary study of these arbitrary surface profiles and their dependence in the
oil thickness and the applied voltage.

The shape variation of the undulation is due to the spatial variation in the
electric field in the direction of increasing distance from the plane of the elec-
trodes. This is also seen in figure 6.1 [1] where an analytical solution to the
dielectrophoretic forces generated by interdigitated electrode arrays has been pro-
duced using a Fourier series approximation [1] similar to that used in chapter 5.
In figure 6.1, which shows the magnitude of the DEP force plotted on a logarith-
mic grey scale, the highest DEP force is generated at the edge of the electrodes
[2, 108, 111]. In terms of oil on the surface this plot shows that oil in a region
directly between two electrodes and very close to the surface would feel a force
drawing it from in between the electrodes towards the outer edge of the electrodes.

It has been shown that in regions far from the electrode plane the electric
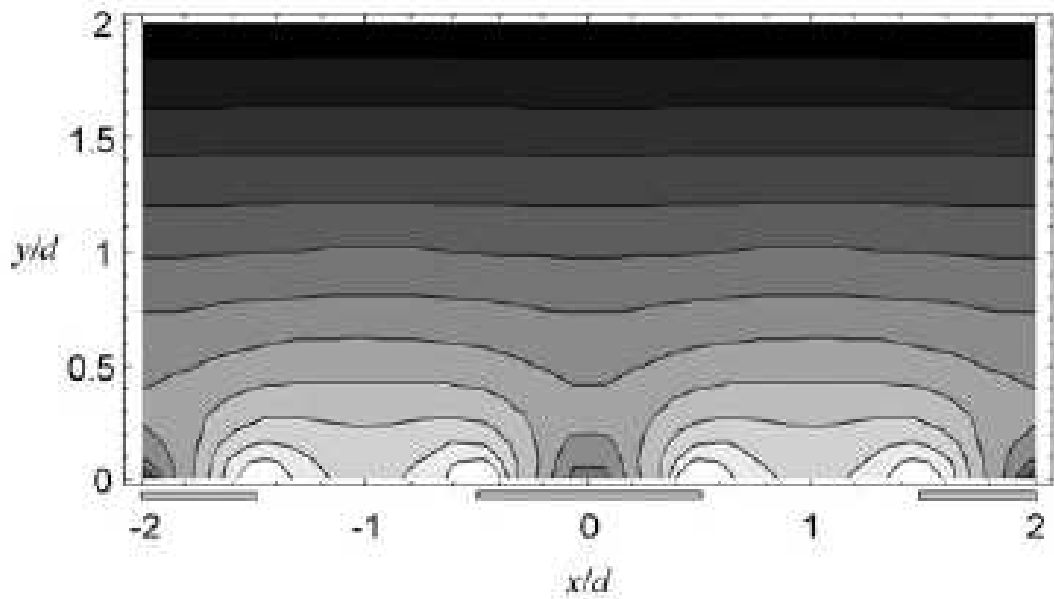
Figure 6.1: Contour Plot of the magnitude of the DEP force Plotted on a logarithmic grey scale. Image taken from [1] ©2001 IOP Publishing Ltd

field are dominated by the first order spatial harmonic components, whilst in regions closer to the electrode surface the higher order harmonics of the electric field become more prominent. [108, 112]. This dependence is shown in figures 6.2 [2] taken from Wang et al, where the E^2 field is plotted 2μm from a surface. The electrodes are marked as bold lines on the y-axis. The highest field gradients on this diagram occur in the regions just on the inside edge of the electrodes. i.e. between 5μm and 10μm and 30μm and 35μm. There are also smaller field gradients on the outside edges of the electrodes. Since, as seen in equation 1.19, the force on a dielectric liquid due to a non uniform field is proportional to $\nabla \mid E \mid^2$.

Since the DEP force is given by the equation $\mathbf{F} = \frac{1}{2}\alpha\nu\nabla|E_e|^2$ then the force on a dielectric medium in the electric field shown in figure 6.2 could be obtained by the gradient of the field magnitude squared. This would lead to a high force drawing the medium to the regions just inside the electrode edge as mentioned previously and also a slight force towards the outside edge of the electrodes.
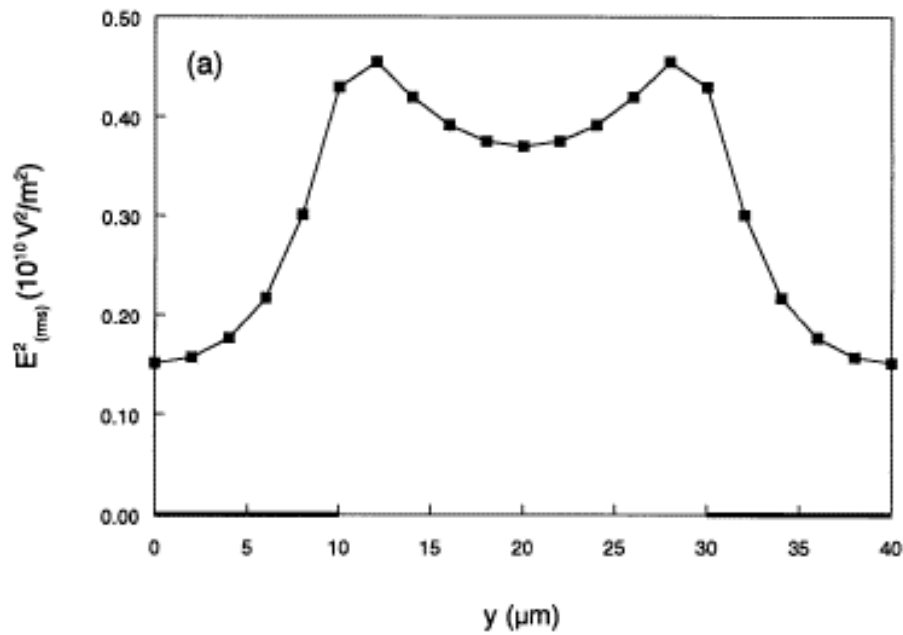
Figure 6.2: Plot of the E^2 field from Wang et al 1996 at 2 μm from the electrode plane [2] ©1996 IOP Publishing Ltd

6.2 Undulation Shape and Layer Thickness

Figure 6.3 shows the surface shape created by hexadecane oil under voltage on electrodes with a 320μm pitch. The thicknesses shown are 6.0μm, 9.0μm, 16.5μm and 30.0μm each thickness has profile extracted for five different voltage 275V, 325V, 400V, 475V, and 550V. The hexadecane layer thickness is marked on the right hand axis and has been vertically displaced for ease of viewing. The graph shows that as the ratio $\frac{h}{d}$ decreases the surface of the undulation becomes non-sinusoidal due to the increasing contributions of the higher order spatial components of the electric field [112].
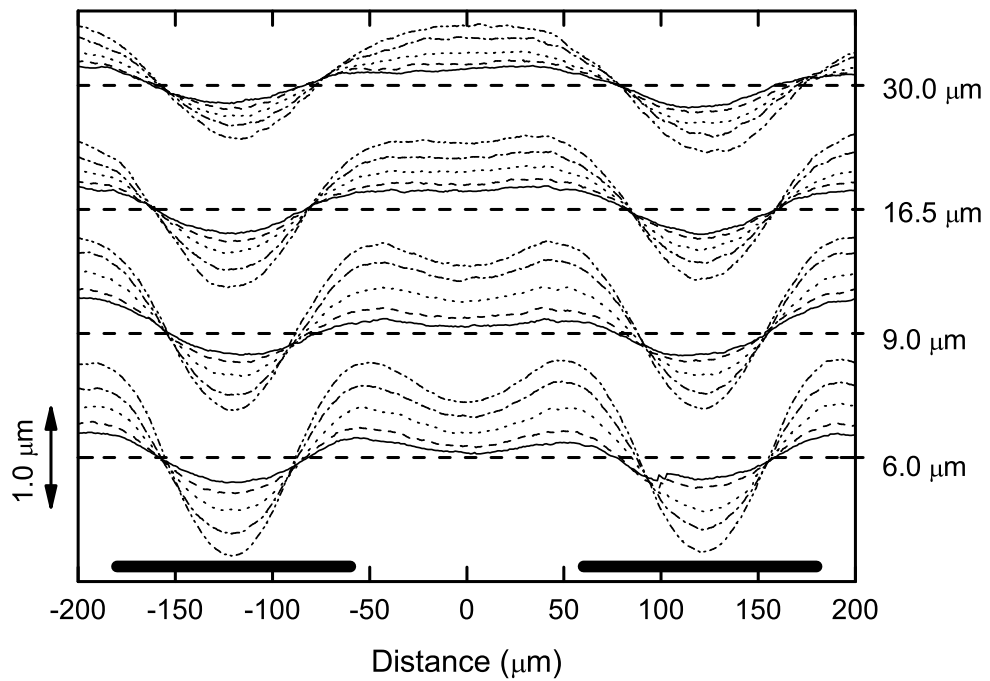
Figure 6.3: Experimentally extracted surface profiles showing the Undulation shape variation with thickness for Hexadecane oil on 340μm pitch electrodes. The profiles were obtained using the Mach-Zendher interferometer

6.3 Spatial Components of the Electric field

6.3.1 Spatial Components and Layer Thickness

The different spatial components of the electric field decay at different rates with increasing height from the electrode plane [112]. The higher order components of the electric field decay much more quickly than the lower order components. In order to see how these components manifest and decay in the surface of the oil, the Fourier components, for the surface profiles of a hexadecane layer with thicknesses of 6, 8, 9, 16.5, 19, 30μm at 550V, were extracted using an Excel spreadsheet. The resulting coefficients where then plotted using the theoretical curve of the form

$$F(x) = A_0 + A_1 \cos(x) + A_2 \cos(2x) + A_3 \cos(3x) + \cdots \qquad (6.1)$$

The theoretical curve was matched with the data from the surface profile and figure 6.4 shows a typical fit of the theoretical equation created using the extracted Fourier components against the actual data of the surface profile.The data from the profile is shown as open circles and the black line shows the fourier series fit for the data. Once this fit is matched with the surface profile the components of the oil surface shape are extracted and the rate of decay with increasing oil thickness is plotted.

Figure 6.5 shows the natural log of A_1, A_2 and the A_3 coefficients in equation 6.1 plotted against the thickness to electrode ratio $\frac{h}{d}$. The Higher order coefficients decay faster than the lower order coefficients as expected. This reproduces the experimental result shown in figure 6.3 that as the thickness of the oil decreases the higher order components of the electric field play a greater role in the shape of the oil/air interface. The data shown in figure 6.5 is only preliminary and although the general expected decay trend is seen the actual rate of decay is not predicted from this data.
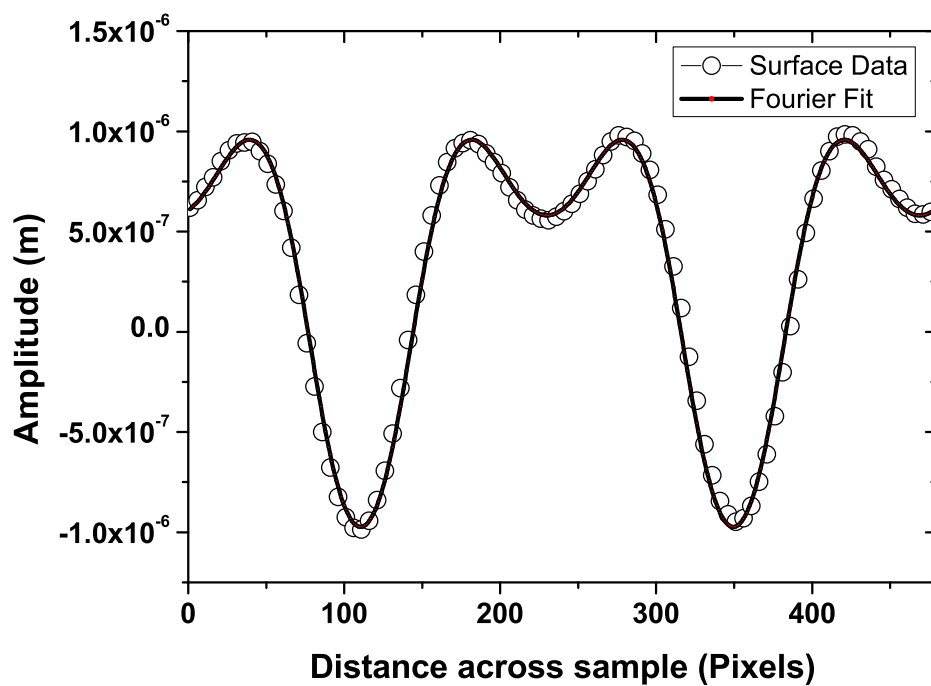
Figure 6.4: Graph showing a typical fit of the Fourier components of the surface profile of hexadecane oil in a 6μm layer. The theoretical line has been slightly displaced vertically for clarity.
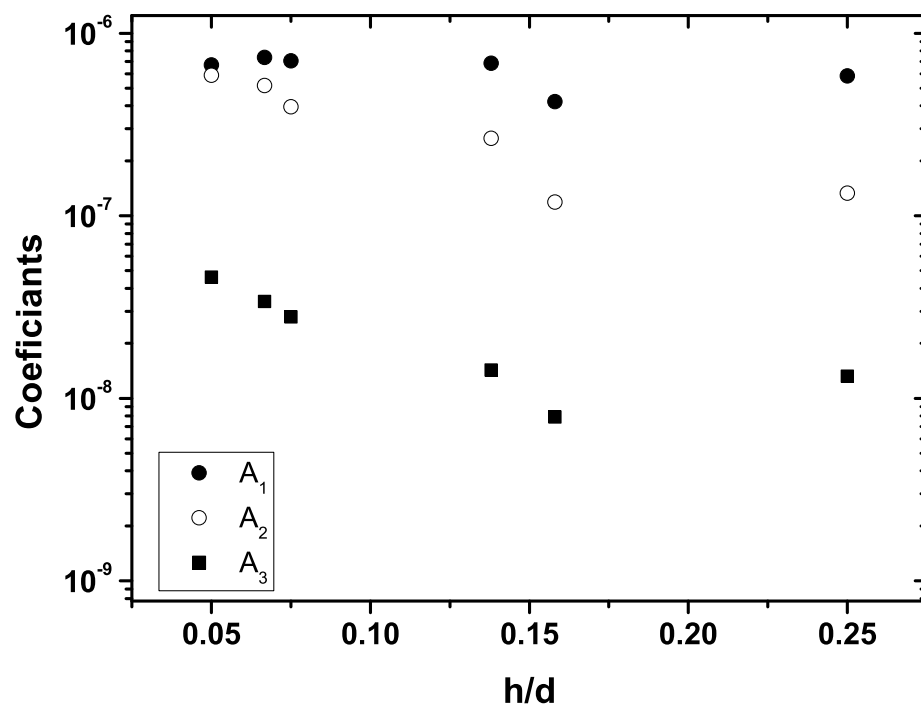
Figure 6.5: Graph showing the decay of the A_1,A_2 and A_3 constants in the Fourier series as a function of h/d

The relative contributions of these coefficients to the surface profile are shown in figure 6.6 It is clear that the contribution from the A_3 coefficient is very small and falls away wery quickly with thickness. For a thin layer of hexadecane there is a contribution from the A_1 and A_2 component but the A_3 coefficient falls away rapidly with increasing thickness.
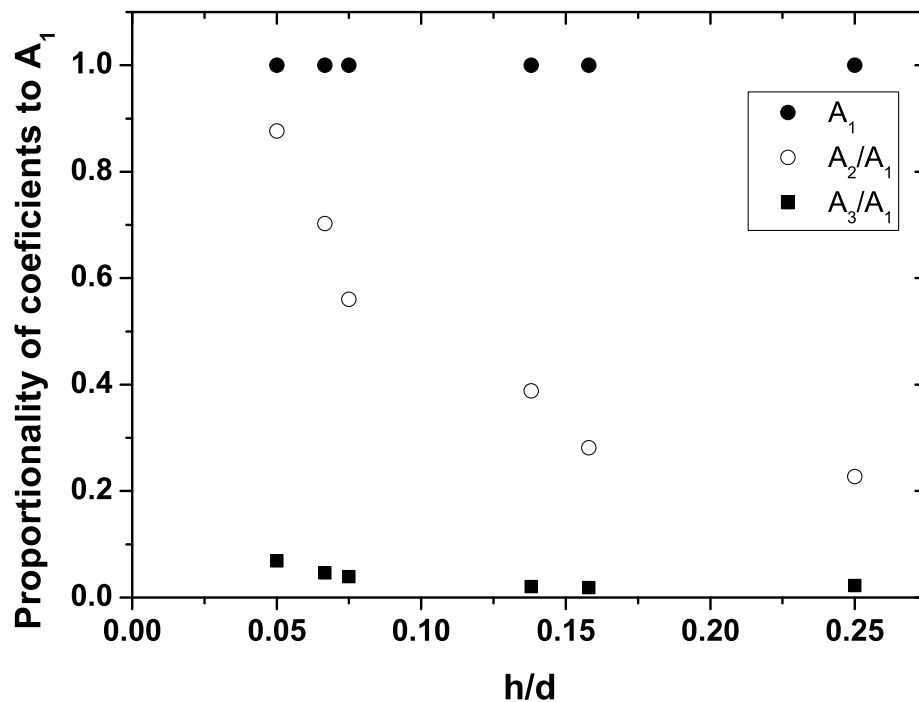
Figure 6.6: Relative contributions of the first three coefficients of the fourier series to the shape of the hexadecane surface. The A_2 component is plotted as an absolute value

6.3.2 Spatial Components and Voltage

The same technique of extracting the Fourier components in a hexadecane profile was used to see how the coefficients varied with applied voltage. The Fourier coefficients from the profiles of a hexadecane oil layer $6\mu m$ thick were extracted at different voltages. The results are plotted in figure 6.7 along with the linear fits for this data. The linear fit data is summarized below:

$$A_1 = (-2.82 \times 10^{-7} \pm 0.21 \times 10^{-7}) + (1.72 \times 10^{-9} \pm 0.05 \times 10^{-9})V$$

$$A_2 = (-1.97 \times 10^{-7} \pm 0.18 \times 10^{-7}) + (1.24 \times 10^{-9} \pm 0.04 \times 10^{-9})V$$

$$A_3 = (-0.50 \times 10^{-7} \pm 0.06 \times 10^{-7}) + (0.14 \times 10^{-9} \pm 0.01 \times 10^{-9})V$$
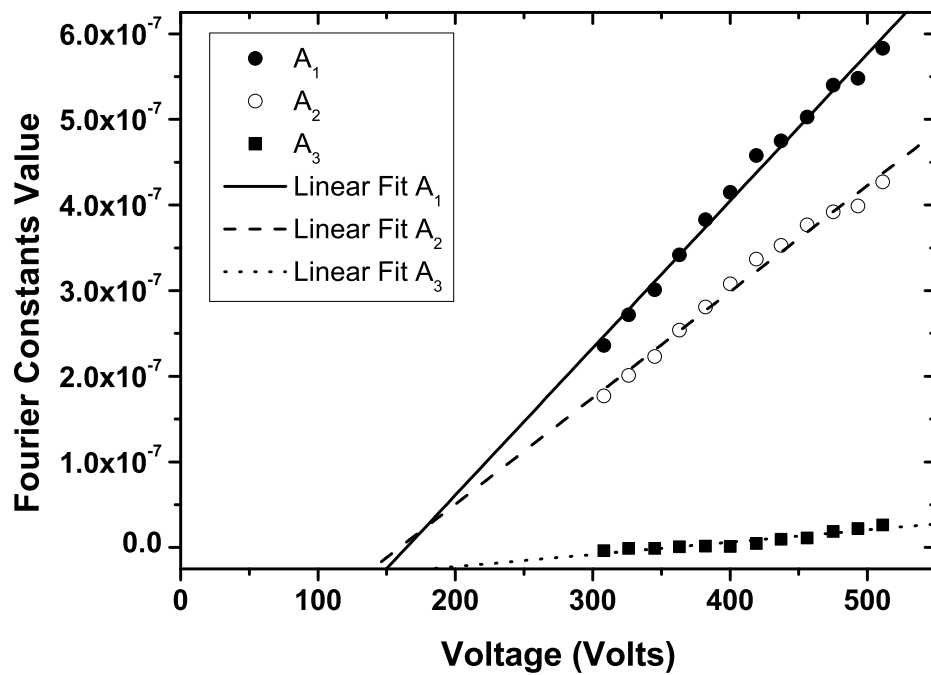
Figure 6.7: The a A_1, A_1 and A_1 coefficients of a 6μm hexadecane layer plotted as a function of voltage

The Fourier coefficients of the surface profile show a linear relationship with the applied voltage. The proportions of the coefficients contributions however, remain constant irrespective of the voltage. Figure 6.8 shows the A_1, A_2, and A_3 coefficients as a proportion of the A_1 coefficient against voltage. The shape of the oil in this voltage range is dominated by the A_1 and A_2 components of the field with very little contribution from the A_3 component. The proportions of the A_1 and A_1 constants contributing to the shape appears to be constant in this voltage range. However the A_3 does appear to be increasing very slightly but the contribution from this coefficient is very small to begin with.
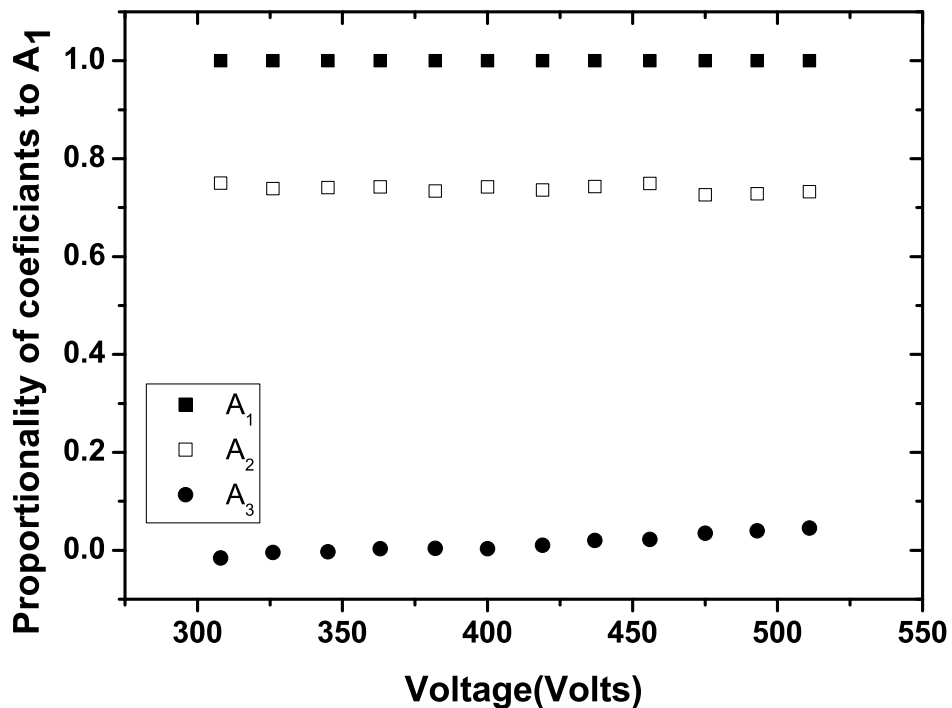
Figure 6.8: graph showing the Fourier coefficients of the surface of a 6μm thick hexadecane layer as a proportion of the A_1 coefficient.

6.3.3 The Effect of the Properties of the Oil on Surface Shape

The rate at which the Fourier coefficients present in the shape of the oil/air interface decay is also dependent on the properties of the oil used. Figure 6.10 shows interferograms of both hexadecane and 1-decanol oil taken at the maximum amplitude voltage, which is 584V and 300V for hexadecane and 1-decanol respectively. The magnification for each picture is unknown but it is the general shape of the surface which is of interest. The electrode width, and thus the half pitch values, as well as the oil thickness and the h/d ratio are given on the left hand side of each pair of pictures. This figure shows clearly that the hexadecane has a surface profile which is governed by the thickness of the oil. At a h/d ratio of 0.25 the surface has a sinusoidal profile and the higher order spatial components have decayed leaving only the A_1 component. At a ratio of 0.0625 A_2 components have become much more prominent. 1-decanol on the other hand has only the first order components at a h/d ratio of 0.25 and is still virtually sinusoidal at a ratio of 0.0625. 1- decanol has a dielectric constant of 8.1 as apposed to the 2.05 for Hexadecane and this is means that the contribution from the A_2 components of the electric field decay much faster with increasing thickness in 1-decanol.

This phenomenon is also seen in figure 6.10, where the profile of both 1-decanol and hexadecane are shown above electrodes with 320μm pitch. The thicknesses of hexadecane shown are 16 and 34μm and the thicknesses of 1-decanol are 12 and 26μm. Again whilst at 16μm the hexadecane is beginning to show signs of the higher order harmonics, these features are much less prominent in the decanol even at 12μm thick. This figure also shows that the amplitude obtained at equivalent thicknesses is much greater for a greater dielectric constant.
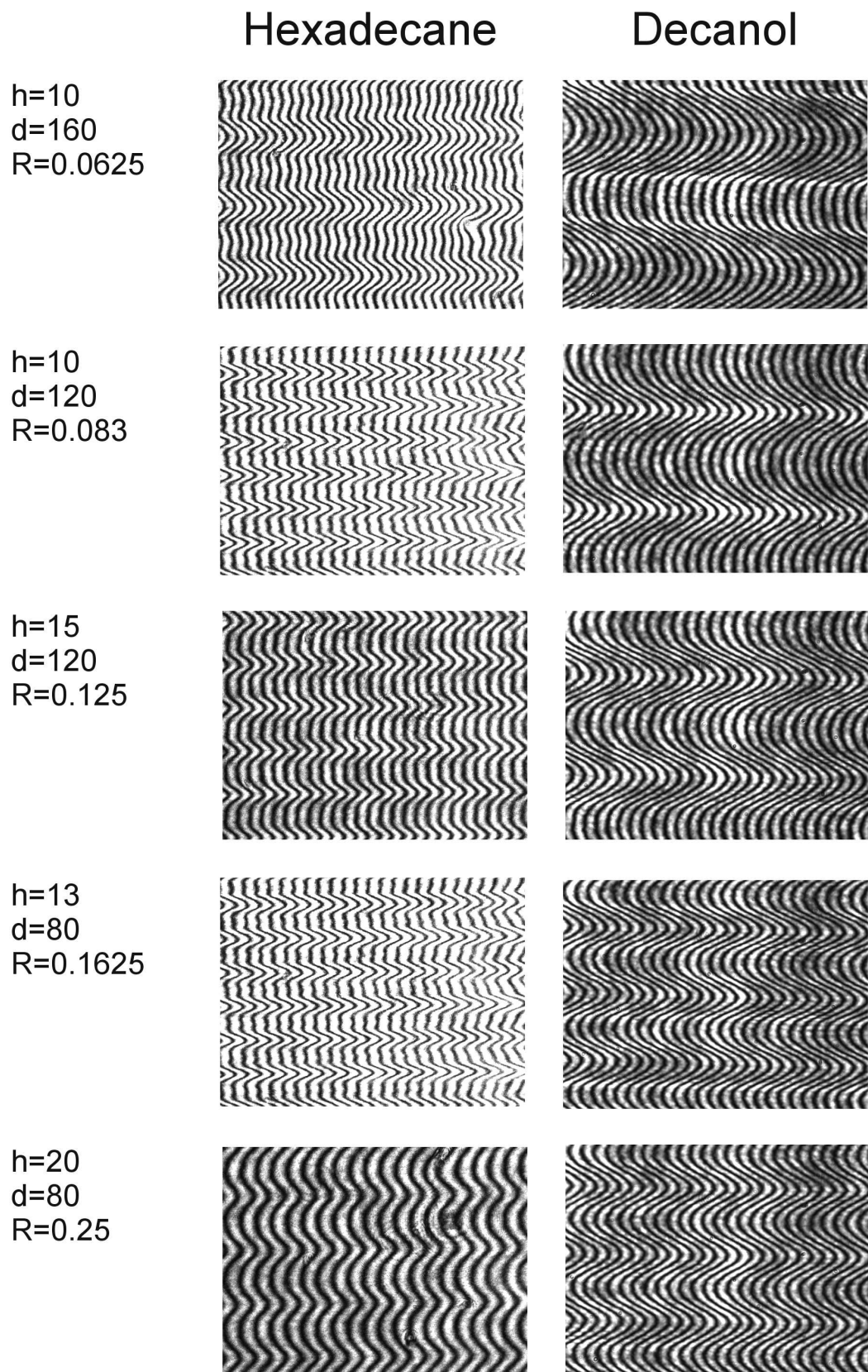
Figure 6.9: Graph showing the Undulation shape variation with thickness of hexadecane and 1-decanoloil on 340μm pitch electrodes.
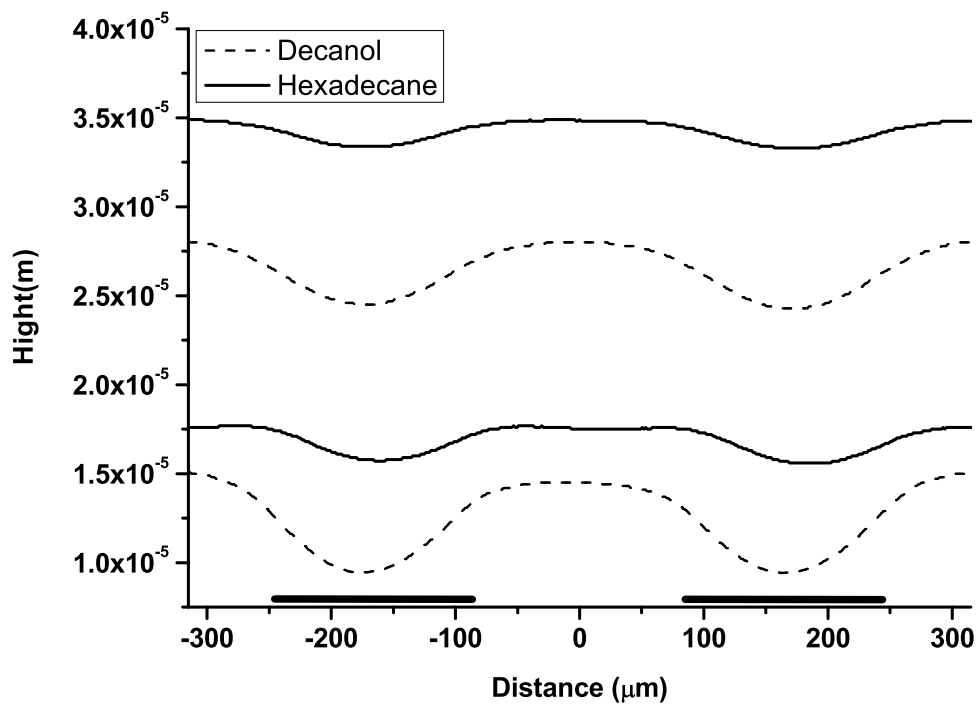
Figure 6.10: Graph showing the Undulation shape variation with thickness of Hexadecane oil on 340μm pitch electrodes.

6.4 Conclusion

It has been shown that in regions very close to the electrode surface the higher order spatial harmonics of the electric field play increasingly important role in the shape of the liquid layer. These harmonics fall away rapidly as the thickness of the layer is increased and the undulation in the surface tends towards a sinusoid. The main contribution comes form the A_1 and A_2 components in a thin layer of hexadecane with only very slight contributions from higher order components. The relative contributions from the A_1 and A_2 components remains constant in the voltage range shown but a slight increase in the A_3 components may be occurring at high voltages. However this is not yet clear and further investigation is required. The contributions of the A_2 components also appears to be much smaller in a layer of oil with a higher dielectric constant for the same layer thickness

Chapter 7

Conclusions and Further Work

7.1 Conclusions: Liquid Crystals

A multistable rotatable liquid crystal waveplate has been demonstrated by confining a small circular droplet of liquid crystal in a square well of dimensions $60 \times 60 \times 15 \mu m$. The confining well was produced using SU8-10 [113] photo resist and a photo lithographic process. The SU8-10 imparts a random planar alignment on the liquid crystal and the dimensions of the box ensure that short range order is maintained within the well. The result is that the average direction of the n-director lies in the plane of the droplet with what appear to be nematic defects at opposite edges of the circumference. The optical texture of the droplet was studied and the most likely n-director orientation inside the droplet has been shown to be a bipolar configuration. By positioning the box between electrodes with different relative orientations it has been possible to rotate the director with the application of an in plane electric field.

In the first instance with electrodes oriented at 40° to each other it was possible to rotate the droplet between two stable states with the director at the centre of the droplet pointing in the direction of the applied field. It was also found that for a perfectly circular droplet the director could be rotated to any direction between these stable states. The rotation of the droplet is shown to follow the

relationship $\theta = 0.472\tau V^2$. From this relationship we can see that the with a $100V_{r.m.s}$ driving voltage the angular rotation speed of the droplet is $450°/s$ at room temperature.

The temperature of the droplet has been shown to influence the size, shape and optical texture. The shape of the droplet at room temperature is governed by the initial volume of liquid crystal within the confining well. At room temperature larger initial volumes of liquid crystal in the well lead to a rounded square shape and with sufficiently small volume a circular shape. If the temperature is increased the droplet is seen to decrease in size until at temperatures above $35°$ the droplet eventually disappears the disappearance temperature is dependent on the initial volume within the confining well. When the temperature is then reduced the droplet recovers via the appearance of surface droplets which gradually coalesce to reform the initial droplet. This process is similar to that seen in spiniodal dewetting [98] in which a thin film of liquid on a surface spontaneously ruptures due the nucleation sites or thermal fluctuations in surface riplons. The temperature dependence of the shape also introduces interactions between defects at the free surface of the droplet and the walls of the confining well. For a droplet with sufficient volume to form a rounded square geometry at room temperature, the previously mentioned relationship of the rotation speed with voltage is lost due to the interactions of the defects with the well walls. As the temperature is increased the effect of the well walls on the free surface of the droplet is reduced, due to the reduction in size of the droplet, the droplet shape then tends more toward a circular disc and the relationship of rotation speed and voltage is restored.

The voltage-rotation speed relationship was also seen in devices in which the electrodes where oriented at $90°$ to each other. In this configuration the electric field applied to the device could be continuously rotated through $360°$. For a droplet which was circular at room temperature the minimum voltage required to maintain a continuous uninterrupted rotation, of the n-director, at a given

rotation frequency was shown to follow the same V^2 relationship. However when the temperature of the device was increased the minimum required voltage to maintain this smooth rotation was seen to decrease.

It was also found that if the rotation frequency of the electric field was increased at a given voltage or the voltage was decreased at a given frequency then the director could no longer rotate smoothly because the interactions of the defects with the well wall became more significant and prevented the director from following the rotating electric field. Several periodic regimes for this non-continuous rotation were observed and studied and the onset several of these regimes with respect to applied voltage and rotation frequency were examined.

For droplet with a rounded square geometry at room temperature the director orientation was seen to exhibit states similar to those seen in previous work where bistable liquid crystal devices where created by confinement in small wells with specific surface treatments [89]. With electrodes oriented at 40° to each other, it was found that the defects on the edge of the droplet could be moved to allow switching between stable states. The switching times versus voltage characteristic of four switching regimes were examined and an interesting outcome of this study was the ability to switch between a diagonal and vertical state and back again by applying only a vertical electric field. However, switching from the vertical to the diagonal required a much longer voltage duration and may be explained by a slight misalignment of the electrodes with respect to the confining well.

7.1.1 Future Work: Liquid crystals

By reducing the gap between the electrodes from 120μm to the order of the droplet diameter it should be possible to increase the speed of rotation by a factor of 5. It was also shown that the speed of rotation could be increased significantly by surface treatments to alter the anchoring forces imparted onto the droplet by the confining box.

Response times of 900 to 7200°/s have previously reported[48, 50, 51, 114] with voltage of 40-140V_{rms}. With the scaling relationships previously mentioned and reduction in the surface anchoring it should be possible to achieve equivalent rotation speeds. It may be possible to pruduce faster switching speeds using ferroelectric liquid crystals [115] and d.c. electric fields. However ferroelectric liquid crystals have a layer structure and this may have different interactions with the confining well.

7.2 Dieletrophoretic Phase Grating

It has been shown that a small droplet of Hexadecane or 1-decanol placed onto a surface which contains an interdigitated electrode array can be spread into a thin film by the application of a non-uniform electric field between the electrodes. This film is shown to be of uniform thickness which is virtually independent of the applied voltage and is only governed by the initial volume of oil dispensed onto the electrodes.

An undulation in the interface between the oil and the surrounding air can be created by the application of higher electric fields. this undulation is static, reproducible, and stable[105–107] when switched on. Data for hexadecane and 1-decanol on electrode pitches of 80, 120, 240 and 320μm at thicknesses various layer thicknesses ranging from 9 to 45μm thick have been shown.

A first approximation of the governing equation for the amplitude of the undulation against the properties of the device has been derived by considering the change in dielectric energy stored in the liquid and the energy stored in the interface of the assumed sinusoidal wrinkle and minimising with respect to the undulation amplitude. The model contains a number of assumptions and is based on the voltage profile for a given electrode width and gap being calculated as a Fourier series expansion[1] which is then used to calculate the dielectric energy. The data is consistent with the scaling predicted by the derived model. This

model does provide a good basis for future designs in that it correctly identifies the dependencies of particular parameters of the device such as the dielectric constant or surface tension of the interface.

The shape of the surface undulation has also been seen to be non-sinusoidal under certain conditions. Higher order harmonics in the spatial components of the electric field become more significant closer to the surface of the electrodes. These harmonics have been preliminarily examined in the surface shape of a thin layer of hexadecane and their exponential decay with increasing thickness of oil has been shown the ratio of these components to each other has also been shown to be independent of the voltage in the same hexadecane layer. It is uncertain why the spatial harmonics of the electric field are more prominent in hexadecane which has a lower dielectric constant than 1-decanol. It may be that the development of the higher order spatial harmonics in the surface profile of the oil layer are time dependent and the lower dielectric constant of the hexadecane allows the higher order harmonics to develop in the surface profile. The higher dielectric constant of the 1-decanol, however, causes the oil to react to the electric field much faster and as such does not allow sufficient time for the higher order harmonics to in the surface of the layer. In order to verify a time dependence on the development of the higher harmonics it may be possible to use a high speed camera to film the surface profile as the electric field is switched on. This would allow the time development of the surface profile to be seen.

The device has also been demonstrated as an amplitude programmable diffraction phase grating. Using a device with an 80μm pitch it was possible do diffract the light of the incoming beam of a 543nm green laser from the zero order into the higher order diffraction spots, whilst at the same time using a 632.8nm He-Ne laser in an interferometer to measure the amplitude of the ripple. By varying the voltage applied to the electrodes it was possible to vary the intensities of the various order spots and although the characteristics of this intensity variation did not fit with theoretical prediction for a thin sinusoidal phase grating[85], it did

show the viability of the device as a phase grating.

By operating the device in reflection it was possible to reduce the amplitude of the ripple required for the same intensity variation in the diffraction orders and this was achieved by replacing the transparent dielectric layer with a dielectric stack which was transmissive to the He-Ne laser of the interferometer and reflective to the green laser used for the diffraction tests.

For a device operated in transmission, with a pitch of 10μm, the characteristics of the change in intensity of the various diffracted orders was shown to follow the theoretical predictions using the Frounhofer approximation for a thin sinusoidal phase grating [85] and the intensities of the diffraction orders was also shown to exhibit a dependence on the amplitude of the undulation which matched closely with a Bessel function of the 1st order. 32.8% of the incident light was diffracted into the first order which is very close to the theoretical value of 33.8% [85].

A preliminary investigation of the switching characteristics of the device was performed by applying a 20kHz square wave which was switched discontinuously between a high voltage and a low voltage by modulating with a second 200Hz signal. The high and low voltages where chosen such that they switched the first diffracted order from its minimum to its maximum intensity. The switch and relax times for three different thickness of oil were shown to be 35μs, 40μs, and 49μs for switching and 79μs, 89μs, and 108μs for relaxation at oil thickness's of 20μm, 18μm, and 14μm respectively. This combination of properties in a single device is significant compared with existing technologies based on, for example, birefringent liquid crystals[15, 116], electro-optic or acousto-optic modulators[8, 117], or deformable polymer layers [118].

7.2.1 Future Work: Dieletrophoretic Phase Grating

The device in its current incarnation is a single fluid device and is thus restricted in its orientation due to gravity. It is possible that this type of undulation could

be produced at the interface between two density matched liquids. For example oil and water in an encapsulated device[119]. This approach has previously been used in variable focus lenses which produce devices which can be used in any orientation and are also resistant to mechanical shock and vibrations[5, 120]. The disadvantages of this approach is that there is a smaller difference between the refractive indices of the two chosen liquids which would probably be smaller then the difference between oil and air. Therefore the amplitude of the undulation would need to be several times bigger than that currently required in order to produce the same diffraction efficiency. Also, adding a second liquid to the system would change the inter facial tension of the two liquids. Since the model shows an inverse proportionality, any increase in inter facial tension would reduce the ripple amplitude and thus raise the operating voltage. Also the model does not take into account changes in the electric field introduced by the oil-air interface, as such only the dielectric constant of the oil is taken into account. A second liquid in the system would introduce a change in the electric field with a second dielectric constant and it is unsure how this would affect the amplitude of the ripple.

The physical properties of the oil could be selected to optimise the performance of the device. A list of the various properties of oil is given in table 7.1. It has been shown that in order to maximise the amplitude of the wrinkle an oil with a higher dielectric constant and a low surface tension must be used. If an oil with higher refractive index is used then this would in turn reduce the amplitude required for maximum diffraction efficiency. In order for the device to switch quickly in response to step changes in the voltage the oil used must also have a low viscosity. There are obviously compromises in selecting the right type of oil with the right physical properties i.e. it is colourless, does not evaporate too quickly and is also relatively non-toxic. If refractive index matching [121] oils are polar and have dielectric constants larger than the square of the refractive index then they make promising candidates although some have colouration which may

limit the operating wavelength.

It is also unclear how the scaling of the device will affect the dynamic switching time. It may be possible to reduce the switching time in higher electric fields as the electrodes become smaller.

The surface could be configured as a liquid mirror [122, 123] by doping with silver nano particles[124, 125] or the addition of self assembled Janus tiles[126]. This would not only eliminate the unwanted diffraction from the electrodes but would also lower the operating voltage by effectively halving the ripple amplitude required for a specific optical path difference. This would also negate the need for high refractive index difference in a the fluids in a two fluid device.

The demonstration of more complex non-sinusoidal surface undulation profiles suggests the possibility of producing aperiodic or arbitrary surface profiles using independently addressable electrodes.

.

Oil	Dielectric Constant	Viscosity (Nsm^{-2})	Surface Tension (mNm^{-1})	Refractive Index	Density (gcm^{-3})
Hexadecane[109]	2.05	0.00303	27.47	1.4345	0.773
1-Decanol[109]	8.10	0.1130	28.4	1.438	0.830
Glycerol[109]	47.20	0.945	63.4	1.473	1.26
Nitrobenzene[109]	34.8	0.00178	43.9	1.55	1.2
PDMS 47V20	2.68[127]	0.019[128]	20.6[128]	1.400[127]	0.950[128]
PDMS 47v350	2.80[127]	0.340[128]	21.1[128]	1.403[127]	0.970[128]
Imersion Oil[129]	N/A	0.10-0.12	N/A	1.515	1.025
RI matching Fluid[121]	N/A	0.015	29	1.460-1.570	0.832
RI matching Fluid[121]	N/A	0.085	37	1.570-1.640	1.006

Table 7.1: Physical Properties of a selection of candidate Oils

References

[1] H Morgan, AG Izquierdo, D Bakewell, NG Green, and A Ramos. The dielectrophoretic and travelling wave forces generated by interdigitated electrode arrays: analytical solution using Fourier series. *Journal Of Physics D-Applied Physics*, 34(10):1553–1561, MAY 21 2001.

[2] XJ Wang, XB Wang, FF Becker, and PRC Gascoyne. A theoretical method of electrical field analysis for dielectrophoretic electrode arrays using Green's theorem. *Journal Of Physics D-Applied Physics*, 29(6):1649–1660, JUN 14 1996.

[3] RA Hayes and BJ Feenstra. Video-speed electronic paper based on electrowetting. *Nature*, 425(6956):383–385, SEP 25 2003.

[4] J Heikenfeld and AJ Steckl. High-transmission electrowetting light valves. *Applied Physics Letters*, 86(15), APR 11 2005.

[5] B Berge and J Peseux. Variable focal lens controlled by an external voltage: An application of electrowetting. *European Physical Journal E*, 3(2):159–163, OCT 2000.

[6] S Kuiper and BHW Hendriks. Variable-focus liquid lens for miniature cameras. *Applied Physics Letters*, 85(7):1128–1130, AUG 16 2004.

[7] Neil R. Smith, Don C. Abeysinghe, Joseph W. Haus, and Jason Heikenfeld. Agile wide-angle beam steering with electrowetting microprisms. *Optics Express*, 14(14):6557–6563, JUL 10 2006.

[8] L Eldada. Optical communication components. *Review Of Scientific Instruments*, 75(3):575–593, MAR 2004.

[9] M Schadt and W Helfrich. Voltage-dependent optical activity of a twisted nematic liquid crystal. *Applied Physics Letters*, 18(4):127–&, 1971.

[10] TJ Scheffer and J Nehring. A new, highly multiplexable liquid-crystal display. *Applied Physics Letters*, 45(10):1021–1023, 1984.

[11] Mark C. Gardner, Sally E. Day, and F. Anibal Fernandez. High efficiency transflective nematic LC cell using three director states. *Journal Of Display Technology*, 4(3):282–289, SEP 2008.

[12] CM Waters, EP Raynes, and V Brimmell. Design of highly multiplexed liquid-crystal dye displays. *Molecular Crystals And Liquid Crystals*, 123(1-4):303–319, 1985.

[13] P D DeGennes. *The Physics of Liquid Crystals*. Clarandon Press, 1995.

[14] WA Crossland, TV Clapp, TD Wilkinson, IG Manolis, AG Georgiou, and B Robertson. Liquid crystals in Telecommunications Systems. *Molecular Crystals And Liquid Crystals*, 413:2499–2519, 2004. 19th International Liquid Crystal Conference, Edinburgh, Scotland, Jun 30-Jul 05, 2002.

[15] JLD De La Tocnaye. Engineering liquid crystals for optimal uses in optical communication systems. *Liquid Crystals*, 31(2):241–269, FEB 2004.

[16] L Eldada. Advances in telecom and datacom optical components. *Optical Engineering*, 40(7):1165–1178, JUL 2001.

[17] WA Crossland, IG Manolis, MM Redmond, KL Tan, TD Wilkinson, MJ Holmes, TR Parker, HH Chu, J Croucher, VA Handerek, ST Warr, B Robertson, IG Bonas, R Franklin, C Stace, HJ White, RA Woolley, and G Henshall. Holographic optical switching: The "ROSES" demonstrator. *Journal Of Lightwave Technology*, 18(12):1845–1854, DEC 2000.

[18] SE Broomfield, MAA Neil, EGS Paige, and GG Yang. Programmable binary phase-only optical-device based on ferroelectric liquid-crystal slm. *Electronics Letters*, 28(1):26–28, JAN 2 1992.

[19] Xing-jun Wang, Zhang-di Huang, Jing Feng, Xiang-fei Chen, Xiao Liang, and Yan-qing Lu. Liquid crystal modulator with ultra-wide dynamic range and adjustable driving voltage. *Optics Express*, 16(17):13168–13174, AUG 18 2008.

[20] CC Mao, M Xu, W Feng, TZ Huang, KY Wu, and JY Liu. Liquid-crystal applications in optical telecommunication. In Chien, LC, editor, *Liquid Crystal Materials, Devices, And Applications Ix*, volume 5003 of *Proceedings Of The Society Of Photo-)ptical Instrumentation Engineers (SPIE)*, pages 121–129, 1000 20th St, Po Box 10, Bellingham, WA 98227-0010 USA, 2003. Soc Imaging Sci & Technol; SPIE, Spie-int Soc Optical Engineering. Conference on Liquid Crystal Materials, Devices, and Applications IX, Santa Clara, CA, JAN 21-22, 2002.

[21] G Walker, N. Polarization control for coherent communications. *Journal of Lightwave Technology*, 8:438–458, 1990.

[22] I. Abdulhalim, R. Moses, and R. Sharon. Biomedical optical applications of liquid crystal devices. *Acta Physica Polonica A*, 112(5):715–722, NOV 2007. International School and Conference on Optics and Optical Materials, Belgrade, SERBIA, SEP 03-07, 2007.

[23] GP Crawford, DW Allender, and JW Doane. Surface elastic and molecular-anchoring properties of nematic liquid-crystals confined to cylindrical cavities. *Physical Review A*, 45(12):8693–8708, JUN 15 1992.

References

[24] DC Zografopoulos, EE Kriezis, and TD Tsiboukis. Photonic crystal-liquid crystal fibers for single-polarization or high- birefringence guidance. *Optics Express*, 14(2):914–925, JAN 23 2006. OSA Topical Meeting on Signal Recovery and Synthesis, Charlotte, NC, JUN, 2005.

[25] GP Crawford, LM Steele, R Ondriscrawford, GS Iannacchione, CJ Yeager, JW Doane, and D Finotello. Characterization of the cylindrical cavities of anopore and nucleopore membranes. *Journal Of Chemical Physics*, 96(10):7788–7796, MAY 15 1992.

[26] P Drzaic. A new director alignment for droplets of nematic liquid-crystal with low bend-to-splay ratio. *Molecular Crystals And Liquid Crystals*, 154:289–306, 1988.

[27] DA Higgins, JE Hall, and AF Xie. Optical microscopy studies of dynamics within individual polymer-dispersed liquid crystal droplets. *Accounts Of Chemical Research*, 38(2):137–145, FEB 2005.

[28] R. R. Deshmukh and M. K. Malik. Effect of temperature on the optical and electro-optical properties of poly(methyl methacrylate)/E7 polymer-dispersed liquid crystal composites. *Journal Of Applied Polymer Science*, 109(1):627–637, JUL 5 2008.

[29] N. Houriez, S. Delenclos, S. Longuemart, D. Dadarlat, and A. Hadj Sahraoui. Thermal analysis of Polymer Dispersed Liquid Crystal under electric field using photopyroelectric technique. *Laser Physics*, 19(6):1345–1349, JUN 2009.

[30] Bin Yan, Jie He, Xin Du, Ailin Qin, Qin Zhang, and Yinghan Wang. Effect of Molecular Weight of Macro-Iniferter on Electro-Optical Properties of Polymer Dispersed Liquid Crystal Films Prepared by Iniferter Polymerization. *Journal Of Polymer Science Part B-Polymer Physics*, 47(15):1530–1534, AUG 1 2009.

[31] PJ Collings. *Liquid Crystals: Nature's delicate Phase of Matter*. IOP Publishing, 1990.

[32] PJ Collings. *Introduction to Liquid Crystals*. Taylor and Francis, 1997.

[33] Edited by Birendra Bahadur. *Liquid Crystals Applications and Uses*. World Scientific, 1992.

[34] FJ Kahn, GN Taylor, and Schonhor.H. Surface-produced alignment of liquid-crystals. *Proceedings Of The IEEE*, 61(7):823–828, 1973.

[35] N Thurston, R, J Cheng, and GD Boyd. Mechanically Bistable Liquid-crystal Display Structures. *IEEE Transactions On Electron Devices*, 27(11):2069–2080, 1980.

[36] S Kitson and A Geisow. Controllable alignment of nematic liquid crystals around microscopic posts: Stabilization of multiple states. *Applied Physics Letters*, 80(19):3635–3637, MAY 13 2002.

References

[37] R Barberi, JJ Bonvent, M Giocondo, M Iovane, and AL Alexe-Ionescu. Bistable nematic azimuthal alignment induced by anchoring competition. *Journal Of Applied Physics*, 84(3):1321–1324, AUG 1 1998.

[38] CV Brown, MJ Towler, VC Hui, and GP Bryan-Brown. Numerical Analysis of Nematic Liquid Crystal Alignment on Asymmetric Surface Grating Structures. *Liquid Crystals*, 27(2):233–242, FEB 2000.

[39] GP Crawford, DW Allender, JW Doane, M Vilfan, and I Vilfan. Finite molecular anchoring in the escaped-radial nematic configuration - a h-2-nmr study. *Physical Review A*, 44(4):2570–2577, AUG 15 1991.

[40] S. Ladak, A. Davidson, C. V. Brown, and N. J. Mottram. Sidewall control of static azimuthal bistable nematic alignment states. *Journal Of Physics D-Applied Physics*, 42(8), APR 21 2009.

[41] JH Kim, M Yoneya, J Yamamoto, and H Yokoyama. Surface alignment bistability of nematic liquid crystals by orientationally frustrated surface patterns. *Applied Physics Letters*, 78(20):3055–3057, MAY 14 2001.

[42] Phil Kook Son, Jeung Hun Park, Jae Chang Kim, Tae-Hoon Yoon, Soon Joon Rho, Sung Tae Shin, Jang Sub Kim, Soon Kwon Lim, and Jun Hyung Souk. Control of Liquid Crystal Alignment on SiOx Film Surfaces by Low-Energy Ion Beam. *Japanese Journal Of Applied Physics*, 48(5, Part 1), MAY 2009.

[43] WJ Duffin. *Electricity and Magnetism*. McGraw-Hill, 1990.

[44] P Lorrain and DR Corson. *Electromagnetic Fields and Waves*. W H Freeman and Company, 1988.

[45] E Hecht. *Optics*. Addison Wesley, 1987.

[46] Yeh Pochi. *Optical Waves in Layered media*. Wiley, 2005.

[47] ZZ Zhuang, SW Suh, and JS Patel. Polarization controller using nematic liquid crystals. *Optics Letters*, 24(10):694–696, MAY 15 1999.

[48] T Chiba, Y Ohtera, and S Kawakami. Polarization stabilizer using liquid crystal rotatable waveplates. *Journal Of Lightwave Technology*, 17(5):885–890, MAY 1999.

[49] L Dupont, JD de la Tocnaye, M Le Gall, and D Penninckx. Principle of a compact polarisation mode dispersion controller using homeotropic electroclinic liquid crystal confined single mode fibre devices. *Optics Communications*, 176(1-3):113–119, MAR 15 2000.

[50] Y Ohtera, T Chiba, and S Kawakami. Liquid crystal rotatable waveplates. *IEEE Photonics Technology Letters*, 8(3):390–392, MAR 1996.

References

[51] BR Acharya, KW Baldwin, RA MacHarrie, JA Rogers, CC Huang, and R Pindak. In-fiber nematic liquid crystal optical modulator based on in-plane switching with microsecond response time. *Applied Physics Letters*, 81(27):5243–5245, DEC 30 2002.

[52] E Hecht. *Optics*. Addison Wesley, fourth edition, 2002.

[53] M born and E Wolf. *Principles of Optics*. Cambridge University Press, 2005.

[54] http://atom.physics.calpoly.edu, 2009.

[55] FC Frank. On the theory of liquid crystals. *Discussion of the Faraday Society*, 1958.

[56] HA Pohl. The motion and precipitation of suspensoids in divergent electric fields. *Journal of Applied Physics*, 22:869–871, 1951.

[57] HA Pohl. Some effects of nonuniform fields on dielectrics. *Journal of Applied Physics*, 29:1182–1188, 1958.

[58] TB Jones. Liquid dielectrophoresis on the microscale. *Journal Of Electrostatics*, 51-52:290–299, 2001.

[59] H Pellat. *Journali Comptes Rendus Hebdomadaires des Sceaces de l'Academie des sciences*, 119:675, 1894.

[60] TB Jones, MP Perry, and JR Melcher. Dielectric siphons. *Science*, 174(4015):1232–&, 1971.

[61] TB Jones, M Gunji, M Washizu, and MJ Feldman. Dielectrophoretic liquid actuation and nanodroplet formation. *Journal Of Applied Physics*, 89(2):1441–1448, JAN 15 2001.

[62] d Ahmed, D Hsu, C Bailey, and TB Jones. Dispensing picoliter droplets using dielctrophoretic micro-actuation. *First International Conference on Microchannels and Minichannels*, 2003.

[63] R Ahmed, N Tombs, TB Jones, and P Leas. Dispensing thin liquid films using dielectrophoresis. In *Fifth Int'l Conference on Electrowetting*, 2006.

[64] HA Pohl. *Dielectrophoresis*. Cambridge Monographs on Physics, 1978.

[65] Ff Becker, Xb Wang, Y Huang, R Pethig, J Vykoukal, and Prc Gascoyne. Separation of human breast-cancer cells from blood by differential dielectric affinity. *Proceedings Of The National Academy Of Sciences Of The United States Of America*, 92(3):860–864, JAN 31 1995.

[66] GH Markx, PA Dyda, and R Pethig. Dielectrophoretic separation of bacteria using a conductivity gradient. *Journal Of Biotechnology*, 51(2):175–180, NOV 1 1996.

References

[67] NG Green and H Morgan. Dielectrophoretic investigations of sub-micrometre latex spheres. *Journal Of Physics D-Applied Physics*, 30(18):2626–2633, SEP 21 1997.

[68] NG Green, H Morgan, and JJ Milner. Manipulation and trapping of sub-micron bioparticles using dielectrophoresis. *Journal Of Biochemical And Biophysical Methods*, 35(2):89–102, SEP 25 1997.

[69] T Muller, A Gerardino, T Schnelle, SG Shirley, F Bordoni, G DeGasperis, R Leoni, and G Fuhr. Trapping of micrometre and sub-micrometre particles by high-frequency electric fields and hydrodynamic forces. *Journal Of Physics D-Applied Physics*, 29(2):340–349, FEB 14 1996.

[70] RC Wrede and M Spiegel. *Advanced Calculus*. McGraw-Hill, second edition, 2002.

[71] GT Barnes and IR Gentle. *Interfacial Science: An Introduction*. Oxford University Press, 2005.

[72] AW Adamson and AP Gast. *Physical Chemistry of Surfaces*. Wiley-Interscience, sixth edition, 1997.

[73] E Hallstig, J Stigwall, T Martin, L Sjoqvist, and M Lindgren. Fringing fields in a liquid crystal spatial light modulator for beam steering. *Journal Of Modern Optics*, 51(8):1233–1247, MAY 20 2004.

[74] MSL Lee, P Pichon, C Sauvan, JC Rodier, P Lalanne, M Hutley, D Joyeux, P Chavel, E Cambril, and Y Chen. Transmission blazed-binary gratings for visible light operation: performances and interferometric characterization. *Journal Of Optics A-Pure And Applied Optics*, 5(5):S244–S249, SEP 2003. 19th Congress of the International-Commission-for-Optics, FLORENCE, ITALY, AUG 25-30, 2002.

[75] J Chen, PJ Bos, H Vithana, and Dl Johnson. An electrooptically controlled liquid-crystal diffraction grating. *Applied Physics Letters*, 67(18):2588–2590, OCT 30 1995.

[76] WM Gibbons and ST Sun. Optically generated liquid-crystal gratings. *Applied Physics Letters*, 65(20):2542–2544, NOV 14 1994.

[77] S Matsumoto, M Goto, SW Choi, Y Takanishi, K Ishikawa, H Takezoe, G Kawamura, I Nishiyama, and H Takada. Phase grating using a ferroelectric liquid-crystal mixture with a photocurable liquid crystal. *Journal Of Applied Physics*, 99(11), JUN 1 2006.

[78] B Apter, U Efron, and E Bahat-Treidel. On the fringing-field effect in liquid-crystal beam-steering devices. *Applied Optics*, 43(1):11–19, JAN 1 2004.

[79] DP Resler, DS Hobbs, RC Sharp, LJ Friedman, and TA Dorschner. High-efficiency liquid-crystal optical phased-array beam steering. *Optics Letters*, 21(9):689–691, MAY 1 1996.

References

[80] Raphael A. Guerrero, Jerry T. Barretto, Jerwin L. V. Uy, Ivan B. Culaba, and Benjamin O. Chan. Effects of spontaneous surface buckling on the diffraction performance of an Au-coated elastomeric grating. *Optics Communications*, 270(1):1–7, FEB 1 2007.

[81] C Harrison, CM Stafford, WH Zhang, and A Karim. Sinusoidal phase grating created by a tunably buckled surface. *Applied Physics Letters*, 85(18):4016–4018, NOV 1 2004.

[82] TK Barik, PR Chaudhuri, A Roy, and S Kar. Probing liquid surface waves, liquid properties and liquid films with light diffraction. *Measurement Science & Technology*, 17(6):1553–1562, JUN 2006.

[83] TK Barik, A Roy, and S Kar. A simple experiment on diffraction of light by interfering liquid surface waves. *American Journal Of Physics*, 73(8):725–729, AUG 2005.

[84] D Byrne and JC Earnshaw. Pphoton-correlation spectroscopy of liquid interfaces .1. liquid-air interfaces. *Journal of Physics D-Applied Physics*, 12(7):1133–1144, 1979.

[85] Joseph W Goodman. *Introduction to Fourier Optics*. Roberts, 2005.

[86] Frank Bowman. *Intorduction to Bessel Functions*. Dover Publications, 1958.

[87] R Pethig. Dielectrophoresis: Using inhomogeneous AC electrical fields to separate and manipulate cells. *Critical Reviews In Biotechnology*, 16(4):331–348, 1996.

[88] Microposit S1800 Series Photo Resists. Shipley Europe Ltd, Herald Way, Coventry, CV3 2RQ, United Kingdom.

[89] C. Tsakonas, A. J. Davidson, C. V. Brown, and N. J. Mottram. Multistable alignment states in nematic liquid crystal filled wells. *Applied Physics Letters*, 90(11), MAR 12 2007.

[90] S Chandrsekhar. *Liquid Crystals*. Cambridge University Press, 2nd edition, 1992.

[91] Sonin A A. *The Surface Physics Of liquid Crystals*. Gordan and Breach, 1995.

[92] FM Leslie. Continuum theory for nematic liquid-crystals. *Continuum Mechanics And Thermodynamics*, 4(3):167–175, AUG 1992.

[93] J. M. Hind, A. A. T Smith, and C. V. Brown. Transient capacitance study of switching in the nematic Freedericksz geometry. *Journal Of Applied Physics*, 100(9), NOV 1 2006.

[94] GP Bryan-Brown, EL Wood, and IC Sage. Weak surface anchoring of liquid crystals. *Nature*, 399(6734):338–340, MAY 27 1999.

[95] AH Alexopoloulos and EI Franses. Surface tension of viscous and anisotropic fluids. *Colloids and Surfaces*, 43:263–277, 1990.

[96] MGJ Gannon and T E Faber. The surface tension of nematic liquid crystals. *Philosophical Magazine A*, 37:117–135, 1978.

[97] MM Telo Da Gama. The interfacial properties of a model of nematic liquid crystal. *Molecular Physics*, 52:585–610, 1984.

[98] S Herminghaus, K Jacobs, K Mecke, J Bischof, A Fery, M Ibn-Elhaj, and S Schlagowski. Spinodal dewetting in liquid crystal and liquid metal films. *Science*, 282(5390):916–919, OCT 30 1998.

[99] ZQ Lin, T Kerle, SM Baker, DA Hoagland, E Schaffer, U Steiner, and TP Russell. Electric field induced instabilities at liquid/liquid interfaces. *Journal Of Chemical Physics*, 114(5):2377–2381, FEB 1 2001.

[100] Farshid Mostowfi, Khristo Khristov, Jan Czarnecki, Jacob Masliyah, and Subir Bhattacharjee. Electric field mediated breakdown of thin liquid films separating microscopic emulsion droplets. *Applied Physics Letters*, 90(18), APR 30 2007.

[101] E Schaffer, T Thurn-Albrecht, TP Russell, and U Steiner. Electrohydrodynamic instabilities in polymer films. *Europhysics Letters*, 53(4):518–524, FEB 2001.

[102] F Vandenbrouck, MP Valignat, and AM Cazabat. Thin nematic films: Metestability and spinoidal dewetting. *Physical Review Letters*, 82:2693–2696, 1999.

[103] A Vrij. Possible mechanism for spontaneous rapture of thin films. *Discussions of the Faraday Lectures*, pages 23–33, 1966.

[104] Richard James, Eero Willman, F. Anibal Fernandez, and Sally E. Day. Finite-element modeling of liquid-crystal hydrodynamics with a variable degree of order. *IEEE Transactions On Electron Devices*, 53(7):1575–1582, July 2006.

[105] S Herminghaus. Dynamical instability of thin liquid films between conducting media. *Physical Review Letters*, 83(12):2359–2361, SEP 20 1999.

[106] E Schaffer, T Thurn-Albrecht, TP Russell, and U Steiner. Electrically induced structure formation and pattern transfer. *Nature*, 403(6772):874–877, FEB 24 2000.

[107] Adrian Staicu and Frieder Mugele. Electrowetting-induced oil film entrapment and instability. *Physical Review Letters*, 97(16), OCT 20 2006.

[108] Tao Sun, Hywel Morgan, and Nicolas G. Green. Analytical solutions of ac electrokinetics in interdigitated electrode arrays: Electric field, dielectrophoretic and traveling-wave dielectrophoretic forces. *Physical Review E*, 76(4, Part 2), OCT 2007.

References

[109] Online 2009 Knovel Critcial Tables, 2nd ed.

[110] Yorkshire Photonic Technology Ltd, Unit HM13 Holmfield Mills, Holdsworth Road, Holmfield, Halifax,HX3 6SN.

[111] NG Green, A Ramos, and H Morgan. Numerical solution of the dielectrophoretic and travelling wave forces for interdigitated electrode arrays using the finite element method. *Journal Of Electrostatics*, 56(2):235–254, SEP 26 2002.

[112] S Masuda, M Washizu, and M Iwadare. Separation of small particles suspended in liquid by nonuniform traveling field. *IEEE Transactions On Industry Applications*, 23(3):474–480, MAY-JUN 1987.

[113] SU8-10 chemically amplified epoxy based negative resist. MicroChem Corp, 90 Oak St, Newton, MA 02464,USA.

[114] BR Acharya, L Moller, KW Baldwin, RA MacHarrie, RA Stepnoski, CC Huang, R Pindak, and JA Rogers. In-line liquid-crystal microcell wave plates and their application for high-speed, reset-free polarization mode dispersion compensation in 40-Gbit/s systems. *Applied Optics*, 42(27):5407–5412, SEP 20 2003.

[115] HR Kim, YW Lee, SJ Kim, DW Kim, CJ Yu, B Lee, and SD Lee. A rotatable waveplate using a vertically aligned deformed-helix ferroelectric liquid crystal. *Ferroelectrics*, 312:479–484, 2004. 9th International Conference On Ferroelectric Liquid Crystals, Dublin, IRELAND, AUG 24-29, 2003.

[116] Ravi K. Komanduri, Chulwoo Oh, and Michael J. Escuti. Reflective liquid crystal polarization gratings with high efficiency and small pitch - art. no. 70500J. In Khoo, IC, editor, *Liquid Crystal XII*, volume 7050 of *Proceedings Of The Society Of Photo-optical Instrumentation Engineers (SPIE)*, page J500, 1000 20th St, Po Box 10, Bellingham, WA 98227-0010 USA, 2008. SPIE, SPIE-Int Soc Optical Engineering. Conference on Liquid Crystals XII, San Diego, CA, AUG 11-12, 2008.

[117] S. Mias and H. Camon. A review of active optical devices: I. Amplitude modulation. *Journal Of Micromechanics And Microengineering*, 18(8), AUG 2008.

[118] N Bowden, S Brittain, AG Evans, JW Hutchinson, and GM Whitesides. Spontaneous formation of ordered structures in thin films of metals supported on an elastomeric polymer. *Nature*, 393(6681):146–149, MAY 14 1998.

[119] CV Brown, MI Newton, and G McHale. Switchable diffraction grating, 2006.

[120] http://www.varioptic.com.

[121] RI Matching Liquids Series A (http://www.cargille.com/refractivestandards.shml) Cargille Labs.

[122] H Yockell-Lelievre, EF Borra, AM Ritcey, and LV da Silva. Optical tests of nanoengineered liquid mirrors. *Applied Optics*, 42(10):1882–1887, APR 1 2003.

[123] D Yogev and S Efrima. Novel silver metal liquidlike films. *Journal Of Physical Chemistry*, 92(20):5754–5760, OCT 6 1988.

[124] EF Borra, AM Ritcey, R Bergamasco, P Laird, J Gingras, M Dallaire, L Da Silva, and H Yockell-Lelievre. Nanoengineered astronomical optics. *Astronomy & Astrophysics*, 419(2):777–782, MAY 2004.

[125] J Gingras, JP Dery, H Yockell-Lelievre, E Borra, and AM Ritcey. Surface films of silver nanoparticles for new liquid mirrors. *Colloids And Surfaces A-physicochemical And Engineering Aspects*, 279(1-3):79–86, MAY 15 2006.

[126] Michael A. Bucaro, Paul R. Kolodner, J. Ashley Taylor, Alex Sidorenko, Joanna Aizenberg, and Tom N. Krupenkin. Tunable Liquid Optics: Electrowetting-Controlled Liquid Mirrors Based on Self-Assembled Janus Tiles. *Langmuir*, 25(6):3876–3879, MAR 17 2009.

[127] Rhodersil Oils 47(http://www.bluestarsilicones.com) Bluestar Silcones France SAS.

[128] X Fanton, AM Cazerbat, and D Quere. *Langmuir*, 12:5875–5880, 1996.

[129] Merck Cat. No. 1.04699 "Imersion Oils For Microscopy".